UC Santa Cruz
UC Santa Cruz Electronic Theses and Dissertations

Title

Multi-wavelength Astrophysical Probes of Dark Matter Properties

Permalink

https://escholarship.org/uc/item/7fh692sv

Author

McDaniel, Alex Raymond

Publication Date

2020

Copyright Information

Peer reviewed|Thesis/dissertation

UNIVERSITY OF CALIFORNIA

SANTA CRUZ

**MULTI-WAVELENGTH ASTROPHYSICAL PROBES OF DARK
MATTER PROPERTIES**

A dissertation submitted in partial satisfaction of the
requirements for the degree of

DOCTOR OF PHILOSOPHY

in

PHYSICS

by

Alex McDaniel

June 2020

The Dissertation of Alex McDaniel
is approved:

_____

Professor Tesla Jeltema, Chair

_____

Professor Stefano Profumo

_____

Professor Robert Johnson

_____
Quentin Williams
Acting Vice Provost and Dean of Graduate Studies

Table of Contents

List of Figures

List of Tables

Abstract

Multi-wavelength Astrophysical Probes of Dark Matter Properties

by

Alex McDaniel

Although we have yet to fully understand the nature of dark matter (DM), astrophysical observations across the electromagnetic spectrum allow us to probe its properties and constrain proposed models. These include annihilating DM models that can be investigated through their standard model annihilation products such as electrons and positrons that produce radio, X-ray, and gamma-ray emission through typical radiative processes such as synchrotron radiation and inverse compton scattering. Some other proposed DM models exhibit collisional self interactions that impact the shapes of DM haloes. Using X-ray observations, the DM halo shapes can be constrained in order to probe the strength of possible DM self interactions. In this dissertation, I present an overview of our work in the development of the RX-DMFIT tool to study the secondary emission from DM annihilation, along with applications to DM and cosmic ray studies in the Andromeda galaxy. I also discuss work using data from Chandra and XMM-Newton in studying the X-ray shapes of elliptical galaxies to constrain DM self interactions.

To my family, especially my Mom and my Grandma Pat

Acknowledgments

I would first like to start by thanking my advisor Tesla Jeltema, without whom this work would not have been possible. She has been a great resource of knowledge in astronomy and astrophysics, as well as generally how to navigate grad school and academia. I cannot thank her enough for the opportunities she has provided during my time in my graduate career, allowing me to perform exciting research and travel to conferences and summer schools. Her passion and dedication to supporting her students cannot be overstated, and her mentorship has been the driving force in helping me grow into a researcher and scientist. Thanks to Stefano Profumo, who has been an amazing collaborator and invaluable in accomplishing this work, while helping show me how to approach questions in physics in novel and creative ways. I would also like to thank Robert Johnson for serving on my dissertation committee, and the many graduate students here at UC Santa Cruz who have given me support and camaraderie over the years.

My family of course has also been a major source of support throughout my life before and throughout grad school. I would like foremost to thank my mom Laurie for her unwavering support in everything that I have done. I would also like to especially thank my Aunt Lynda and Uncle Alan for all their help and support over the past five years. From helping me get settled in Santa Cruz in the first place, to being available for dinners and a place to stay over the hill, it has been great to have you nearby and made grad school more enjoyable. Finally, I would like to thank my girlfriend Jordan. Thank you for putting up with all the stress, the erratic schedules, and long work nights. You have made our time in Santa Cruz truly memorable, and without your support completing grad school would not be possible.

The text of this dissertation includes reprints of the following previously pub-

lished material: Chapter 2 is adapted from "Multiwavelength analysis of dark matter annihilation and RX-DMFIT." by A. McDaniel, T. Jeltema, S. Profumo, and E. Storm in J. Cosmology Astropart. Phys., 9:027, September 2017. Chapter 3 is adapted from "Multiwavelength analysis of annihilating dark matter as the origin of the gamma-ray emission from M31." by A. McDaniel, T. Jeltema, S. Profumo, Phys. Rev. D, 97(10):103021, May 2018. Chapter 4 is adapted from "Exploring a cosmic-ray origin of the multiwavelength emission in M31." by A. McDaniel, T. Jeltema, S. Profumo, Phys. Rev. D, 100(2):023014, July 2019. The co-authors listed in this publication directed and supervised the research which forms the basis for the dissertation.

Chapter 1

Introduction

1.1 Discovery and Evidence for Dark Matter

Among the most prominent open questions in physics is the fundamental nature of dark matter. Various cosmological and astrophysical clues provide insight into the composition of the energy density in the universe. Evidence from the cosmic microwave background (CMB) [173, 1], formation of large-scale structure [316, 114], supernovae observations [265, 45] and baryon-acoustic oscillations [253, 17] reveal that the universe is made up of about 70% dark energy (DE), which drives the expansion of the universe, while the unknown dark matter (DM) contributes another $\sim 26\%$ and the familiar baryonic matter makes up the final $\sim 4\%$ of the energy density. Although the presence of DM can be inferred from its gravitational effects, and the abundance of DM in the universe determined from big-bang-nucleosytnthesis (BBN) and CMB observations [247, 104], an understanding of the fundamental nature of DM remains elusive.

DM was initially introduced by Fritz Zwicky in 1933 as a result of observations of the velocity distributions of galaxies in the Coma Cluster [328]. Applying the virial theorem to the galaxies in Coma, Zwicky found that the luminous mass in

the cluster was a factor of ~ 400 too small to produce the galaxy velocity distributions, and thus posited that there may be an invisible component of "dark matter" contributing to the mass of the cluster. During the subsequent decades there were a handful of observations of nearby galaxies that suggested divergence from unity of the mass-to-light ratio [23, 249], though other astrophysical arguments were presented and overall the dark matter hypothesis gained little attention. The search for DM was accelerated in the 1970s and 1980s by the work of Rubin and Ford. Measuring the galactic rotation curves of Andromeda (M31) and other galaxies, they observed flat curves that suggested an additional component of mass extending far beyond the luminous component [272]. Since the pioneering work of Rubin and Ford, the case for the existence of DM has been reaffirmed and expanded through a variety of probes including galactic rotation curves, lensing measurements, BBN, the CMB, observations of merging clusters, and observations of X-ray gas in clusters (for some reviews, see [44, 37]).

Though most of the effort in addressing the evidence for DM has focused on searching for an unobserved form of matter, alternate theories can explain aspects of the observed phenomena without requiring the existence of this unaccounted-for matter. This group of theories falls under the umbrella of MOdified Newtonian Dynamics (MOND) [229, 228, 32, 33] and calls for modifications to our understanding of gravity that can explain some of the observational evidence of DM. In particular, MOND theories are quite successful in describing DM effects at galactic scales such as the rotation curves of galaxies and the Tully-Fisher relation. However, several shortcomings of MOND exist [124, 224]. The dynamics of galaxy clusters is a notable challenge for MOND theories, most glaringly in the case of the Bullet Cluster which has been touted as "Direct Evidence of Dark Matter" [103]. Additionally, the matter power spectrum from MOND theories is

in stark disagreement with observations [124]. Among other challenges (see e.g. [124, 224]) these present a strong case against MOND.

The corpus of observational evidence and the shortcomings of alternative gravity theories has fostered a wide agreement between particle physicists, astrophysicists, and cosmologists that there is a need for some form of matter to account for the various observations. This has led to the standard cosmological model – ΛCDM – containing a cosmological constant (Λ) for dark energy along with Cold Dark Matter (CDM).

1.2   Dark Matter Properties and Candidates

The ΛCDM framework assumes that there is a currently undiscovered matter component of the universe (the "Cold Dark Matter"). This most commonly takes the form of a new particle outside the Standard Model paradigm, though there are also intriguing arguments for the possibility that dark matter consists of primordial black holes (PBH) that were formed early in the universe [171]. In either case, any proposed dark matter must meet a handful of conditions.

As implied by the name, the dark matter must be "dark". That is to say that any electromagnetic interactions are suppressed below current detection thresholds. The dark matter also must be stable on timescales of the Hubble time in order to both have played a significant role in large-scale-structure formation while surviving to the current time in the observed abundances. Additionally, the dark matter must be "cold". In other words, the dark matter must be relatively massive in comparison to its rest mass and non-relativistic during the early universe in order to account for the observed structure of the universe on large scales. These conditions eliminate all SM particles as candidates for DM, emphasizing the need for new physics. For instance, protons and electrons certainly have significant

charge so are not "dark". Neutrons meet the neutrality condition, but do not fulfill the stability requirement given the relatively short free neutron lifetime ~ 900 s. Neutrinos are both stable and electromagnetically neutral, but do not meet the "cold" criterion to be a good DM candidate.

Further phenomenological arguments can be applied in order to constrain the possible mass range of DM candidates. From the basic requirement that the DM particle is gravitationally bound on length scales representative of dwarf galaxies (i.e. $\sim$ kpc) a lower bound can be determined. Taking this length scale to be the upper limit of the DM de Broglie wavelength, the mass then has a lower limit of $m \gtrsim 10^{-22}$ eV [179, 202]. Note that this assumes the particle is a boson. A fermion will have a maximum allowed phase space density, and Pauli blocking becomes relevant [307], increasing the minimum DM mass by roughly 23 orders of magnitude.

At the high end of the mass spectrum, a rough upper limit on the DM can be determined by placing conditions on the discreteness of the DM on galactic scales. The granularity of DM can produce observable effects by disrupting bound systems. For masses $m > 10^6 M_\odot$, this can lead to heating of the galactic disk [198] and masses at the level of $m \gtrsim 10^3 M_\odot$ would disrupt globular clusters [164, 267, 232]. Thus we have an upper bound $m \lesssim 10^3 M_\odot \sim 10^{70}$ eV.

Given the conditions described above, there exists a wide and diverse zoo of potential DM candidates across a mass scale spanning ~ 90 orders of magnitude. A particularly well motivated class of particle DM candidates that has received some of the most scrutiny is Weakly Interacting Massive Particles (WIMPs) [291]. In the following section we discuss some of the motivations for WIMPs as DM along with approaches to detecting and constraining this class of particles.

1.3   WIMP Dark Matter and Detection Methods

WIMPs are a class of neutral, stable particles with masses roughly on the order of the electroweak scale ($\sim$ GeV - TeV), sufficiently satisfying the requirements discussed in the previous section. Additionally, WIMPs are thermal relics produced in the early universe before undergoing freeze-out as the temperature of the universe cools below the weak scale. The density of WIMPs that then remains in the universe after freeze-out is dependent on the annihilation cross-section of the particle. For the typical annihilation cross-section at the electroweak scale, the resulting fractional abundance is roughly the same as the current observed DM density. This apparent coincidence (sometimes referred to as the "WIMP Miracle") has made WIMPs one of the more intriguing classes of DM candidates, and has spurred numerous and varied experimental search techniques (cf. [21, 43, 191, 37, 36]).

The methods used in the identification of DM can be broadly placed into the three categories of direct detection, indirect detection, and collider searches. Collider searches rely on the production of DM particles from the collision of standard model particles (e.g. proton-proton collisions at the Large Hadron Collider) and are naturally model-dependent [60]. Since the detectors in collider experiments are not able to detect the DM directly, the signature in collider searches is in the form of missing energy after the collisions that would correspond to the DM escaping the detector.

Direct detection experiments focus on DM interactions with the standard model, primarily DM scattering off of Standard Model particles as the DM passes through the Earth-based detectors. There are several different implementations of this approach (see [279] for a comprehensive review), however currently the strongest constraints for WIMPs with $m \gtrsim 5$ GeV come from the XENON1T

[323] and LUX [16] liquid noble gas detectors. Thus far, no definitive DM signal has been seen in collider or direct detection experiments, though direct detection experiments have been able to place constraints on the DM-nucleon scattering cross-section, and collider searches can constrain certain model-dependent interactions.

Another promising approach to DM searches is indirect detection, wherein the annihilation or decay of WIMP DM produces Standard Model particles that can then be detected using a multitude of standard techniques. These encompass much of multi-messenger astronomy, including the detection of neutrinos, cosmic-rays, and electromagnetic radiation. While the neutrino [186, 27, 303] and cosmic-ray [101, 25, 260] approaches can also provide interesting results, we will focus on the electromagnetic signatures of annihilating DM.

Significant research efforts have been put into DM indirect searches across the electromagnetic spectrum. In particular, gamma-rays have been extensively used to seek out signals of DM with both ground based [324, 266] and space based observatories, most notably the Fermi-LAT [22]. DM annihliations can produce neutral pions, which rapidly decay into gamma-rays. The gamma-rays then travel in straight lines directly from the source to the detector, making them enticing targets for DM indirect searches. In addition to gamma-rays produced by the annihilation of DM, observations at other wavelengths are a powerful and complementary probe of DM. Annihilations of DM are predicted to yield charged relativistic electrons and positrons [106]. These charged particles then emit secondary radiation at radio, X-ray, and gamma-ray energies through a variety of radiative processes [106, 220]. In the presence of magnetic fields, the electrons will synchrotron radiate and produce synchrotron emission. The relativistic electrons and positrons can also upscatter ambient photons to higher energies through

6

inverse Compton scattering. CMB photons which are ubiquitous throughout the universe are up-scattered to X-ray energies, while infrared and starlight photons can be scattered to X-ray and soft gamma-ray energies [219, 221]. A difficulty arises with the secondary emission because effects of diffusion become important and must be accounted for in calculations of the expected flux [220].

Targets that are well suited to multiwavelength DM searches encompass a large range of astrophysical systems, including local dwarf galaxies, normal galaxies (e.g. the Milky Way, M31), and galaxy clusters. Ideal targets are those that exhibit a high concentration of DM, low astrophysical background, and – for radio searches – magnetic fields of at least around $\sim \mu$G in order to produce detectable synchrotron emission. Galaxy clusters for example meet many of these criteria (and also benefit from negligible diffusion effects [220, 106]). Clusters are the largest virialized objects in the universe with the majority of their mass ($\sim 80\%$) being composed of DM. Previously, non-detections of gamma-rays in clusters have been used to constrain DM annihilation [7]. Clusters are also known to typically contain magnetic fields at the $\gtrsim \mu$G scale making them potentially strong targets for radio searches [292, 293, 106]. Recent studies have shown that with upcoming radio equipment, clusters have the capability of providing highly competitive constraints on the DM cross-section [293].

Similarly, local group dwarf galaxies are also DM rich, near in proximity, and – in the case of dwarf spheroidal galaxies (dSphs) – contain low astrophysical backgrounds at radio, X-ray, and gamma-ray energies. Some of the most stringent indirect detection constraints on the DM annihilation cross-section come from gamma-ray observations of dwarf spheroidal galaxies [9]. At radio frequencies, several studies of dwarfs have been performed exploring current observational constraints [107, 283, 238] as well as the ability of upcoming instruments such as

the Square-Kilometer Array (SKA) radio telescope [96, 194] to further constrain annihilating DM models.

Galaxies such as the Milky Way and M31 are known to exist in large DM halos, making them natural targets for DM searches, and the presence of magnetic fields in these systems can produce observable synchrotron emission needed for multiwavelength probes. In particular, the Galactic Center (GC) of the MW is expected to be one of the brightest sources of DM annihilation due to its proximity (~ 8.3 kpc) as well as the higher concentration of DM in the inner regions of galaxies. Multiple separate gamma-ray observations of the GC using the Fermi-LAT telescope have revealed a significant detection of extended excess emission peaking at ~ 2 GeV and exhibiting an approximately spherical spatial symmetry [175, 166, 167, 2, 116, 83, 84, 177, 327, 15]. This emission, commonly referred to as the "Galactic Center Excess" (GCE) has been shown in multiple studies to be consistent with the signal expected from WIMP DM annihilating through quark-antiquark channels with a mass of $\sim 30-50$ GeV and an annihilation cross-section in line with that of a thermal relic [2, 83, 116, 167, 175]. The possibility of a DM annihilation signal in the GCE has undergone extensive scrutiny, and while the GCE can potentially be explained through other astrophysical processes, the possibility of DM annihilation is enticing.

If the GCE is in fact due to DM annihilation, there should also be similar DM induced emission signals in nearby DM halos. The Andromeda (M31) galaxy offers an excellent target for such a comparative study as the nearest large spiral galaxy at a distance of ~ 785 kpc. Early observations were able to place upper limits on the gamma-ray emission from M31, though no definitive signal had been reported [146, 256, 288, 53]. In more recent years, an observed extended emission in the central region of M31 with a radial extent ~ 5 kpc was reported from

observations with the Fermi-LAT [10]. Additionally, recent observations of diffuse gamma-ray emission in the outer halo of M31 could also have implications DM annihilation in Andromeda [196]. Due to similarities between the MW and M31, as well as between the purported observed excesses in each galaxy, previous work in studying the GCE can serve as a guide for how to approach understanding the emission in M31.

Both the GCE as well as the M31 observations provide intriguing potential signals of DM annihilation. However, a complicating factor when searching for DM induced emission in galaxies is the existence of astrophysical backgrounds at essentially all wavelengths of interest. This presents difficulties in disentangling a possible DM signal from other standard astrophysical emissions. In addition to a DM interpretation, astrophysics based explanations for the GCE have been put forward including an unresolved population of point sources in the form of millisecond pulsars (MSP) [26, 64, 133] or additional cosmic-rays sources [91, 154, 100]. Unsurprisingly, these have similarly drawn interest as possible explanations for the M31 observation [133, 151, 221]. It is likely that each of these components can partially contribute to the gamma-ray emission, though as of yet the DM interpretations have still provided some of the best fits to the gamma-ray spectrum of the GCE. However, concerted multiwavelength observations can continue to provide a better understanding of both the GCE as well as the gamma-ray emission in M31, which has not faced the same degree of scientific scrutiny as the GCE.

1.4 Self Interacting Dark Matter and Small Scale Challenges

While WIMPs are well motivated DM candidates from both cosmological and particle physics perspectives, the lack of strong experimental evidence has weakened the case for WIMP DM [21]. As collider experiments reach higher and higher energies without finding evidence of WIMPs, along with the ever more stringent constraints on the annihilation, decay, and WIMP-nucleon scattering properties provided by indirect and direct searches, scientists in the field have been increasingly interested in exploring DM candidates external to the WIMP paradigm. Further motivation for non-WIMP DM comes from challenges that arise in the ΛCDM framework.

The ΛCDM model of cosmology has done an excellent job describing the structure of the universe on large scales as well as elements of galaxy formation [55, 286, 308]. However, on smaller scales discrepancies arise between observations in the local universe and the small-scale-structure predicted by ΛCDM N-body simulations [72, 310]. A few of note include the missing satellites problem [197, 234], the core-cusp problem[148, 233, 192], and the "Too-Big-To-Fail" problem [62, 63].

The missing satellites problem describes the discrepancy between the observed number of low-mass satellite galaxies found in galactic scale DM halos and the abundance of sub-halos predicted by simulations. High resolution cosmological simulations predict on the order of thousands of observable satellites in a typical Milky Way halo [285], yet to date only roughly ~ 50 have been discovered [128].

The core-cusp problem highlights the inability of many CDM simulations to accurately predict the inner structure of DM cores. In simulations, DM halos are

characterized by steep "cuspy" densities in their inner regions. However, observed DM halos instead usually exhibit a diversity of more flat, cored inner profiles.

Finally, the "Too-Big-To-Fail" problem refers to a lack of observed local galaxies with high central densities. The most massive satellite galaxies observed have central densities lower than those predicted in simulations [285]. If the predicted high density subhalos do exist, they should be "Too-Big" not to form stars (i.e. "to-Fail" to form stars) and thus – in principle – be observable. So either by some mechanism star-formation in these specific galaxies has been suppressed, or CDM fails to accurately describe the structure of the galaxies at this scale.

While there are strong motivations suggesting that baryonic effects play a meaningful role in understanding these discrepancies [67, 243, 168, 19], another intriguing approach is to consider how modifications to the standard collisionless cold dark matter paradigm can address these issues. For instance, warm dark matter has been suggested as a possible explanation of the missing satellites, as dark matter with some greater free-streaming in the early universe could wipe out the smaller perturbations that would ultimately form the simulation based expectation of subhalo abundances [57, 66].

An additional possibility is Self-Interacting Dark Matter (SIDM) wherein DM is not fully collisionless, but rather can exhibit some degree of self-interactions. If the collisional cross-section is sufficiently large, these self-interactions can have observable macroscopic effects on the DM halo properties. N-Body simulations that incorporate DM self-interactions provide some of our best understanding of how SIDM can affect DM substructure and halos. Several studies have shown that SIDM with $\sigma/m \approx 0.5 - 10$ cm^2/g produces flat cores and lower densities in the inner regions of DM halos, which can address the core-cusp and TBTF problems [318, 254, 137]. Dark matter self-interactions also impact the shapes

of the DM halos. In CDM, halos tend to be triaxial [131], however introducing self interactions yields halos that are more spherical due to isotropized particle velocities [254, 284, 115].

Early constraints on the SIDM cross-section did not bode well for a SIDM solution to the small-scale problems. Simulations of SIDM in cluster cores [325, 227] along with strong-lensing measurements of cluster halo shapes [231] set limits on the cross-section at $\sigma/m \lesssim 0.02 - 0.1$ cm^2/g. This effectively eliminates the cross section parameter space necessary to address the small-scale challenges previously discussed. Additional constraints from merging systems – specifically, the Bullet Cluster – place the cross-section at the level of $\sigma/m \lesssim 0.7 - 1.25$ cm^2/g [262, 214], again ruling out a large portion of the cross-section range of interest. However, more recent simulations with higher resolution have shown that the previous cluster based constraints were overly optimistic, and that cross-sections up to $\sigma/m \lesssim 1$ cm^2/g are still viable [268, 254]. Still, in order to both alleviate the small-scale structure challenges while abiding by the observational constraints, the interaction cross section must depend on the relative velocity of the particles [193, 138]. Thus, constraints on the SIDM cross-section are relevant at specific velocity (i.e. halo mass) scales, and complementary probes are needed from dwarf ($v \sim 10$ km/s) to galaxy ($v \sim 100$ km/s) to cluster scales ($v \sim 1,000$ km/s).

As noted earlier, dark matter self-interactions are expected to alter the shapes of DM halos, making them more spherical in comparison to their triaxial ellipsoidal CDM counterparts [254, 284, 115]. Therefore, measurements of the DM halos shapes – namely, the ellipticity ϵ – can be used to constrain the interaction cross-section. X-ray observations of elliptical galaxies offer a potentially powerful method of probing dark matter self-interactions at galactic scales. In Ref. [75, 81], it is shown that when certain conditions are met the X-ray emitting gas in ellip-

tical galaxies can be treated as a tracer of the overall gravitating matter. In Ref [81], this technique was employed using data from the Chandra X-ray telescope to demonstrate the existence of a triaxial DM halo in NGC 720 as well as to constrain the DM halo ellipticity [81]. Critical to the "X-ray Shape Theorem" approach [77, 78, 75] is the assumption that the X-Ray gas is in hydrostatic equilibrium. If the hydrostatic equilibrium assumption holds, then the relaxed X-ray emitting gas fills the gravitational potential well, taking on the three-dimensional shape of the DM dominated potential. By using X-ray observations to model the 3D shape of the gas, the 3D distribution of gravitating matter – roughly corresponding to the DM distribution – can be determined.

The measured ellipticities of these halos can then be compared to SIDM simulations. In the NGC 720 analysis [81] the DM ellipticity was found to be $\epsilon \approx 0.35 - 0.4$. SIDM Simulations performed in Ref. [254] considered a range of cross-sections (0, 0.1, 1 cm^2/g) and computed the ellipticities for simulated halos with masses of $\sim 10^{12} - 10^{13} M_\odot$. While the measured ellipticity of NGC 720 appears to be inconsistent with the $\sigma/m = 1$ cm^2/g, it does fall within the ellipticity distributions for the more moderate interaction strength of $\sigma/m = 0.1$ cm^2/g as well as for CDM. Of note however, is the fact that the ellipticity distributions contain significant scatter, making definitive statements on the cross-section difficult. This highlights the need for an analysis of an ensemble of galaxies rather than just the singular case of NGC 720 in order to draw more meaningful conclusions from this method. Several elliptical galaxies have been identified for which the hydrostatic approximation is suitable and for which there exists high-quality X-ray data (e.g. [184]). Performing the shape measurements on these galaxies can provide the observational information needed to compare with simulations in order to gain a more complete picture of viable DM self-interaction cross-sections.

1.5   Outline of the Dissertation

In the remainder of this dissertation, I discuss efforts to constrain properties of dark matter using astrophysical observations across the electromagnetic spectrum. Namely, these include searching for multiwavelength signals of DM annihilation and X-ray shape measurements of elliptical galaxies as a probe of dark matter self-interactions.

In chapter 2, I present the publicly available RX-DMFIT tool used for calculating the secondary multiwavelength emission from DM annihilation. First, I discuss the theory for the relevant radiative processes and the role of diffusion in the emission spectrum, and then examine the potential signals and constraints from interesting astrophysical targets for multiwavelength DM searches. In chapter 3 I study potential multiwavelength signals of DM annihilation in Andromeda in the context of recently detected gamma-ray emission in the central region of M31. I explore whether DM models consistent with the Milky Way GCE can also produce the observed M31 emissions, as well as the consistency in the DM annihilation spectrum for M31 at different frequencies compared to observational data. In chapter 4, I perform a similar analysis wherein instead of the observed emission originating from DM annihilation, I consider the possibility of a purely astrophysical origin. In this scenario, the multiwavelength spectrum of M31 originates from standard cosmic-ray populations, such as supernovae and pulsar wind nebulae. In chapter 5, I analyze a sample of isolated elliptical galaxies using data from the Chandra and XMM-Newton X-ray satellites and determine their X-ray ellipticity and surface brightness profiles. Invoking the hydrostatic equilibrium assumption, the X-ray images are used as a tracer of the gravitating potential and the shape of the total gravitating matter is determined. I then discuss the implication of these results for dark matter self-interactions. Finally, in chapter 6

I provide a brief summary of this work and the results, along with discussion of future directions for this research.

Chapter 2

Multiwavelength Analysis of Dark Matter Annihilation and RX-DMFIT

Note: The work in this chapter is adapted from "Multiwavelength analysis of dark matter annihilation and RX-DMFIT." by A. McDaniel, T. Jeltema, S. Profumo, and E. Storm in J. Cosmology Astropart. Phys., 9:027, September 2017.

2.1 Introduction

2.1.1 Background and Motivation

Proposed dark matter WIMP models can undergo self-annihilation yielding standard model particles such as quarks, leptons, and bosons, which can then decay into charged particles such as electrons and positrons. The presence of these particles in astrophysical systems leads to unique signatures across the electromag-

netic spectrum due to radiative processes such as synchrotron, inverse Compton (IC), bremsstrahlung, and Coulomb energy losses [106].

While there have been considerable efforts to study gamma-ray emission from dark matter annihilation in a variety of systems, e.g. [7, 9, 98, 116, 6, 5], a multiwavelength approach provides a complementary probe and in certain cases stronger constraints on dark matter properties [292, 293]. The synchrotron emission from these particles is the result of ambient magnetic fields that accelerate the charged particles, causing them to emit radiation at radio wavelengths. The IC radiation peaks at X-ray frequencies and is the result of photons from various radiation sources such as the CMB and starlight being up-scattered by the relativistic particles.

For a multiwavelength approach to indirect dark matter searches we focus on three main categories of astrophysical targets: galaxy clusters, local group dwarf galaxies, and other nearby galaxies (including the Milky Way Galactic Center). Galaxy clusters are the largest virialized objects in the universe and are highly dark matter dominated. These are enticing targets due to the large presence of dark matter as well as the presence of μG scale magnetic fields [144, 69, 163], enabling synchrotron processes. Dwarf spheroidal galaxies (dSphs) are also targets of great interest to dark matter searches. The proximity of the local group dwarfs along with their low luminosity and high concentration of dark matter make them prime targets for indirect dark matter searches [215, 294]. Particularly, dwarf spheroidal galaxies generally lack high radio and X-ray emission, which allow us to place stronger constraints on dark matter properties by analyzing the synchrotron and IC radiation from dark matter annihilation. Other interesting targets for dark matter searches include galaxies such as M31 [132, 134] or the Galactic center of the Milky Way [264, 200, 5]. These systems are thought to be rich in dark

matter, as well as to contain magnetic fields capable of producing synchrotron emissions from dark matter annihilation products. Particularly, reports of gamma-ray excesses in these systems [10, 116] that could potentially be due to the presence of dark matter make these compelling targets, since a gamma-ray signal from dark matter should be accompanied by radio and X-ray signatures. A difficulty with these targets however, is the presence of other astrophysical processes that can create signatures similar to what we would expect to see from dark matter.

In order to model the multiwavelength DM signal, besides the relevant radiative processes there are additional important effects such as spatial diffusion of the charged particles that require greater study. In former studies of galaxy clusters for instance, the role of diffusion has been estimated to be negligible [106], whereas in other systems such as dSphs it cannot be ignored [107]. The extent to which diffusion affects the analysis of a system is determined by factors including the physical size of the region, energy losses of the particles, and magnetic fields. For example, in larger environments such as galaxy clusters the particle byproducts of dark matter annihilation are able to lose all their energy within the region of study, whereas in smaller systems the energetic particles escape the system before fully radiating through synchrotron and IC processes. Additionally, the strong dependence on the magnetic field of synchrotron losses and diffusion effects means that uncertainties in the magnetic field must be examined before making assumptions on the role of diffusion.

To facilitate multiwavelength indirect dark matter searches in astrophysical systems, the main purpose of this work presented in this chapter is to introduce and describe the RX-DMFIT (Radio and X-ray - DMFIT) tool. RX-DMFIT is an extension of the DMFIT [188] tool developed by Jeltema & Profumo (2008) which is used for gamma-ray fitting. The RX-DMFIT code[1] is publicly available

---

[1]https://github.com/alex-mcdaniel/RX-DMFIT

and provides the user a tool with which to calculate the properties of secondary emission from dark matter annihilation due to synchrotron and IC processes. In particular, it relies on the DarkSUSY [165] Fortran package to provide the electron/positron injection spectrum for a given dark matter mass and annihilation channel. From the injection spectrum the RX-DMFIT tool calculates the emissivities and fluxes based on the user provided properties of the astrophysical system. Also, provided observational flux density data, RX-DMFIT can calculate dark matter particle constraints from synchrotron and IC radiation. The tool consists of 19 C++ files including 5 .h header files and interfaces with the DarkSUSY Fortran package. Integrations are carried out using the methods from the GNU Scientific Library [156]. Users have the ability to specify a multitude of system parameters including physical size of the system, magnetic field strength, dark matter density profile, and diffusion properties among others. In all, RX-DMFIT has roughly 15 different physical parameters to be manipulated.

This chapter is organized in the following manner. In section 2.2 we describe the analytic solution of the diffusion equation and subsequently derive the synchrotron and IC flux densities. In section 2.3 we assign and describe parameter values chosen for the models used in our analysis, which we then analyze using the RX-DMFIT tool in section 2.4 showing the effects of altering system components such as the role of diffusion and the magnetic field. In this section, we also demonstrate the use of the tool to place constraints on the DM particle cross-section using radio observations before presenting our conclusions in section 5.6. Throughout this chapter we assume a ΛCDM universe with $H_0 = 70.4$ km s^{-1} Mpc^{-1}, $\Omega_m = 0.272$, $\Omega_\Lambda = 0.73$. We note here that these cosmological parameters are fixed in RX-DMFIT, though they are readily accessible in the source code in case adjustments are desired.

2.2 Radiation From DM Annihilation

2.2.1 Diffusion Equation

In order to calculate the synchrotron and IC emission from DM annihilation, we must first obtain the equilibrium $e^{\pm}$ spectrum by solving the diffusion equation:

$$\frac{\partial}{\partial t}\frac{\partial n_e}{\partial E} = \boldsymbol{\nabla}\left[D(E,\mathbf{r})\boldsymbol{\nabla}\frac{\partial n_e}{\partial E}\right] + \frac{\partial}{\partial E}\left[b(E,\mathbf{r})\frac{\partial n_e}{\partial E}\right] + Q(E,\mathbf{r}). \tag{2.1}$$

Here $\partial n_e/\partial E$ is the equilibrium electron density, $Q(E,\mathbf{r})$ is our electron source term, $D(E,\mathbf{r})$ is the diffusion coefficient, and $b(E,\mathbf{r})$ is the energy loss term. We assume equilibrium and seek a steady state solution, thus we set the time dependence on the left hand side of the equation to zero. Our source term is given by,

$$Q\left(E,r\right) = \frac{\langle\sigma v\rangle\,\rho_{\chi}^2(r)}{2M_{\chi}^2}\frac{dN}{dE_{inj}}, \tag{2.2}$$

where we use the Fortran package DarkSUSY v5.1.2 to determine the electron/positron injection spectrum per dark matter annihilation event, dN/dE_{inj}, which is dependent on the DM particle mass, annihilation channel, and the source energy, E.

For the diffusion coefficient, we adopt a spatially independent form with a power law energy dependence. The RX-DMFIT tool includes two forms for the diffusion coefficient: a simplified power law in energy, and another that incorporates the degree of uniformity of the magnetic field. They are respectively:

$$D(E) = D_0 E^\gamma \tag{2.3a}$$

$$D(E) = D_0 \frac{d_B^{2/3}}{B_{avg}^{1/3}} E^\gamma, \tag{2.3b}$$

where d_B is the minimum uniformity scale of the magnetic field and D_0 is the diffusion constant [106, 105, 51].

In the full energy loss term we include contributions from synchrotron, inverse compton (IC), Coulomb, and bremsstrahlung losses. Each energy loss term is dependent on the energies of the electrons and positrons, as well as the magnetic field strength in the case of synchrotron losses and the CMB photon spectrum for IC losses. Additionally, the Couloumb and bremmstrahlung losses are dependent on the thermal electron density, n_e. The full energy loss expression is

$$\begin{aligned}
b(E, \mathbf{r}) &= b_{IC}(E) + b_{Synch.}(E, \mathbf{r}) + b_{Coul.}(E) + b_{Brem.}(E) \\
&= b_{IC}^0 E^2 + b_{Synch.}^0 B^2(r) E^2 \\
&\quad + b_{Coul.}^0 n_e \left(1 + \log \left(\frac{E/m_e}{n_e} \right) / 75 \right) \\
&\quad + b_{Brem.}^0 n_e \left(\log \left(\frac{E/m_e}{n_e} \right) + 0.36 \right).
\end{aligned} \tag{2.4}$$

Here n_e is the mean number density of thermal electrons. For high energy $e^\pm$ the synchrotron and IC losses are dominant.

A general analytic solution for equation 2.1 has previously been determined for the case of homogenous diffusion using the Green's function method [106, 162], which in general can also be applied to non-stationary sources. We are interested in the steady-state solution, and following the notation of Colafrancesco et. al.

(2006) [106] have a solution of the form,

$$\frac{\partial n_e}{\partial E} = \frac{1}{b(E,\mathbf{r})} \int_E^{M_\chi} dE' G\left(r, v(E) - v(E')\right) Q(E, \mathbf{r}).$$ (2.5)

where the Green's function, $G\left(r, v(E) - v(E')\right)$, is given by,

$$G(r, \Delta v) = \frac{1}{\sqrt{4\pi\Delta v}} \sum_{n=-\infty}^{\infty} (-1)^n \int_0^{r_h} dr' \frac{r'}{r_n} \left(\frac{\rho_\chi(r')}{\rho_\chi(r)}\right)^2$$
$$\times \left[\exp\left(-\frac{(r'-r_n)^2}{4\Delta v}\right) - \exp\left(-\frac{(r'+r_n)^2}{4\Delta v}\right)\right].$$ (2.6)

As in previous work [106, 24], we impose the free escape boundary condition at the radius of the diffusion zone, r_h, using the image charge method with charges placed at $r_n = (-1)^n r + 2nr_h$. Information about both the diffusion coefficient and energy loss terms have been incorporated into the $\Delta v = v(E) - v(E')$ term, where $v(E)$ is:

$$v(E) = \int_E^{M_\chi} d\tilde{E} \frac{D(\tilde{E})}{b(\tilde{E})}.$$ (2.7)

Here $\sqrt{\Delta v}$ has units of length and gives the mean distance traveled by an electron as it loses energy between its source energy, E', and interaction energy, E. Note that in order to derive the Green's function for the diffusion equation using the method of Colafrancesco et. al. (2006) a spatially independent magnetic field is needed. For evaluation of the Green's function we approximate the energy loss term, $b(E, \mathbf{r}) \approx b(E)$ by using an average magnetic field strength. That is, in equation 4.8 we take,

$$b_{Synch.}(E) \approx b_{Synch.}^0 B_{avg}^2 E^2.$$ (2.8)

This approximation is used only in the evaluation of the Green's function, whereas for the energy loss term outside the integral of equation 4.12 we incorporate the

full spatial profile of the magnetic field.

2.2.2 Synchrotron

The electrons and positrons produced as a result of dark matter annihilation produce multiwavelength emission through a variety of radiative processes. For instance, in the presence of reasonably strong magnetic fields (i.e. $B > B_{CMB} \simeq 3.25(1+z)^2 \mu G$) energy losses of the relativistic electrons and positrons are dominated by radio synchrotron radiation. From [293, 209] we have the synchrotron power for a frequency ν averaged over all direction as:

$$P_{syn}\left(\nu, E, r\right) = \int_0^\pi d\theta \frac{\sin\theta}{2} 2\pi \sqrt{3} r_0 m_e c \nu_0 \sin\theta F\left(\frac{x}{\sin\theta}\right), \qquad (2.9)$$

where $r_0 = e^2/(m_e c^2)$ is the classical electron radius, θ is the pitch angle (i.e. the angle between the particle velocity and the magnetic field [56]), and $\nu_0 = eB/(2\pi m_e c)$ is the non-relativistic gyrofrequency. The x and F terms are defined as,

$$x \equiv \frac{2\nu\left(1+z\right)m_e^2}{3\nu_0 E^2}, \qquad (2.10)$$

$$F(s) \equiv s \int_s^\infty d\zeta K_{5/3}\left(\zeta\right) \simeq 1.25 s^{1/3} e^{-s} \left[648 + s^2\right]^{1/12}, \qquad (2.11)$$

where $K_{5/3}$ is the Bessel function of order 5/3. The synchrotron emissivity at a frequency ν is found by folding the synchrotron power and electron equilibrium spectrum:

$$j_{syn}\left(\nu, r\right) = 2\int_{m_e}^{M_\chi} dE \frac{dn_e}{dE}\left(E, r\right) P_{syn}\left(\nu, E, r\right). \qquad (2.12)$$

From this we calculate the integrated flux density spectrum, which we find by taking the line of sight integral of the emissivity to find the surface brightness, then subsequently integrate the surface brightness over the solid angle of the emission region. This gives us:

$$S_{syn}(\nu) = \int_\Omega d\Omega \int_{los} dl j_{syn}(\nu, l).$$ (2.13)

Approximating the target as a small region with much greater distance than size gives the final result:

$$S_{syn} \approx \frac{1}{D_A^2} \int dr r^2 j_{syn}(\nu, r),$$ (2.14)

where D_A is the angular diameter distance.

2.2.3 Inverse Compton

For regions with lower magnetic fields, the dominant radiative process is inverse Compton (IC) scattering of background photons, including most prominently the 2.73K Cosmic Microwave Background photons. Relativistic electrons and positrons from dark matter annihilation scatter the ambient CMB photons, producing a spectral peak between the soft to hard X-ray bands depending on the mass of the dark matter particle [190]. With the photon number density $n(\epsilon)$, and the IC scattering cross-section $\sigma(E_\gamma, \epsilon, E)$, the IC power is:

$$P_{IC}(E_\gamma, E) = cE_\gamma \int d\epsilon\, n(\epsilon)\, \sigma(E_\gamma, \epsilon, E).$$ (2.15)

Here ϵ is the energy of the target CMB photons, E is the energy of the relativistic electrons and positrons, and E_γ is the energy of the upscattered photons.

$\sigma\left(E_\gamma, \epsilon, E\right)$ is given by the Klein-Nishina formula:

$$\sigma\left(E_\gamma, \epsilon, E\right) = \frac{3\sigma_T}{4\epsilon\gamma^2} G\left(q, \Gamma\right), \tag{2.16}$$

where σ_T is the Thomson cross-section and $G(q, \Gamma)$ is given by [56]:

$$G(q, \Gamma) = \left[2q \ln q + (1 + 2q)(1 - q) + \frac{(2q)^2(1 - q)}{2(1 + \Gamma q)}\right], \tag{2.17}$$

where,
$$\Gamma = \frac{4\epsilon\gamma}{m_e c^2} = \frac{4\gamma^2\epsilon}{E}, \qquad q = \frac{E_\gamma}{\Gamma(E - E_\gamma)} \tag{2.18}$$

For this process, the range of values of q is determined by the kinematics of the problem to be $1/\left(4\gamma^2\right) \leq q \leq 1$ [106, 56, 273]. As with the synchrotron emission, we find the local emissivity by folding the power with the electron equilibrium density,

$$j_{IC}\left(E_\gamma, r\right) = 2 \int_{m_e}^{M_\chi} dE \frac{dn_e}{dE}\left(E, r\right) P_{IC}\left(E, E_\gamma\right), \tag{2.19}$$

and the (approximate) integrated flux density is:

$$S_{IC} \approx \frac{1}{D_A^2} \int dr r^2 j_{IC}(E_\gamma, r), \tag{2.20}$$

2.3   Parameter Selection

In the following sections we describe and assign the various parameters required to define our target, and present the results of radiation from DM annihilation as calculated by RX-DMFIT. We will demonstrate the use of RX-DMFIT by performing our analysis on three scales: A cluster scale model emulating the Coma cluster, where we assume a redshift $z = 0.0232$ and diffusion zone $r_h = 415$ kpc [292]; a dwarf spheroidal model similar to the Draco dwarf with redshift

corresponding to a distance of 80 kpc [195] and a diffusion zone $r_h = 2.5$ kpc [107]; and finally a galactic scale model similar to M31 at a distance 780 kpc [4] and with a diffusion zone radius of $r_h = 30$ kpc borrowing from analysis of the Milky Way [296].

2.3.1 Magnetic Field Model

The RX-DMFIT tool currently supports two magnetic field models. These are

$$B(r) = B_0 \, e^{-r/r_c} \tag{2.21a}$$

$$B(r) = B_0 \left[1 + \left(\frac{r}{r_c} \right)^2 \right]^{-1.5\beta\eta}, \tag{2.21b}$$

where B_0 is the central magnetic field strength and r_c is the core radius of the target system.

Clusters: The presence of large scale magnetic fields in galaxy clusters has been demonstrated through various methods such as observations of radio halos, purported inverse compton X-ray emission, and Faraday Rotation Measures (FRM) among others [169]. The typical ranges that have been determined for magnetic field strength in non-cool-core clusters based on FRMs are $\sim$ 1-10 μG, whereas clusters with cool cores have been found to host magnetic fields in the range of $\sim$ 10-40 μG [90]. In our analysis we explore both a "non-cool-core" (NCC) model and a "cool-core" (CC) model. A prototypical and well-studied NCC cluster is the Coma cluster, with a reported central magnetic field of $B_0 = 4.7\mu$G and $r_c = 291$ kpc [58]. For the CC cluster model, the Perseus cluster provides the prototypical example with a field strength $B_0 = 25\mu$G [302] and core radius $r_c = 46$ kpc [292]. CC clusters typically have higher central fields with steeper

profiles whereas the NCC clusters tend to host lower strength, shallow field pro-
files. These differences are generally attributed in part to major mergers of NCC
clusters that destroy the cool core [182, 82]. In both the NCC and CC systems
we adopt the the beta model magnetic field profile of equation 2.21b. This choice
of the profile is motivated by simulations [236] along with observations of clusters
such as Coma [58] that suggest magnetic fields in clusters scale with the thermal
gas density which is often modeled with a beta-model [95]. We also include the
free-parameter η as in previous cluster magnetic field modeling [58, 314]. The β
and r_c parameters are typically fit by X-ray observations [99], whereas η is usually
fit using FRMs [314]. While the values for β and η are easily adjusted by the user
in RX-DMFIT we will adopt $\beta = 0.75$ and $\eta = 0.5$ throughout our calculations,
noting that the effect of varying these parameters is minimal [293].

dSphs: Previous explorations of the magnetic field present in dSph galaxies
show that any fields present would be relatively small, with most estimates for the
magnetic field strength being $B_\mu \sim 1\mu$G [283, 107], although some estimates are
as large as $B_\mu \sim 2\mu$G for dwarfs in the outer regions of the Milky Way magnetic
field [238]. For our purposes we will adopt the more conservative estimates of
a central strength $B_\mu = 1\mu G$. The spatial profile of magnetic fields in dwarfs
is similarly poorly defined, leading us to adopt the simple exponential model of
equation 2.21a. For the estimate of the core radius we take the half-light radius
of Draco to be $r_c = 0.22$ kpc [217].

Galaxies: The magnetic fields structure in galaxies is often considerably more
complex than considered in this analysis. However, for our purposes we again
employ the exponential model given by equation 2.21a for the magnetic field,
while noting that a full treatment of the magnetic fields structure in galaxies can
potentially impact the resulting synchrotron emission. Values for the magnetic

	ρ_s (GeV/cm^3)	r_s (kpc)	Ref.
Cluster	0.0399	404	[292]
dSph	1.40	1	[107]
Galaxy	0.184	24.42	[70]

Table 2.1: Dark matter density parameters of each system for an NFW profile.

field in the centermost region of M31 have been reported to be up to 15 μG [174]. Using a core radius of 10 kpc [296], this value provides us with an average field strength of ~ 4.8 μG in our model which is consistent with previous studies of M31 [160].

2.3.2 Dark Matter Profile

The DM profile modeling supports user-selection of the Navarro-Frenk-White (NFW) profile [240, 241], as well as the Einasto profile [136, 242] in the forms,

$$\text{NFW: } \rho\left(r\right) = \frac{\rho_s}{\left(\frac{r}{r_s}\right)\left(1 + \frac{r}{r_s}\right)^2} \tag{2.22}$$

$$\text{Einasto: } \rho\left(r\right) = \rho_s \exp\left\{-\frac{2}{\alpha}\left[\left(\frac{r}{r_s}\right)^\alpha - 1\right]\right\}. \tag{2.23}$$

In the RX-DMFIT code, users supply relevant characteristic density, ρ_s, and radius, r_s, as well as the α parameter for the Einasto profile. In this chapter we will restrict our analysis to mainly make use of the NFW profile, and use the same NFW density and radius values for both the NCC and CC cluster models. The parameters chosen for each example system with references are summarized in table 2.1.

2.3.3 Diffusion Parameters

Due to the lack of concrete values for diffusion in the different systems being studied here, we adopt the same initial parameters across our cluster, dwarf, and galaxy models. In the following sections we will vary these parameters and see to what extent the role of diffusion is important on different astrophysical scales.

For diffusion modeling in this chapter we will restrict ourselves to the simple power law in equation 2.3a. Most values for appropriate D_0 are based on studies of the Milky Way and fall in the range of 10^{27} - 10^{29} cm^{2}s^{-1} [322, 24, 70]. Constraints on the Milky Way diffusion parameters have been determined based on measured B/C data in the galaxy [322, 216]. We can also consider the D_0 parameter in terms of its relation to the inhomogeneity of the magnetic field in order to understand how it scales with the size of the system. Estimates for the diffusion constant can be found by assuming $D_0 \sim V_L L$, where V_L is the amplitude of the turbulent velocity and L is the scale of the turbulent motions [201, 189]. Scaling these parameters for dwarf spheroidals, normal galaxies, and galaxy clusters provides diffusion constant values compatible with the range above. Furthermore, the overall size of the system and the magnetic field strength play a role in whether or not diffusion has a significant impact on the resulting emission. In cluster sized systems, the length scale over which the electron/positrons lose their energy, given by $\sqrt{\Delta v}$, will typically be less than the diffusion zone r_h. In contrast, relativistic particles in smaller systems such as Milky Way sized galaxies and dwarf spheroidals will be able to escape the diffusion zone before radiating their energy. In each of these systems, greater magnetic field strength will result in the relativistic particles radiating their energy more quickly before escaping the system. These effects can also be considered in terms of the relevant timescales for each energy loss process in comparison to the timescale for diffusion, with a useful

example provided in figure A.3 of Appendix A of [106]. While there is a lack of studies into values for the diffusion constant in other astrophysical systems, the range of 10^{27} - 10^{29} cm^{2}s^{-1} provides reasonable estimates that we can apply to our models.

Following previous work [106] we assign $\gamma = 1/3$ and take the parameter values for the energy loss coefficients in equation 4.8 to be $b^0_{syn} \simeq 0.0254$, $b^0_{IC} \simeq 0.25$, $b^0_{brem} \simeq 1.51$, and $b^0_{Coul} \simeq 6.13$, all in units of 10^{-16} GeV/s. Additionally, we also must select appropriate values for the average thermal electron density, n_e. For our cluster models we take $n_e \approx 10^{-3}$ [292], $n_e \approx 10^{-6}$ [107] for dwarf spheroidals, and estimate $n_e \approx 0.1$ [145] for our galaxy model.

2.4 Application and Results

2.4.1 Diffusion Effects

We show the results of the SED and emissivity calculations using the RX-DMFIT tool. In figures 2.1, 2.2, and 2.3 we show the multiwavelength SED for each of of our main systems, assuming the $b\bar{b}$ annihilation channel dominates and including contributions from IC and synchrotron processes with various values for the diffusion constant D_0. To compare with the expected synchrotron and IC fluxes, in figures 2.1, 2.2, 2.3, and 2.5 we also include the expected prompt gamma-ray emission due to the decay of neutral pions. Note that this emission is not affected by the magnetic field or diffusion parameters, simplifying the flux calculation (see for instance [106, 264]). For clarity, we do not include the gamma-ray fluxes in the SEDs of figures 2.4 and 2.7.

Figure 2.1 shows a comparison of the SED for our CC and NCC cluster models. The CC model contributes more from synchrotron radiation due to its stronger

magnetic field, whereas the decreased synchrotron emission in the NCC model leads to comparatively higher IC emissions. In both the CC and NCC models we do not observe significant impact of spatial diffusion for even the largest diffusion values of $D_0 = 3 \times 10^{29}$ cm^{2}s^{-1} , which is consistent with previous estimations of the diffusion effect in galaxy clusters [106]. To help illustrate this point, in the right panel of figure 2.1 we show the ratio of flux density from synchrotron radiation in our cluster models with diffusion versus without diffusion over a range of frequencies. In both the CC and NCC models there is at most a $\sim 2\%$ decrease when considering our highest diffusion strength. In the case of dSphs, we see in figure 2.2 that diffusion at all included D_0 values plays a significant role in decreasing the total emission of both the synchrotron and IC radiation as the relativistic particles escape the diffusion region before radiating. In figure 2.3 we show the SED of our galaxy model. Here we observe a decrease in synchrotron emission at each D_0 value, however this is considerably less than in the dwarf model. For instance, the lowest diffusion constant value $D_0 = 3 \times 10^{27}$ cm^{2}s^{-1} yields an essentially negligible decrease in synchrotron emission. Even at the highest value of $D_0 = 3 \times 10^{29}$ cm^{2}s^{-1} there is only about a factor of two decrease in the synchrotron emission, in contrast to the roughly three order of magnitude decrease in the dwarf model for this diffusion value. We also note that the decrease in synchrotron emission is accompanied by a slight increase in the IC emission for our galaxy model. As the relativistic particles diffuse into regions of diminished magnetic field within the diffusion zone, IC emission scattering from the uniform CMB photon distribution becomes the dominant form of radiation.

We also consider a variety of particle models for dark matter annihilation wherein different channels dominate. In figure 2.4 we show the SED for our dwarf system under various assumptions for the DM annihilation channel. We note a
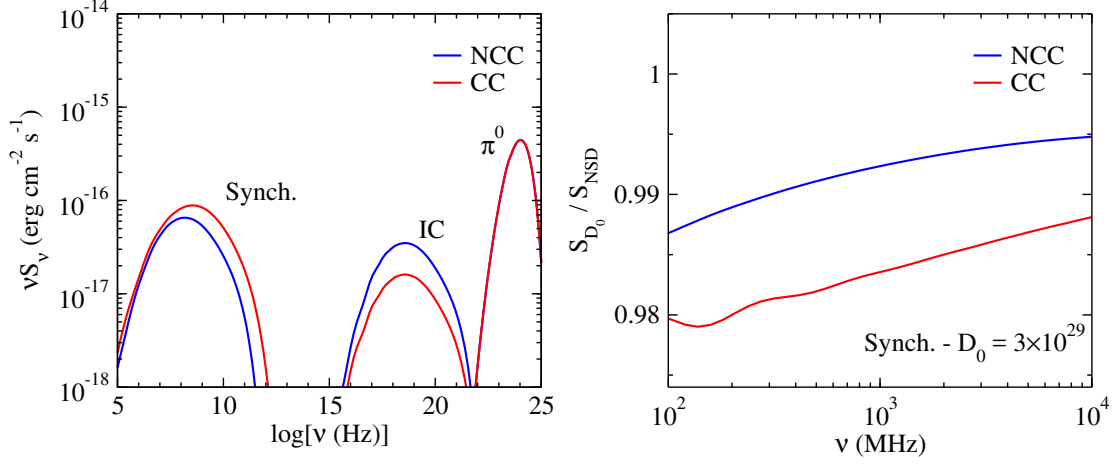
Figure 2.1: Left: SED comparing the "non-cool-core" (NCC) and "cool-core" (CC) cluster models assuming a $b\bar{b}$ final state with $M_\chi = 100$ GeV. Here we use only the limit of no spatial diffusion (NSD). Right: Ratio of synchrotron flux with $D_0 = 3 \times 10^{28}$ cm^{-3}s^{-1} over the NSD limit for the NCC and CC cluster models.
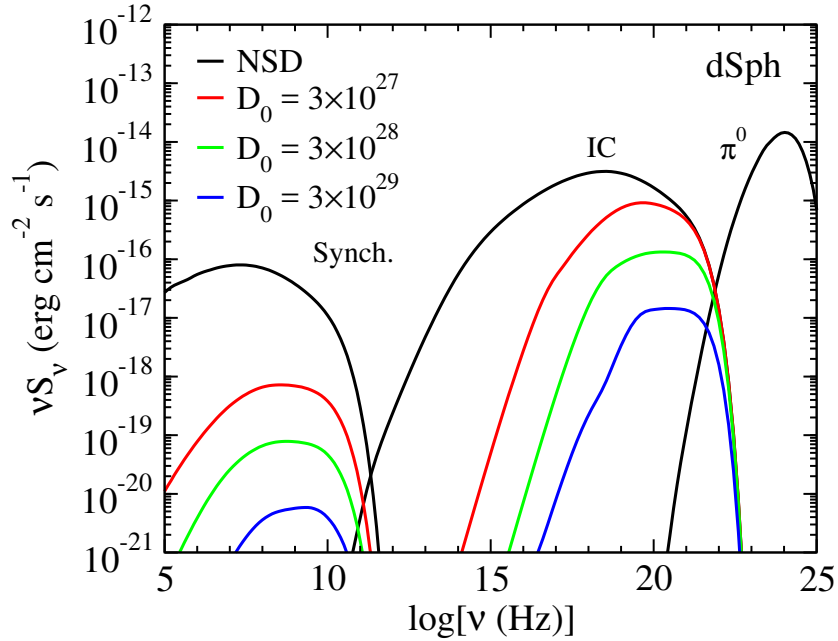
Figure 2.2: SED of the dwarf model assuming a $b\bar{b}$ channel with $M_\chi = 100$ GeV for multiple values of D_0 in cm^2 s^{-1}.
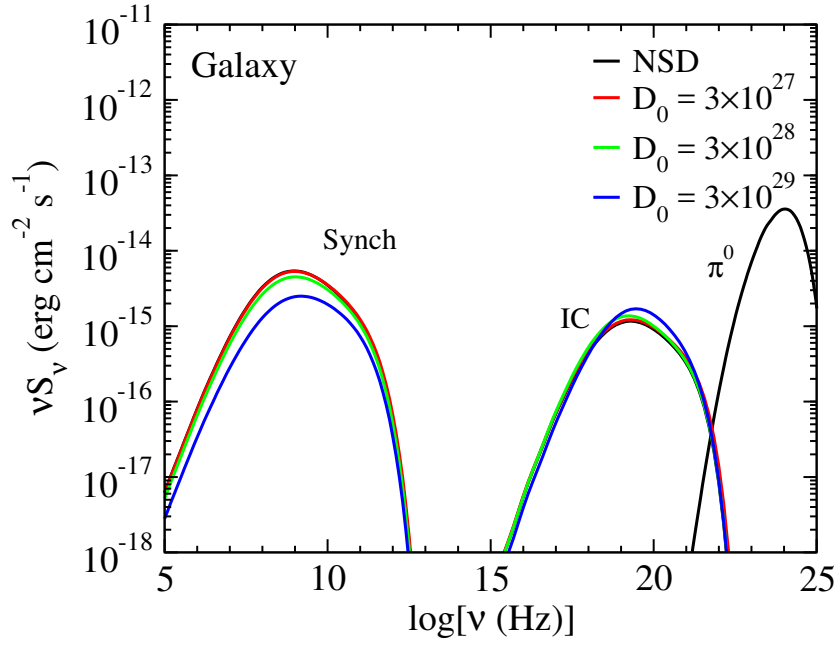
Figure 2.3: SED of the galaxy model assuming a $b\bar{b}$ channel with $M_\chi = 100$ GeV for multiple values of D_0 in cm^2 s^{-1}. Note that in the plot there is almost no noticeable difference between the NSD limit and the lowest diffusion values of $D_0 = 3 \times 10^{27} - 3 \times 10^{28}$ cm^{2}s^{-1}.
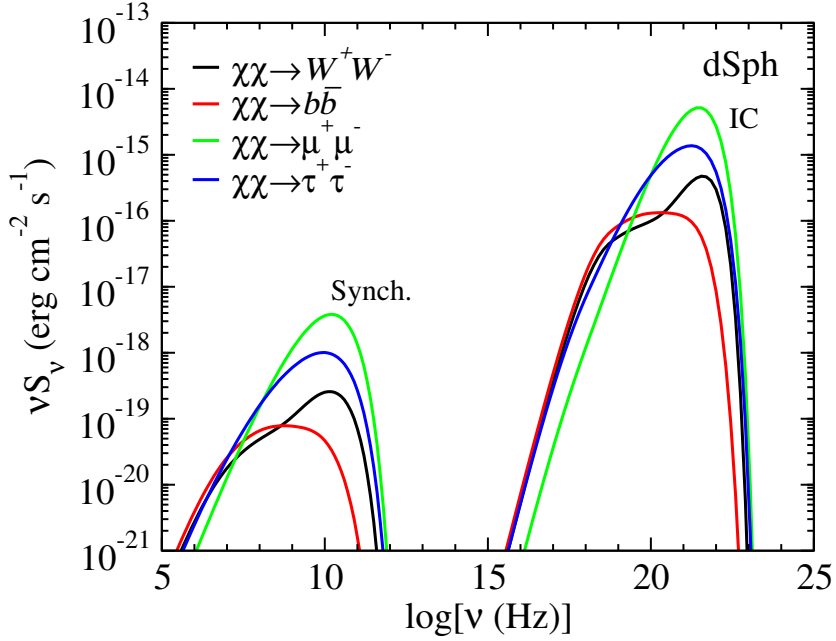
Figure 2.4: SED of the dwarf model with $M_\chi = 100$ GeV for various annihilation channels assuming a diffusion constant of $D_0 = 3 \times 10^{28}$ cm^{-3}s^{-1}.

harder spectrum for the leptonic $\mu^+\mu^-$ and $\tau^+\tau^-$ states than for the $b\bar{b}$ state, and a flatter spectrum for the W^+W^- state. While the leptonic states have spectra that tend to slant more towards higher energies than the $b\bar{b}$ channel, the W^+W^- channel combines aspects of both the leptonic spectra and the $b\bar{b}$ spectra due to the W^+W^- decay into pions and leptons, resulting in a flattened spectral profile. Furthermore, as seen in figure 2.5, increased diffusion tends to diminish this effect as the hard spectrum of the W^+W^- channel becomes more prominent. The predicted SED is also affected by other properties of the dark matter particle model such as the cross-section and particle mass. Changing the DM particle cross-section only changes the overall normalization since the emission is directly proportional to the $\langle \sigma v \rangle$ by equation 3.2. Varying the DM particle mass on the other hand will affect the shape and location of the spectrum, with higher M_χ values producing harder spectra.

Diffusion effects can be seen more clearly by looking at the spatial local emissiv-
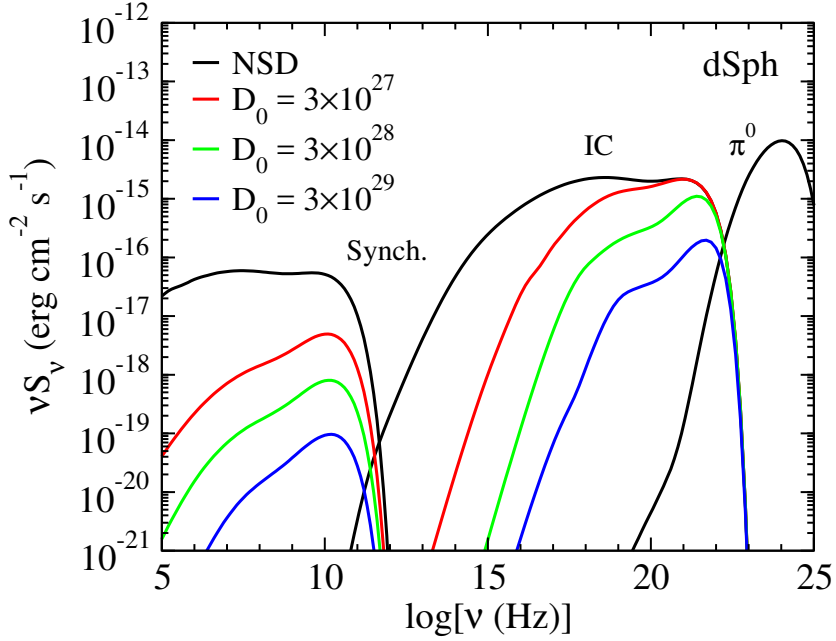
Figure 2.5: SED of the dwarf model with $M_\chi = 100$ GeV and DM annihilation through the W^+W^- channel for multiple values of D_0 in cm^2 s^{-1}.

ity profile for synchrotron and IC emission. In figure 2.6 we show the synchrotron and IC emissivity profiles for our NCC, dwarf, and galaxy models with various diffusion constant values. In our NCC model, introducing diffusion causes a slight decrease in the innermost region of the cluster which quickly returns to the NSD limit. For instance in the case of the the highest diffusion value of $D_0 = 3 \times 10^{29}$ cm^{2}s^{-1} the synchrotron profile approaches the NSD limit at ~ 10 kpc and the IC emission reaches the NSD limit at ~ 40 kpc. Furthermore, in neither case do we observe a considerable increase in emission along the profile. The NCC emissivity profiles are consistent with the lack of variation observed in the SEDs for the different D_0 values.

For our dwarf and galaxy models, including diffusion results in a large decrease in both synchrotron and IC emission for the central regions of each system. This depletion of emission is greater in the dwarf model than in the galaxy model, consistent with the SEDs of each system. We also note that diffusion leads to

a slight excess in synchrotron emission in the outer regions of our dwarf system for the lower D_0 values. This excess is also present in the galaxy model for every D_0 value shown and for a larger portion of the diffusion zone. For instance, with a diffusion constant value of $D_0 = 3 \times 10^{27}$ cm^{2}s^{-1} the synchrotron emission of the dwarf reaches the NSD limit at ~ 0.5 kpc in comparison to $r_h = 2.5$ kpc, whereas the the galaxy model reaches NSD limit at ~ 0.9 kpc compared to $r_h = 30$ kpc. Both models also exhibit a flattened IC emission profile. In contrast to the synchrotron emission that depends on the radially dependent magnetic field, the IC emission depends on the spatially constant CMB photon distribution, leading to a flatter emission profile as the relativistic particles diffuse outward. While the dwarf model yields a slight excess of IC emission for the lowest diffusion strength, the galaxy model has a small excess in the outer regions for all diffusion values, providing the increase in IC emission observed in figure 2.3.

2.4.2   Magnetic Fields

Our ability to detect radio signals of from dark matter annihilation depends significantly on the magnetic field present in the system. In figure 2.7 we again show the multiwavelength SED for each of our models, this time varying central magnetic field strength in each case. We assume a diffusion constant value of $D_0 = 3 \times 10^{28}$ cm^{2}s^{-1} for the dwarf and galaxy models, and assume no spatial diffusion for the NCC and CC cluster models.

In each model, the magnetic field strength drastically impacts the the total synchrotron emission. For instance, decreasing the field strength on the dwarf model from $B_0 = 1$ μG to $B_0 = 0.1$ μG causes a decrease in the synchrotron radiation by roughly two orders of magnitude. For IC emissions, all of our models except the dSphs show significant dependence on the magnetic field strength,
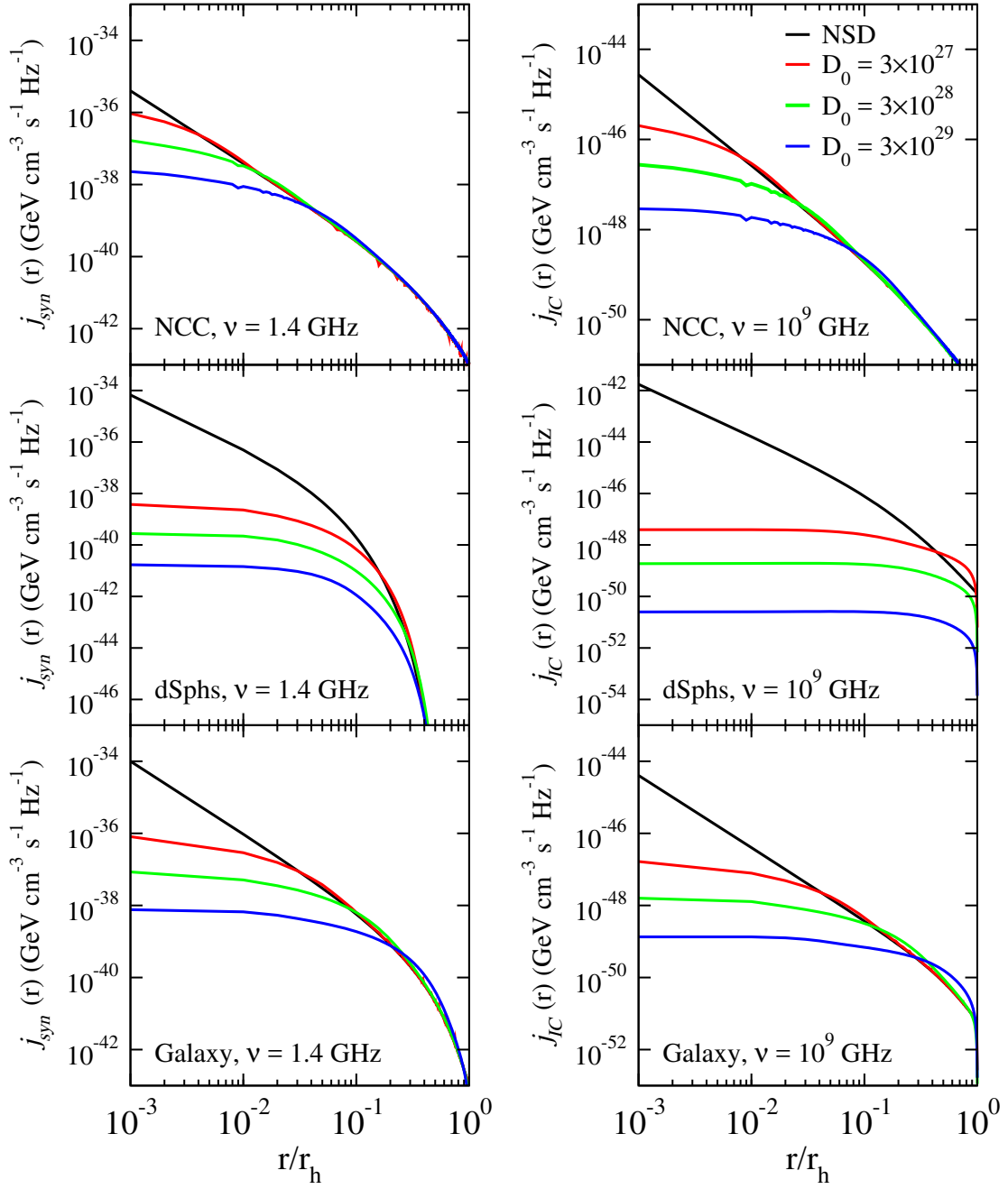
Figure 2.6: Predicted synchrotron (*left*) and IC (*right*) local emissivity profiles for the NCC, dSph, and galaxy models for an observing frequency ν (note that 10^9 GHz ≈ 4 keV) and various D_0 values. Our particle model assumes a dominant $b\bar{b}$ final state and a mass $M_\chi = 100$ GeV.
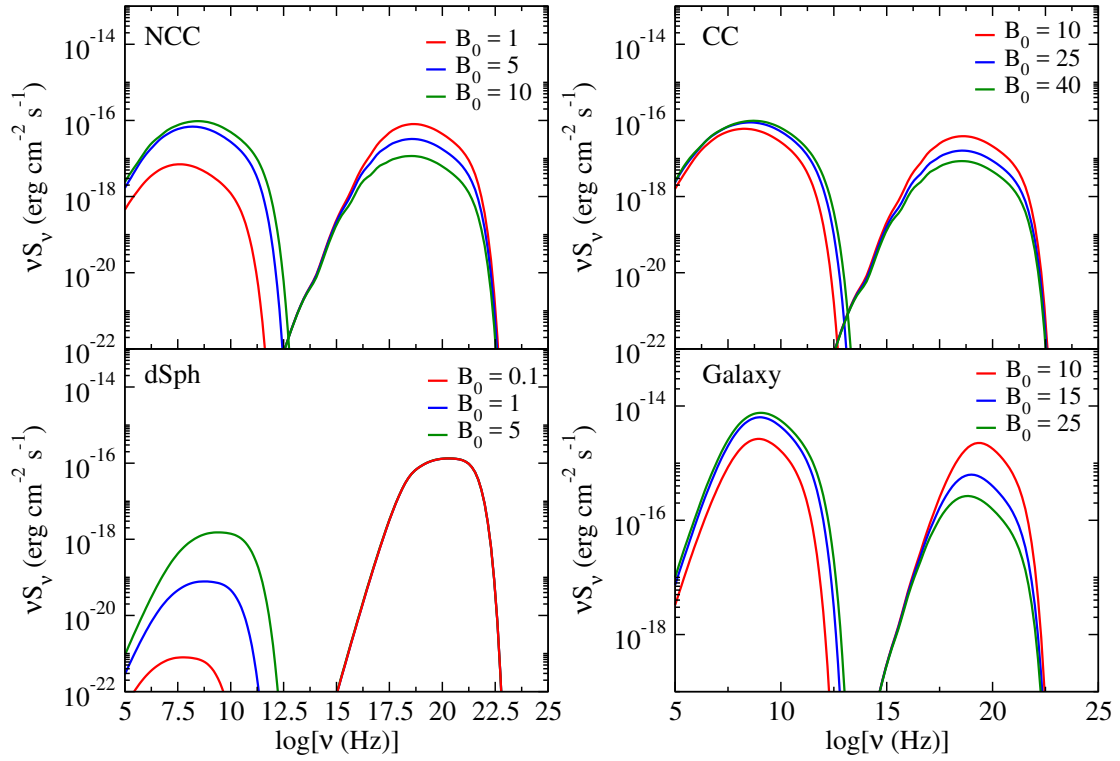
Figure 2.7: SED for each model assuming a $b\bar{b}$ final state, with $M_\chi = 100$ GeV, and $D_0 = 3 \times 10^{28}$ cm²s^{-1} (except for the NCC and CC models, in which diffusion is ignored) for multiple values of B_0 in μG. In the case of the dSph. model, while each B_0 value is shown there is no discernable difference in the IC SED.

although with an inverse relationship. That is, lower magnetic field strengths in the galaxy and cluster systems lead to IC processes making up a greater portion of the total energy loss of the electrons and positrons. So while IC losses do not explicitly depend on magnetic field strength, systems with lower magnetic fields provide greater potential for IC radiation. For the NCC cluster model, we see that an order of magnitude increase in the magnetic field from $B_0 = 1$ to $B_0 = 10$ roughly translates into an even greater increase in radio emission, while decreasing the IC emission. In the CC cluster model there is less of a dependence on the central field strength, as shown by only a factor of ~ 2 increase in synchrotron emission and factor of ~ 4 decrease in IC emission from a factor of 4 increase in the magnetic field strength from $B_0 = 10$ μG to $B_0 = 40$ μG. The weaker dependence on the central magnetic field in the CC clusters versus the NCC cluster can be attributed to the smaller core radius of CC clusters. The steeper profiles of the CC clusters lead to a greater share of the synchrotron emission being confined to the inner regions of the clusters in comparison to the NCC clusters, meaning that altering the central field strength will have a lesser impact on the total emission in CC clusters than in NCC clusters.

2.4.3 Dark Matter Constraints from Synchrotron Radiation

Limits on the DM cross-section can also be determined using observed diffuse radio emission. To do this, we note that the flux density from dark matter given by equation 3.17 is directly proportional to the thermal averaged DM particle cross-section through the source term given in equation 3.2. Thus we can express the flux density as:

$$S_\chi = \frac{\langle \sigma v \rangle}{M_\chi^2} S'_\chi, \tag{2.24}$$

Segue I Parameters	
r_h	1.6 kpc
d	23 kpc
D_0	3×10^{26} cm^{2}s^{-1}
γ	0.7
B_0	2 μG
η	0
ρ_s	6.6 GeV/cm^3
r_s	0.15 kpc
α	1/3

Table 2.2: Parameter selection for Segue I model.

where we have simply extracted the $\langle \sigma v \rangle$ dependence from the calculated flux density due to DM annihilation. We can then compare this quantity to an observed flux density for the system we are modeling and derive a constraint on the dark matter particle cross-section from,

$$\langle \sigma v \rangle = \frac{S_{obs}}{S'_\chi} M_\chi^2. \tag{2.25}$$

Here we present a practical example using RX-DMFIT wherein we derive dark matter constraints using radio data reported in Natarajan et. al. (2015) [238] from $\nu = 1.4$ GHz observations of the Segue I dwarf galaxy with the Green Bank Telescope. From their analysis they find an upper limit flux density of ~ 0.57 Jy for a region of radius $\sim 4°$. The physical parameters that we input into RX-DMFIT are taken from Natarajan et. al. (2015) [238] and are summarized table 2.2, with any parameters that are not listed unchanged from our earlier dwarf model. Note that for consistency with Natarajan et. al. (2015) [238], we set β (or
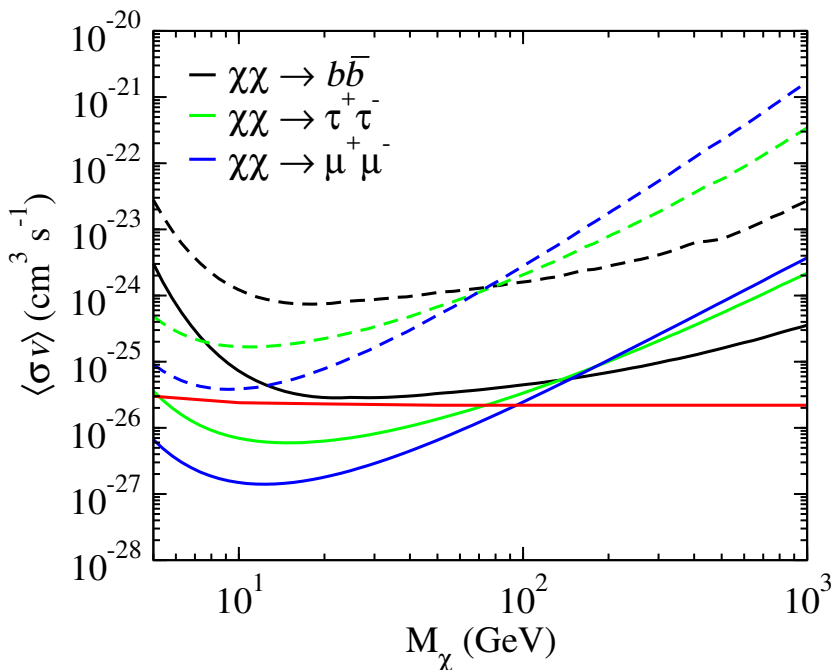
Figure 2.8: Constraints on the DM particle cross-section from radio observations of the Segue I dwarf galaxy for various annihilation channels and diffusion strengths. The solid lines indicate a diffusion constant of $D_0 = 3 \times 10^{26}$ cm^{2}s^{-1}, whereas the dashed lines indicate $D_0 = 3 \times 10^{28}$ cm^{2}s^{-1}. The red line is the thermal relic cross-section from Steigman et. al. (2012) [290].

equivalently, η) equal to zero in order to establish a constant magnetic field and employ the Einasto profile of 2.23, and thus include the α parameter. In addition to the fairly low diffusion value of $D_0 = 3 \times 10^{26}$ cm^{2}s^{-1}, we also consider a greater diffsuion constant value of $D_0 = 3 \times 10^{28}$ cm^{2}s^{-1}.

Figure 2.8 shows the upper limits on the annihilation cross-section for a variety of annihilation channels with and without diffusion. As we saw in the SED plots (see figures 2.2 and 2.5), diffusion has a significant impact on the expected radio synchrotron emission in dwarf spheroidal galaxies, and in turn, a significant impact on the strength of the constraints that can be placed on the DM particle. Increasing the diffusion constant from $D_0 = 3 \times 10^{26}$ cm^{2}s^{-1} to $D_0 = 3 \times 10^{28}$ cm^{2}s^{-1} weakens the constraints by an order of magnitude, and thus should not be
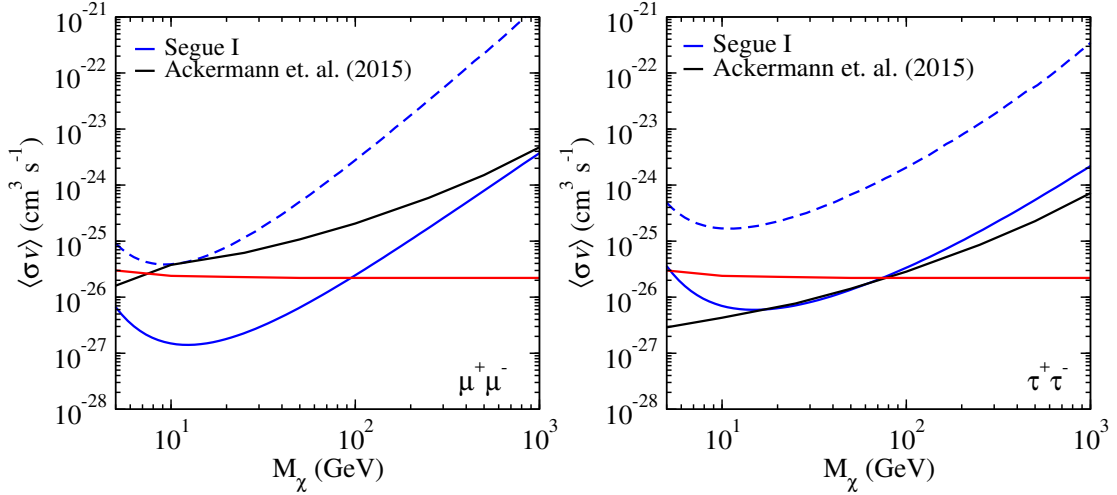
Figure 2.9: Constraints on the DM particle cross-section from radio observations of the Segue I dwarf galaxy in comparison to limits from Fermi gamma-ray data. The solid blue lines indicate a diffusion constant of $D_0 = 3 \times 10^{26}$ cm^{2}s^{-1}, whereas the dashed blue lines indicate $D_0 = 3 \times 10^{28}$ cm^{2}s^{-1}. The red line is the thermal relic cross-section from Steigman et. al. (2012) [290].

neglected for our dwarf system. We find the strongest constraints for annihilation through the $\mu^+\mu^-$ and $\tau^+\tau^-$ channels, both of which reach below the thermal relic cross-section value for WIMP masses $M_\chi \leq 100$ GeV under weak diffusion assumptions.

These constraints are competitive with previous studies of dark matter in dSphs using Fermi gamma-ray data [9] which provides some of the strongest dark matter constraints from gamma-rays to date. In figure 2.9 we compare the constraints placed on the dark matter cross-section from the combined gamma-ray observations of 25 Milky Way dSphs with six years of Fermi data [9]. For $\tau^+\tau^-$ final states, weak diffusion, and masses around 10 GeV, the constraints are very similar. In the case of $\mu^+\mu^-$ dominated final states, the radio approach provides similar constraints for masses near 10 GeV in the case of high diffusion where $D_0 = 3 \times 10^{28}$ cm^{2}s^{-1} . With our lower value of $D_0 = 3 \times 10^{26}$ cm^{2}s^{-1} radio

constraints are stronger for masses 5 GeV $\leq M_\chi \leq$ 1000 GeV including improvement upon the gamma-ray constraints by greater than an order of magnitude for masses 5 GeV $\leq M_\chi \leq$100 GeV. From these constraints we determine that dSphs are viable targets for indirect searches from dark matter annihilation by way of radio observations, and note that our results here are compatible with other radio constraints on dark matter annihilation. For instance, in the case of the Draco dwarf limits on the dark matter cross-section are in the range of $\langle \sigma v \rangle \sim 10^{-25}$ cm^{2}s^{-1} [283, 107]. Other radio constraints from the analysis of several dSphs [263] also are similar to the constraints found in this work.

We are also interested in deriving limits on the dark matter WIMP models using X-ray observations. In the case of galaxy clusters, future hard X-ray observations have the potential to contribute significantly to dark matter constraints [190]. Additionally, Jeltema & Profumo (2008) [189] have demonstrated that current and future X-ray observations of dwarf spheroidals can provide limits comparable and potentially better than limits from gamma-rays in a similar mass range as that for radio observation. However, these results rely on favorable assumptions for diffusion. More recently, there is deep X-ray data of the Draco dwarf that has been used for constraining dark matter decay [187] that can potentially provide stronger constraints on dark matter annihilation than those in [189] while making fewer assumptions about the diffusion and energy loss processes. In order to better understand the feasibility of obtaining dark matter constraints from X-rays in dwarfs we must take the X-ray background into account. For instance, recent Chandra results report cosmic X-ray background fluxes of $4.55^{+0.03}_{-0.03} \times 10^{-12}$ erg cm^2 s^{-1} deg^{-2} for the 1-2 keV ($\sim 2.4 - 4.8 \times 10^{17}$ Hz) energy range and $2.034^{+0.005}_{-0.006} \times 10^{-11}$ erg cm^2 s^{-1} deg^{-2} for the 2-10 keV ($\sim 4.8 - 24.0 \times 10^{17}$ Hz) range [85]. From figure 2.4 we see that the predicted X-ray fluxes from DM anni-

hilation in these energy ranges and for a 100 GeV DM particle are on the order of $\sim 10^{-16} - 10^{-14}$ erg cm^2 s^{-1}, depending on annihilation channel. The $\sim 2 - 5$ order of magnitude excess of the X-ray background over the predicted DM flux suggest that only conservative constraints can be placed without an improved understanding of the X-ray background or deeper X-ray observations.

2.5   Conclusion

We have presented RX-DMFIT, a new tool to analyze synchrotron and IC emission due to DM annihilation for the purposes of astrophysical indirect detection of dark matter. We considered four model systems: a "non-cool-core" as well as a "cool-core" galaxy cluster, a dwarf model, and a galaxy model. We discussed in detail the relevant astrophysical processes, namely diffusion of the charged particle byproducts of DM annihilation, magnetic field modeling, and radiative energy loss processes. We then used RX-DMFIT to examine the effect that varying these attributes of the astrophysical model has on the profile, spectrum, and total flux resulting from DM annihilation. Our results show that effects such as diffusion of charged particle byproducts can be ignored in the case of most large scale systems such as galaxy clusters, but can provide order of magnitude corrections in dwarfs and other galaxies under conservative assumptions for diffusion values. Additionally, we discussed the presence of X-ray radiation resulting from IC scattering of CMB photons as a secondary form of emission due to DM annihilation. We showed that the inclusion of diffusion effects can lead to relative increases in the X-ray band as relativistic electrons and positrons diffuse into regions of lower magnetic field, which can potentially provide new methods of searching for dark matter.

We used radio data of the Milky Way dSph Segue I to place constraints on

the dark matter particle cross-section and find the best limits at low masses with $\tau^+\tau^-$ and $\mu^+\mu^-$ final states. The $\mu^+\mu^-$ channel in particular provides the most stringent constraints. Assuming a low diffusion value of $D_0 = 3 \times 10^{26}$ cm^{2}s^{-1}, this annihilation channel provides limits below the canonical thermal relic cross-section for masses below 100 GeV, with constraints roughly an order of magnitude greater at $M_\chi \approx 10$ GeV. However, when assuming the more conservative value for the diffusion constant of $D_0 = 3 \times 10^{26}$ cm^{2}s^{-1} these constraints are diminished by a factor of $\sim 20 - 30$, demonstrating the impact of diffusion effects in smaller systems, and a need for a better understanding of diffusion in dwarfs. The constraints we found are competitive with previous analysis of dSphs using gamma-ray observations and, in the some cases such as the $\mu^+\mu^-$ final states with weak diffusion, considerably more stringent.

The RX-DMFIT tool offers a useful and versatile way to predict the synchrotron and inverse Compton emission from DM annihilations. This can aid in the design and planning of future observations by allowing the user to determine optimal observing frequencies and region sizes for dark matter searches. Also, the analysis performed by RX-DMFIT will be of great use in distinguishing astrophysical radio and X-ray signals from potential dark matter signals, particularly where diffusion effects have significant impact on the profile of emission due to dark matter annihilation. Radio and X-ray emission in astrophysical systems have the potential to provide highly competitive constraints on dark matter properties. Diffusion, magnetic field, and dark matter profile parameters all have significant impact on the expected radio and X-ray emission from dark matter annihilation, and better understanding of these features can greatly improve current constraints.

Chapter 3

A Multi-Wavelength Analysis of Annihilating Dark Matter as the Origin of the Gamma-Ray Emission from M31

Note: The work in this chapter is adapted from "Multiwavelength analysis of annihilating dark matter as the origin of the gamma-ray emission from M31." by A. McDaniel, T. Jeltema, S. Profumo, Phys. Rev. D, 97(10):103021, May 2018.

3.1 Introduction

Understanding the fundamental nature of dark matter remains one of the foremost problems in physics. Particle dark matter is arguably the best-supported explanation, and Weakly-Interacting Massive Particles (WIMPs) in particular have strong theoretical motivation as a potential candidate [43, 191, 37]. One of several possible methods for testing WIMP models of dark matter is through indirect de-

tection using astrophysical observations. In the case of annihilating dark matter, the byproducts of dark matter annihilation can include standard model particles such as quarks, leptons, and bosons, which then decay into particles that can be detected through a variety of observational experiments. For instance, the production of electrons and positrons can produce radio emission through synchrotron radiation in regions where magnetic fields are present, or X-rays and soft gamma-rays by up-scattering ambient photons through inverse Compton scattering. Additionally, dark matter annihilation is expected to produce prompt gamma-rays predominately from neutral pion (π^0) decay that have been a major focus of dark matter indirect detection searches. While the bulk of indirect searches for annihilating dark matter have been performed by studying these gamma-rays, several studies have shown that the radio [292, 293, 135, 97, 200, 264, 239, 283, 238, 107] as well as x-ray [190, 189, 264] approaches have the potential to place competitive and in some cases stronger constraints on dark matter in a variety of systems including galaxy clusters, dwarf galaxies, and the central regions of normal galaxies.

An especially enticing target for indirect dark matter searches is our own Galactic center, which has been widely studied in the context of dark matter due in part to its proximity as well as its high concentration of dark matter. Additionally, the presence of a gamma-ray excess in the inner galaxy known as the Galactic Center Excess (GCE) has been reported by several groups using Fermi-LAT data and could potentially be explained as a dark matter signal from annihilating WIMPs [166, 2, 83, 116, 167, 175] (or for a review see [11]). Other possible explanations for the GCE that have been explored include an unresolved population of millisecond pulsars (MSPs) [133, 26, 64] or additional cosmic ray sources [91, 154, 100]. Several of the dark matter interpretations have been shown to be consistent with observations for certain WIMP models, specifically for those annihilating through

$b\bar{b}$ and $\tau^+\tau^-$ channels with masses of $\sim 30-50$ GeV and $\sim 7-10$ GeV, respectively (see e.g. [2, 83, 116, 167, 175]).

A similar excess in the nearby Andromeda galaxy (M31) has been reported by the Fermi collaboration [10]. The dataset used in the analysis by Ackermann et. al. (2017) [10] includes 88 months of Pass 8 data collected between August 4, 2008, and December 1, 2015. SOURCE class events were used excluding those with zenith angle greater than 90° or rocking angle greater than 52°. Reconstructed events within an energy range 0f 0.1-100 GeV were considered as well as reconstructed directions within a $14° \times 14°$ region of interest (ROI) centered at $(\alpha, \delta) = (10°.6847, 41°.2687)$. For greater detail about the analysis we refer the reader to Ref. [10].

The results from this analysis motivate an examination of similar possible explanations of the observed excess as in the case of the GCE. Already there has been exploration into the MSP explanation for the M31 excess [133], where the point was made that MSPs are unlikely to be able to account for the entirety of the observed emission. In this chapter, we use the recently developed RX-DMFIT [220] tool to explore dark matter annihilation as a potential source of the observed excess, and consider the multi-wavelength emissions that would be expected due to synchrotron radiation, inverse Compton scattering of CMB and starlight photons, and π^0 decay and other prompt gamma-rays from dark matter annihilation. We particularly focus on the radio and gamma-ray aspects as they provide greater insight than the X-rays into the dark matter interpretation with current observational data. M31 has been the focus of some previous radio-only dark matter studies [135, 97] as well as an analysis comparing the DM induced gamma-ray emission in M31 with multi-wavelength emission in other systems [28]. Here however we study the full spectrum expected from dark matter annihilation

in M31 and we compare directly with data available in the literature in order to provide complementary probes of a dark matter interpretation for the gamma-ray emission from Andromeda. Our analysis thus provides a two pronged approach wherein we seek to determine whether the GCE dark matter particle models provide gamma-ray emissions consistent with the M31 observations, as well as whether potential dark matter particle models that could explain the M31 gamma-ray excess also predict radio and X-ray emissions "self-consistent" with available M31 observations.

This chapter is organized in the following manner. In section 4.2 we present our astrophysical model for M31, including relevant astrophysical model components such as the diffusion model parameter, the magnetic field, the dark matter density profile, and the interstellar radiation field (ISRF). We derive expressions for the synchrotron and inverse Compton emissions from DM annihilation in section 3.3, then describe our particle physics models in section 3.4. Our results comparing the expected emissions due to dark matter annihilation and the observational data are presented in section 5.5, and finally we conclude in section 5.6. Throughout this chapter we assume a ΛCDM universe with $H_0 = 70.4$ km s^{-1} Mpc^{-1} , $\Omega_m = 0.27$, $\Omega_\Lambda = 0.73$.

3.2 Astrophysical Modeling

3.2.1 Diffusion

The computation of expected emissions due to the injection of electrons and positrons from DM annihilation requires solving a diffusion equation of the type

$$\frac{\partial}{\partial t}\frac{\partial n_e}{\partial E} = \boldsymbol{\nabla}\left[D(E,\mathbf{r})\boldsymbol{\nabla}\frac{\partial n_e}{\partial E}\right] + \frac{\partial}{\partial E}\left[b(E,\mathbf{r})\frac{\partial n_e}{\partial E}\right] \\ + Q(E,\mathbf{r}), \tag{3.1}$$

where $\partial n_e/\partial E$ is the electron equilibrium spectrum and the source term from DM annihilation, $Q(E,\mathbf{r})$, is given by

$$Q\left(E,r\right) = \frac{\langle\sigma v\rangle\,\rho_\chi^2(r)}{2M_\chi^2}\sum_f BR_f\frac{dN}{dE_{inj}}, \tag{3.2}$$

where $\rho_\chi(r)$ is the DM density profile, M_χ is the DM mass, $\langle\sigma v\rangle$ is the thermally averaged annihilation cross-section, and dN/dE_{inj} is the $e^\pm$ injection spectrum through annihilation channels with branching ratios BR_f. The equation above makes several simplifying assumptions, including the absence of diffusive reacceleration and convection, and is well-defined once boundary conditions are specified; also, the factor 2 in the denominator of Eq. (3.2) implicitly assumes that the dark matter is its own antiparticle.

In the energy loss term $b(E,\mathbf{r})$ we include contributions from synchrotron radiation, inverse Compton scattering of CMB and starlight photons, Coulomb

interactions, and bremsstrahlung radiation, given by the expression

$$
\begin{aligned}
b(E, \mathbf{r}) &= b_{IC}(E) + b_{Synch.}(E, \mathbf{r}) + b_{Coul.}(E) + b_{Brem.}(E) \\
&= b_{IC}^0 u_{CMB} E^2 + b_{IC}^0 u_{SL} E^2 + b_{Synch.}^0 B^2(r) E^2 \\
&\quad + b_{Coul.}^0 n_e \left(1 + \log \left(\frac{E/m_e}{n_e} \right) / 75 \right) \\
&\quad + b_{Brem.}^0 n_e \left(\log \left(\frac{E/m_e}{n_e} \right) + 0.36 \right).
\end{aligned}
\tag{3.3}
$$

where the constants are in units of 10^{-16} GeV s^{-1} and have values $b_{syn}^0 \simeq 0.0254$, $b_{IC}^0 \simeq 0.76$, $b_{brem}^0 \simeq 1.51$, and $b_{Coul}^0 \simeq 6.13$ [209, 106]. Additionally, we take the photon energy densities to be $u_{SL} = 8$ eV cm^{-3} for starlight and $u_{CMB} = 0.25$ eV cm^{-3} for CMB photons [259, 257]. We will work under the assumption of a steady-state solution, and we thus set the left hand side to zero while noting that the analytic solution can be determined in the case on non-stationary sources [106, 162]; also, we adopt a homogeneous diffusion coefficient of the form,

$$
D(E) = D_0 E^\delta.
\tag{3.4}
$$

The similarity between the Andromeda galaxy and the Milky Way motivates us to adopt Galactic diffusion parameter values; we thus employ $D_0 = 3 \times 10^{28}$ cm^{2}s^{-1} and $\delta = 0.3$, which are representative values for the Milky Way [295, 317, 24, 322]. While previous analyses of DM annihilation in Andromeda neglect diffusion [135, 97], we take this into account for a more conservative analysis, noting in particular that diffusion is relevant on the smaller scales that we explore in this work. There are also other potential astrophysical processes that could depress the signal such as convection and reacceleration [295, 111], however we do not consider these effects in this analysis. The full analytic solution to the diffusion

equation with free-escape boundary conditions is [106, 162],

$$G(r, \Delta v) = \frac{1}{\sqrt{4\pi \Delta v}} \sum_{n=-\infty}^{\infty} (-1)^n \int_0^{r_h} dr' \frac{r'}{r_n} \left(\frac{\rho_\chi(r')}{\rho_\chi(r)} \right)^2$$
$$\times \left[\exp \left(-\frac{(r' - r_n)^2}{4\Delta v} \right) - \exp \left(-\frac{(r' + r_n)^2}{4\Delta v} \right) \right], \quad (3.5)$$

where r_h is the diffusion zone radius and the locations of the image charges used to implement the free-escape boundary condition are $r_n = (-1)^n + 2nr_h$. The value Δv is defined as $\Delta v = v(E) - v(E')$ with

$$v(E) = \int_E^{M_\chi} d\tilde{E} \frac{D(\tilde{E})}{b(\tilde{E})}. \quad (3.6)$$

where we have adopted the spatially independent form of the energy loss term as previously described [220].

3.2.2 Magnetic Field

The predicted synchrotron emission from the $e^\pm$ products of dark matter annihilation depends heavily on the magnetic field strength and profile. While the full three dimensional structure of the magnetic fields in the central region of M31 can be highly complex, the magnitude of the fields as determined by Faraday rotation measures of polarized radio emission have been reported to have strengths of $15 \pm 3\,\mu\mathrm{G}$ for $r = 0.2 - 0.4$ kpc and $19 \pm 3\,\mu\mathrm{G}$ for $r = 0.8 - 1$ kpc [160, 174], whereas the regular magnetic field in the outer regions is fairly constant with a typical strength of roughly $5 \pm 1\mu\mathrm{G}$ [147]. In this study we model the magnetic field of M31 with an exponential component as well as a constant component with the form,

$$B(r) = B_0 e^{-r/r_c} + B_{const}. \quad (3.7)$$

For consistency with above quoted values, we adopt $B_0 = 10\mu\mathrm{G}$ and $B_{const} = 5\mu\mathrm{G}$, as well as taking $r_c = 1.5$ kpc based on estimates of the magnetic field scale height [147]. Since we are only interested in a relatively small region of radius $r \sim 1-5$ kpc, we assume a spherical magnetic field model while acknowledging that a more accurate model of the magnetic field would include another spatial dependence perpendicular to the plane of the galaxy in order to better model the disk structure at larger radii.

3.2.3 Dark Matter Density Profile

Previous studies have shown that the M31 rotation curves can be fit with good results by using a Navarro-Frenck-White (NFW) [240, 241] profile [299, 282]. Here we adopt a generalized NFW profile of the form

$$\rho_\chi(r) = \frac{\rho_s}{\left(\frac{r}{r_s}\right)^\gamma \left[1 + \left(\frac{r}{r_s}\right)\right]^{3-\gamma}}, \tag{3.8}$$

where γ is a free parameter. For a standard NFW profile we take $\gamma = 1$, however when including significant baryonic matter, such as in the central regions of galaxies, the DM distribution is expected to have a more centrally peaked profile [54, 274]. Values used in GCE analysis are typically about $\gamma \sim 1.2 - 1.3$ [83, 116, 167, 175]. Thus, we will examine a variety of γ values, taking a default of $\gamma = 1.25$. The values for the characteristic density, ρ_s, and scale radius, r_s, are taken to be 0.418 GeV cm^{-3} and 16.5 kpc respectively [299].

3.2.4 Interstellar Radiation Field

In modeling the ISRF for Andromeda we include two elements: the CMB radiation field which is modeled exactly by a black-body spectrum with temperature

$T = 2.735$ K, as well as a starlight (SL) radiation component. We approximate the SL energy spectrum as a black-body with $T = 3500$ K, following previous work showing this is a reasonable assumption for the case of the Milky Way [102]. Unlike the CMB radiation field that is constant throughout the universe, our SL radiation field requires including a spatial dependence. For this, we use a two component bulge-disk model that follows the luminosity profile of M31 [110]. Specifically, for the bulge component we employ

$$n_b(r) \propto e^{-b_n \left[\left(\frac{r}{r_b} \right)^{1/n} - 1 \right]}, \tag{3.9}$$

and for the disk we employ instead

$$n_d(r) \propto e^{-\frac{r}{r_d}} \tag{3.10}$$

The values for the various parameter b_n, r_b, n, r_d are taken from Ref. [110]. From figure 9 of [110] we estimate the ratio of the bulge luminosity to the disk luminosity in the central regions of M31 to be $\sim 1/135$. Thus, the spatial profile of our SL model is given by,

$$n(r) \propto e^{-b_n \left[\left(\frac{r}{r_b} \right)^{1/n} - 1 \right]} + \frac{e^{-\frac{r}{r_d}}}{135}. \tag{3.11}$$

Including both the spatial and spectral components we have

$$n(\nu, r) = N \frac{8\pi\nu^2/c^3}{e^{h\nu/kT} - 1} \left[e^{-b_n \left[\left(\frac{r}{r_b} \right)^{1/n} - 1 \right]} + \frac{e^{-\frac{r}{r_d}}}{135} \right] \tag{3.12}$$

where N is a normalization factor. This factor is determined by assuming that the SL energy density in the central regions of M31 is similar to that of the MW,

which is roughly ~ 8 eV cm^{-3} [257, 259], giving us a value of $N = 4.9 \times 10^{-11}$. In table 3.1 we summarize our parameter selection. These are the values used throughout our analysis unless otherwise noted.

Astrophysical Parameters	
d	780 kpc
r_h	5 kpc
r_{ROI}	5 kpc
r_{core}	1.5 kpc
$B(r)$	$B_0 e^{-r/rc} + B_{const}$
$B(0)$	15 μG
ρ_s	0.418 GeV/cm^3
r_s	16.5 kpc
γ	1.25
$D(E)$	$D_0 E^\delta$
D_0	3×10^{28}cm^2 s^{-1}
δ	0.3

Table 3.1: Default astrophysical parameters. These values are used throughout unless otherwise noted.

3.3 Emission from Dark Matter Annihilation

3.3.1 Synchrotron

In addition to gamma-rays from prompt emission in the annihilation event, the injection of charged electrons and positrons from DM annihilation is expected to produce multi-wavelength emission through processes including synchrotron radiation, inverse Compton scattering of ambient photons, bremsstrahlung, and

Coulomb interactions. In the presence of magnetic fields stronger than the equivalent CMB energy density ($B_{CMB} = 3.25(1 + z)^2 \, \mu$G), synchrotron radiation is the dominant energy loss process of the electron/positron byproducts of DM annihilation. The synchrotron power for a frequency ν averaged over all directions is [293, 209]

$$P_{syn}(\nu, E, r) = \int_0^\pi d\theta \frac{\sin\theta}{2} 2\pi \sqrt{3} r_0 m_e c \nu_0 \sin\theta F\left(\frac{x}{\sin\theta}\right), \qquad (3.13)$$

where $r_0 = e^2/(m_e c^2)$ is the classical electron radius, θ is the pitch angle, and $\nu_0 = eB/(2\pi m_e c)$ is the non-relativistic gyrofrequency. The x and F terms are defined as,

$$x \equiv \frac{2\nu(1+z)m_e^2}{3\nu_0 E^2}, \qquad (3.14)$$

$$F(s) \equiv s \int_s^\infty d\zeta K_{5/3}(\zeta) \simeq 1.25 s^{1/3} e^{-s} \left[648 + s^2\right]^{1/12}, \qquad (3.15)$$

where $K_{5/3}$ is the Bessel function of order 5/3. The synchrotron emissivity is then

$$j_{syn}(\nu, r) = 2 \int_{m_e}^{M_\chi} dE \frac{dn_e}{dE}(E, r) P_{syn}(\nu, E, r). \qquad (3.16)$$

The integrated flux density spectrum can then be taken to be [220, 106]

$$S_{syn} \approx \frac{1}{D_A^2} \int dr r^2 j_{syn}(\nu, r), \qquad (3.17)$$

where D_A is the angular diameter distance.

3.3.2 Inverse Compton

In addition to synchrotron radiation, inverse Compton scattering of ambient CMB and starlight photons is a significant radiative loss process for > 1 GeV electrons and positrons. Depending on the mass of the DM particle [190], the up-scattered CMB photons will peak in the soft to hard X-rays, and the higher energy SL photons will upscatter into the hard X-ray up to soft gamma-ray regime, with higher DM masses leading to higher energy resulting spectra in each case. With the photon number density $n(\epsilon, r) = n_{CMB}(\epsilon) + n_{SL}(\epsilon, r)$, and the IC scattering cross-section $\sigma\left(E_\gamma, \epsilon, E\right)$, the IC power is

$$P_{IC}\left(E_\gamma, E, r\right) = cE_\gamma \int d\epsilon\, n\left(\epsilon, r\right) \sigma\left(E_\gamma, \epsilon, E\right) \tag{3.18}$$

where ϵ is the energy of the target photons, E is the energy of the relativistic electrons and positrons, and E_γ is the energy of the photons after scattering. The scattering cross-section, $\sigma\left(E_\gamma, \epsilon, E\right)$, is given by the Klein-Nishina formula:

$$\sigma\left(E_\gamma, \epsilon, E\right) = \frac{3\sigma_T}{4\epsilon\gamma^2} G\left(q, \Gamma\right), \tag{3.19}$$

where σ_T is the Thomson cross-section and $G(q, \Gamma)$ is given by [56]:

$$G(q, \Gamma) = \left[2q \ln q + (1 + 2q)(1 - q) + \frac{(2q)^2(1 - q)}{2(1 + \Gamma q)}\right], \tag{3.20}$$

where,

$$\Gamma = \frac{4\epsilon\gamma}{m_e c^2} = \frac{4\gamma^2 \epsilon}{E}, \qquad q = \frac{E_\gamma}{\Gamma(E - E_\gamma)} \tag{3.21}$$

The kinematics of inverse Compton scattering set the range of q to be $1/\left(4\gamma^2\right) \leq q \leq 1$ [106, 56, 273]. As with the synchrotron flux calculation, the local emissivity

is

$$j_{IC}\left(E_\gamma, r\right) = 2 \int_{m_e}^{M_\chi} dE \frac{dn_e}{dE}\left(E, r\right) P_{IC}\left(E, E_\gamma\right),$$ (3.22)

and the integrated flux density is:

$$S_{IC} \approx \frac{1}{D_A^2} \int dr r^2 j_{IC}(E_\gamma, r).$$ (3.23)

3.3.3 Gamma-rays

Calculating the gamma-ray flux from DM annihilation is straightforward in comparison to the synchrotron and IC fluxes since gamma-ray photons do not undergo the same radiative loss and diffusion processes. For the gamma-ray flux we integrate over the source volume [106, 264],

$$F_\gamma = \frac{1}{D_A^2} \int dr r^2 E^2 Q_\gamma\left(E, r\right).$$ (3.24)

3.4 Particle Physics Framework

In this analysis we seek to (i) test whether the hypothesis that the gamma-ray emission from M31 originates from dark matter annihilation is compatible with the same explanation to the Galactic center excess (GCE) and (ii) examine whether WIMP dark matter can explain the gamma-ray excess observed in M31 by the Fermi collaboration [10] compatibly with observations of M31 at other wavelengths. While task (ii) doesn't necessarily entail specific choices for the pair-annihilation final state of the dark matter, given the relatively meager spectral information on the gamma-ray emission from M31, it does provide us with a preferred range for the particle dark matter mass. In order to pursue task (i) and (ii) simultaneously, and for simplicity, we shall consider annihilation final states

that have been suggested as plausible candidates to describe the GCE from the standpoint of the reconstructed GCE spectrum.

Specifically, following the results of previous studies of the GCE we focus on particle models with $M_\chi = 40$ GeV and a dominant ($BR_{b\bar{b}} = 100\%$) annihilation branching ratio to $b\bar{b}$ [3, 83, 116], a mass of $M_\chi = 10$ GeV with final state $\tau^\pm$ [3, 175], as well as a mixed annihilation final state with $BR_{b\bar{b}} = BR_{\tau^\pm} = 0.5$ and $M_\chi = 40$ GeV [167] (hereafter referred to as the $b\bar{b}/\tau^+\tau^-$ final state). In passing we note that (a) in the context of Majorana particle dark matter models, for example the lightest neutralino of supersymmetry, such final states are often dominant in that mass range, and (b) the spectral features of the $b\bar{b}$ is largely representative of any dark matter annihilation spectrum to strongly interacting particles (gluon or lighter quark-antiquark pairs) in the mass range under consideration.

In addition, below we also fit to the M31 data with both the mass and cross-section as free parameters, to establish the preferred mass and annihilation rate combinations that best fit the M31 emission, for the same three annihilation final states listed above. While the cross-section allows us to normalize the predicted emission to the Fermi data, adjusting the mass allows us to shift the peak of the spectrum to better fit the data. In doing so, we explore the compatibility between the particle models that fit the M31 excess with models that fit the GCE.

3.5   Results

3.5.1   Compatibility with Galactic Center Excess Particle Models

For the initial comparison with GCE particle models we choose the DM particle mass and annihilation channel to be fixed and adjust the normalization. We

Free Parameters	Channel	M_χ (GeV)	$\langle\sigma v\rangle$ (10^{-26} cm^{3}s^{-1})			χ^2_{min}	p-value
			$\gamma = 1.00$	$\gamma = 1.25$	$\gamma = 1.50$		
$\langle\sigma v\rangle$	$b\bar{b}$	40	33.19	7.35	0.56	25.35	2.9×10^{-4}
	$\tau^+\tau^-$	40	39.17	8.69	0.66	62.72	$< 10^{-5}$
	$b\bar{b}/\tau^+\tau^-$	40	47.86	10.64	0.81	31.48	2.1×10^{-5}
	$b\bar{b}$	10	10.84	2.41	0.18	6.06	0.42
	$\tau^+\tau^-$	10	9.83	2.18	0.17	44.24	$< 10^{-5}$
	$b\bar{b}/\tau^+\tau^-$	10	14.7	3.04	0.23	10.01	0.12
$M_\chi, \langle\sigma v\rangle$	$b\bar{b}$	11.00	11.71	2.60	0.20	5.87	0.32
	$b\bar{b}/\tau^+\tau^-$	5.80	0.91	2.03	0.15	6.03	0.30

Table 3.2: Parameters and results of the fitting procedure, including by column order the free parameters of each fit, the annihilation channel assumed, the DM particle mass, the cross-section for each γ value, and the corresponding χ^2_{min} and p-values.
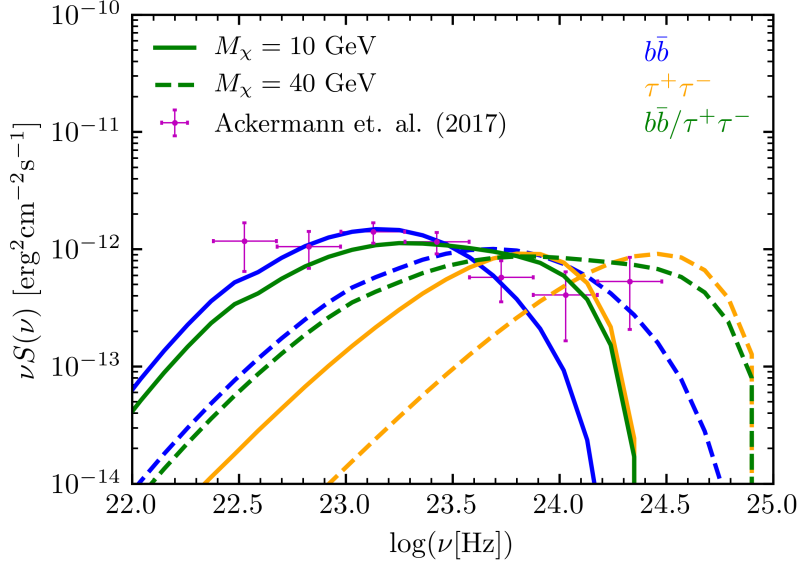
Figure 3.1: Gamma-ray SED using best-fit cross-sections. with fixed mass values of $M_\chi = 10$ GeV (solid) and $M_\chi = 40$ GeV (dashed) for three final states, $b\bar{b}$ (blue), $\tau^+\tau^-$ (orange), and $b\bar{b}/\tau^+\tau^-$ (green).

consider particle models with masses of 10 and 40 GeV, annihilation final states $b\bar{b}$, $\tau^+\tau^-$, and $b\bar{b}/\tau^+\tau^-$, and cross-sections in the range $\sim 10^{-30} - 10^{-20}$ cm^{3}s^{-1}. Cross-sections were determined by minimizing χ^2, and the results are reported in table 3.2 along with the corresponding χ^2_{min} and p-values. The normalized gamma-ray spectra in an ROI of 5 kpc, corresponding to the region where the observed excess is concentrated, for each particle mass and annihilation state are shown in figure 3.1 along with the Fermi M31 data [10]. The best fitting particle model for the masses considered is given by the $b\bar{b}$ model at 10 GeV, followed by the mixed $b\bar{b}/\tau^+\tau^-$ final state at 10 GeV. The pure $\tau^+\tau^-$ annihilation channel at 10 GeV and 40 GeV as well as the $b\bar{b}$ and $b\bar{b}/\tau^+\tau^-$ 40 GeV particle models have harder spectra that do not fit the Fermi M31 data well.

The spectra in figure 3.1 assume a NFW parameter of $\gamma = 1.25$ in accordance with the discussion in section 3.2.3. However, the actual steepness of the inner profile (i.e. γ) is uncertain, so we show in figure 3.2 the best-fitting cross-section of

the dark matter particle masses and final states under consideration for a variety of γ values. The resulting particle models are compared with Fermi gamma-ray constraints from observations of dSphs [9].
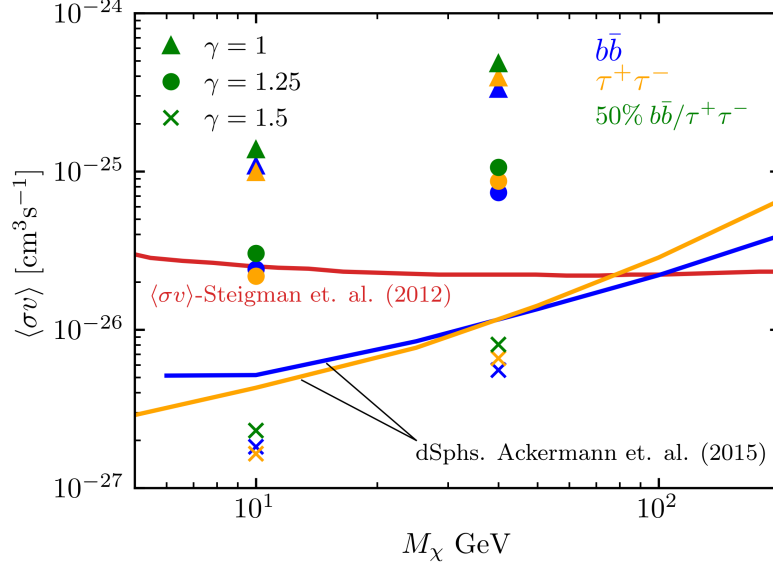
Figure 3.2: The normalized cross-sections are shown for each mass considered in comparison to the Fermi dSphs constraints for multiple γ values and annihilation channels.

For all masses and annihilation channels, the shallowest DM profile ($\gamma = 1$) conflicts with the Fermi dSphs results, requiring cross-sections well above the reported constraints. At $\gamma = 1.25$, the required cross-sections for the 40 GeV particles are still almost an order of magnitude higher than the maximal annihilation cross-sections allowed by Fermi dSph constraints. For the 10 GeV models at $\gamma = 1.25$, all of the cross-sections are concentrated at $\sim 2 - 3 \times 10^{-26}$ cm^{3}s^{-1}, or right around the thermal relic cross-section [290]. In the case of the $\tau^+\tau^-$ annihilation channel, this is in good agreement with best-fit results of GCE analysis, although conflicts in the case of $b\bar{b}$ final states, since higher masses (~ 40 GeV) are favored for $b\bar{b}$ in GCE particle models. As we steepen the profile to $\gamma = 1.5$,

we find that the necessary cross-sections fall below the dwarf constraints, and roughly a factor of 10 and a factor of five below the thermal-relic cross-section for the 10 GeV and 40 GeV masses respectively. Of course, a sub-thermal annihilation rate is perfectly fine from a cosmological standpoint, given for instance non-thermal production of dark matter from the decay of a heavier species in the early universe.

3.5.2 Fitting the Mass and Cross-section to the Andromeda Gamma-ray Data

Expanding on the analysis in the previous section we now allow both the mass of the dark matter as well as the cross-section to vary in order to fit the gamma-ray data and compare with GCE models. We consider masses in the range of $\sim 5 - 500$ GeV and cross-sections on the orders $\sim 10^{-30} - 10^{-20}$ cm^{3}s^{-1} and find our best fitting value in the case of $b\bar{b}$ final states with a mass of ~ 10 GeV as our best-fit to the Fermi M31 data. To illustrate this point quantitatively, we show the results of the fits in table 3.2 and show in figure 3.3 the 68% and 95% confidence levels for the $b\bar{b}$ and $b\bar{b}/\tau^+\tau^-$ final states. For a pure $\tau^+\tau^-$ final state we were unable to find a reasonable best-fit in the mass ranges considered without reaching the mass threshold for $\tau^+\tau^-$ at ~ 1.78 GeV.

In contrast to the previous GCE studies that found good fits for $b\bar{b}$ at ~ 40 GeV, we find that for all models considered a lower mass is required to fit the Fermi M31 observations. Specifically, with $\gamma = 1.25$, our best fitting model is the $b\bar{b}$ final state with $M_\chi = 11$ GeV and $\langle \sigma v \rangle = 2.60 \times 10^{-26}$ cm^3 s^{-1}, as well as the $b\bar{b}/\tau^+\tau^-$ final state with $M_\chi = 5.8$ GeV and $\langle \sigma v \rangle = 2.03 \times 10^{-26}$ cm^3 s^{-1}. In figure 3.4, we show the SEDs of these models in comparison to the spectra of the GCE particle models as discussed in sections 3.4 and 4.3.3, and with $\gamma = 1.25$ as
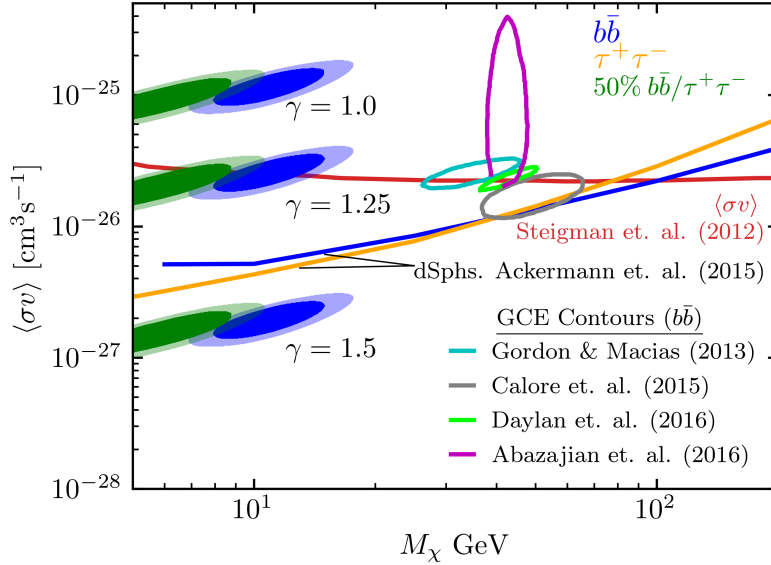
Figure 3.3: We show the 68% and 95% confidence contours of our best fit models with both M_χ and $\langle\sigma v\rangle$ as free parameters. For comparison we also show Fermi dSphs cross-section constraints, along with 95% confidence contours for $b\bar{b}$ final states in GCE studies.

in figure 3.1.

3.5.3 Comparison to Radio Data

The annihilation of WIMP dark matter particles is expected to produce not only gamma-rays through neutral pion decay, but also an abundance of charged electron/positron pairs, which in turn are expected to produce radio emissions through synchrotron radiation. Thus, any DM particle model that is purported to explain the gamma-ray excess in M31 should also be compatible with radio observations under reasonable assumptions for magnetic field and diffusion models. The focus of radio studies in the literature has largely been on studying emissions in larger regions of M31 out to radii of ~ 16 kpc [38, 161, 30, 29, 31], or in the very central ~ 1 kpc region [320, 42]. To account for this we use the particle models
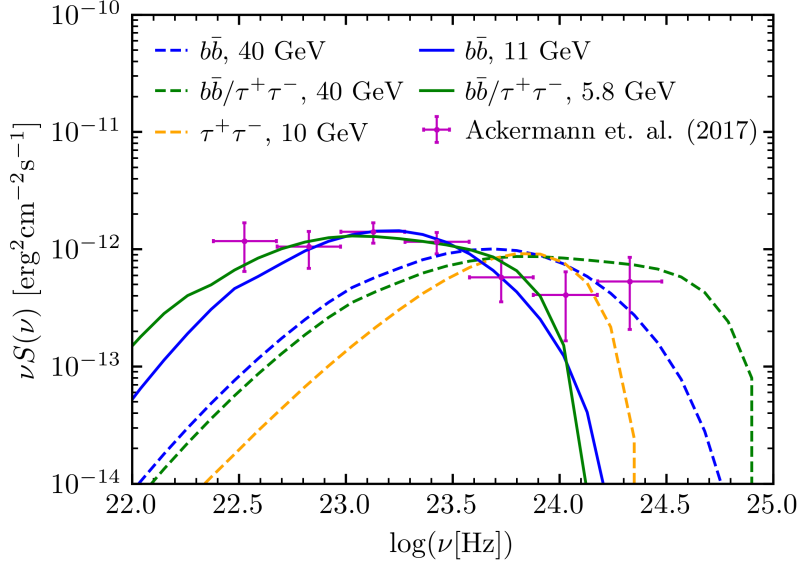
Figure 3.4: Gamma-ray SED for the three GCE models (dashed lines) where we choose fixed masses and annihilation final states consistent with GCE models and subsequently adjust the normalizing cross-section. We additionally show the results of our best-fit models from section 3.5.2 with both the mass and cross-sections as free parameters (solid lines).

consistent with the Fermi emission in a 5 kpc radius, then predict the radio emissions in a 1 kpc radius in order to compare with observational radio data. When extrapolating from 5 kpc to 1 kpc we assume an inner DM density profile with $\gamma = 1.25$. Additionally, we adopt diffusion and magnetic field models as described in sections 3.2.1 and 3.2.2 respectively of $D(E) = D_0 E^\delta$ with $D_0 = 3 \times 10^{28}$ cm^2 s^{-1} and $\delta = 0.3$ and $B(r) = B_0 e^{-r/r_c} + B_{const}$ with $B_0 = 10\,\mu$G and $B_{const} = 5\,\mu$G (see also table 3.1). Figure 3.5 shows the multi-wavelength SED within 1 kpc for our best-fit models as determined in the previous section compared to radio data. We also include the Fermi gamma-ray data and the predicted gamma-ray emission at 5 kpc (dashed lines) for reference and to emphasize that the particle cross-section is determined by fitting to the gamma-ray data (see previous section). We note that in the mixed state scenario radio emission is predicted to be

much larger than radio data in the 1 kpc region, suggesting tension with the assumption that a DM particle with this mass and annihilation state is responsible for the detected gamma-ray emissions. The $b\bar{b}$ final state model also conflicts with current observations, and predicts higher emission than observed for most data available, albeit with lower expected emissions than the mixed state model.
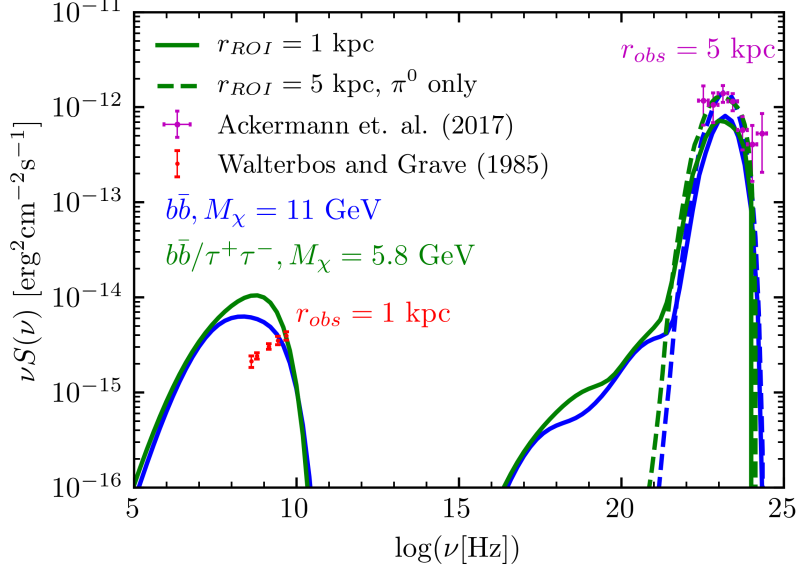
Figure 3.5: Multi-wavelength SED of our two best-fit models within a 1 kpc ROI compared to radio data [320]. Also shown is the Fermi data [10] and our predicted gamma-ray emission (dashed) within a 5 kpc region.

We also take into consideration uncertainty in the magnetic field and the efficiency of diffusion as parameterized by the size of the diffusion coefficient. Previous studies of radio emissions due to DM annihilation in M31 have typically ignored diffusion, however in figure 3.6 we demonstrate the effect that varying the diffusion strength (over a range of low to high estimates for the Milky Way) has on the expected emissions. Additionally, in figure 3.7 we show the DM emission including the magnetic field uncertainty as discussed in section 3.2.2. Figures 3.6 and 3.7 emphasize the role that the uncertainties in the astrophysics of diffusion and magnetic field parameters have on our ability to make concrete statements

66

concerning the validity of the DM explanation of the gamma-ray excess in M31. For instance, from figure 3.7 we see that even in the case of the lowest magnetic fields considered, the DM interpretation appears to conflict with the available data. To make dark matter compatible with the radio observations would require a magnetic field strength lower than our most conservative estimates. Diffusion however presents a much more impactful source of uncertainty, as demonstrated in figure 3.6. While our nominal value for the diffusion constant is the most typical assumed value for the Milky Way, if we adopt a value that is at the upper limit of quoted values we see a significant decrease in the radio emission. Conversely, for decreasing the diffusion constant yields expected emission that greatly overproduces the observational data. Nevertheless, we have demonstrated that conservative estimates for these parameters predict radio emissions from DM annihilation that are in tension with current observations.

Some other points to note include that the spectral shape of the radio emission cannot be matched by the models that fit the gamma-ray data. Due to the low masses needed to fit the gamma-rays, the synchrotron emission peaks at frequencies that are too low for the spectral shape of the predicted emission to match the observations. Additionally, in this analysis we have assumed that the radio emission observed is due entirely to dark matter annihilation. This gives a more conservative approach, since there are other astrophysical contributions to the radio emission such as synchrotron-emitting cosmic-rays that have not been taken into account.

3.6 Conclusion

In this work we have examined the gamma-ray excess in M31 reported by the Fermi collaboration in the context of the multi-wavelength emissions from WIMP
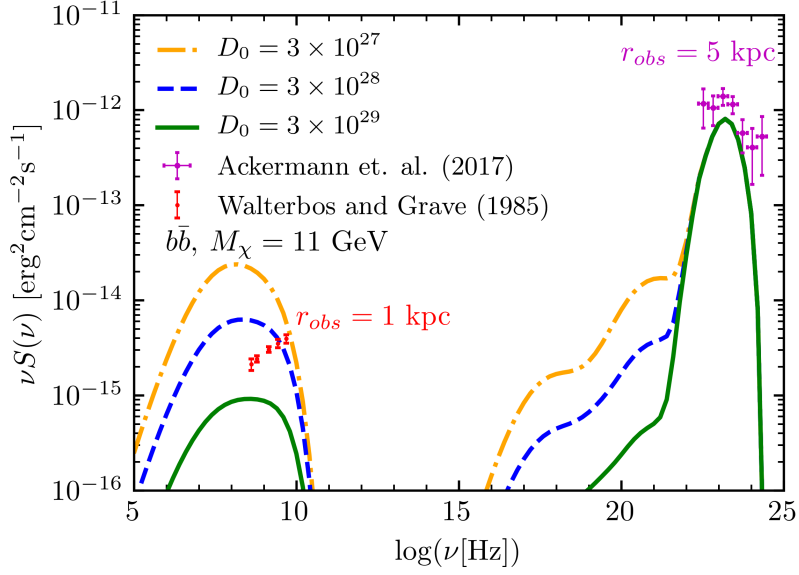
Figure 3.6: SED for the $b\bar{b}$ annihilation channel, $M_\chi = 11$ GeV, and $\langle \sigma v \rangle = 2.6 \times 10^{-26}$ cm^{3}s^{-1} with multiple diffusion constant values in units of cm^{2}s^{-1}
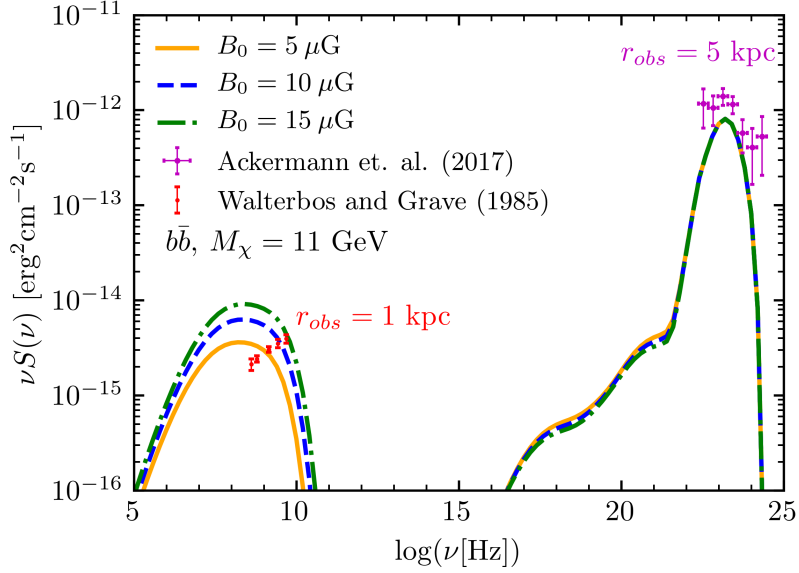
Figure 3.7: SED for the $b\bar{b}$ annihilation channel, $M_\chi = 11$ GeV, and $\langle \sigma v \rangle = 2.6 \times 10^{-26}$ cm^{3}s^{-1} with multiple magnetic field strengths.

dark matter annihilation. We used the RX-DMFIT tool [220] to predict the gamma-ray spectra from DM annihilation in M31 and to fit the expected gamma-

ray signal to the Fermi data in order to develop best-fit particle models. We did this in two ways; first, we adopted the final states and DM mass values that are consistent with the GCE, and fit the cross-section to the M31 data. This allowed us to compare the necessary cross-sections assuming GCE particle models with current constraints on the DM particle. We found that particle models typically associated with the GCE do not produce spectra that provide good fits to the M31 data.

We then allowed both the cross-section and mass to be free parameters in our fit. Our best fit models in this approach were for $b\bar{b}$ final states with a mass of $M_\chi = 11$ GeV and $\langle\sigma v\rangle = 2.6 \times 10^{-26}$ cm^{3}s^{-1}, consistent with other previous studies of gamma-rays in M31 [203], as well as finding a reasonable fit for $b\bar{b}/\tau^+\tau^-$ final states with a mass of $M_\chi = 5.8$ GeV and $\langle\sigma v\rangle = 2.03 \times 10^{-26}$ cm^{3}s^{-1}. Our analysis does not find a good fit for $\tau^+\tau^-$, although previous studies have also begun to disfavor this annihilation channel for typical GCE mass of $7 - 10$ GeV (see e.g. Ref. [116, 167]). We noted that the M31 data tends to favor lower particle masses than the GCE data for all annihilation channels.

Finally, after establishing the class of particle dark matter models consistent with the observed gamma-ray emission, we used RX-DMFIT to calculate the expected emission due to synchrotron radiation and inverse Compton scattering of CMB and starlight photons. We compared the expected radio emission in the central regions of M31 to observational data adopting a DM particle model with $b\bar{b}$ final states with a mass of $M_\chi = 11$ GeV and $\langle\sigma v\rangle = 2.6 \times 10^{-26}$ cm^{3}s^{-1} in accordance with our best-fit to the gamma-ray data. In this scenario we found that the expected emissions tend to overproduce in the observed radio emission for conservative estimates of the magnetic field ($B_0 = 10\mu$G) and diffusion constant ($D_0 = 3 \times 10^{28}$ cm^2 s^{-1}). However, our study shows that very efficient diffusion in

M31, to levels around one of order of magnitude larger than in the Milky Way, or highly suppressed average magnetic fields, could reconcile the relatively dim radio emission observed from the innermost 1 kpc of M31 with the expected bright radio emission from secondary electrons and positrons produced by dark matter annihilation.

Chapter 4

Exploring A Cosmic-Ray Origin of the Multi-wavelength Emission in M31

Note: The work in this chapter is adapted from "Exploring a cosmic-ray origin of the multiwavelength emission in M31." by A. McDaniel, T. Jeltema, S. Profumo, Phys. Rev. D, 100(2):023014, July 2019.

4.1 Introduction

The study of gamma rays in galactic environments offers an intriguing probe of many physical phenomena including cosmic-ray production and transport, star formation rates, or new physics such as dark matter. The Andromeda galaxy (M31) is particularly enticing as a target of gamma-ray studies due its status as the nearest large spiral galaxy. M31 has been the focus of several previous gamma-ray searches [146, 256, 288, 53, 4, 10, 196, 143]. Early observations [146, 256, 288, 53] were only able to place upper limits until the galaxy was first detected

in gamma-rays using 2 years of Fermi-LAT data at 5.3σ significance, along with some evidence of a spatial extension at the 1.8σ confidence level [4]. It has also been observed by high energy Cherenkov telescopes, though no detection has yet been made at energies above the TeV [18, 49, 14, 271].

More recently, M31 was detected in gamma-rays by the Fermi telescope at a significance of nearly 10σ with a detection of spatially extended emission out to ~ 5 kpc at the 4σ significance level [10]. This emission resembles to some extent the well studied Galactic Center Excess (GCE) of gamma rays in the center of the Milky Way, and has led to comparisons in possible origins for the emission in the two galaxies. Proposed explanations for the GCE include signals of annihilating dark matter [2, 83, 116, 167, 175, 166], an unresolved population of millisecond pulsars (MSP) [26, 64, 133], or additional cosmic-ray sources [91, 154, 100]. Due to some similarities between both the two galaxies themselves and the observed emissions, it is natural to also consider whether these are viable explanations for the M31 detection. Although there is significant uncertainty in the dark matter density profile, the possibility of a dark matter signal in M31 has previously been studied for gamma-rays [150, 18, 204], as well as other wavelengths [219, 135, 28, 97, 246, 61, 321]. A brief argument is presented in the recent Fermi detection paper [10] using the relative J-factors of the Galactic center and M31 to infer that the expected gamma-ray emission from dark matter annihilation in M31 is roughly a factor of ~ 5 below the observed emission. In a recent paper [219], we studied the possibility of a dark matter origin of the M31 emission from a multi-wavelength perspective. We found that when assuming a dark matter only interpretation using favored GCE dark matter models, such models typically require annihilation cross-sections above current constraints, and have spectral shapes that are inconsistent with the M31 observations. However, this

does not necessarily preclude these models contributing a subdominant component of the observed emission, with the shape of the spectrum predominantly determined by another emission source. Additionally,the dark matter particle models in that analysis that can reproduce the M31 gamma-ray emission also produce synchrotron emission that is in tension with observational radio data. There have also been efforts made to explore a millisecond pulsar (MSP) explanation for the M31 gamma-ray emission [133, 151]. Ref. [151] studied MSPs originating from globular cluster disruption in the bulge of M31, whereas Ref. [133] considered MSPs formed *in situ.* The *in situ* model was found to fit the energetics and morphology of the excess well, however neither study could account for the full detected emission, with each providing only $\sim 1/4$ of the M31 observation.

In light of the lack of a definitive dark matter or exclusive unresolved MSP explanation, this work focuses on the scenario in which this emission can potentially be accounted for using a conventional astrophysical interpretation of cosmic ray induced emissions. In order to explore this possibility, we study the multi-wavelength emission in Andromeda to consider whether a cosmic ray explanation is consistent across the spectrum. We predominantly focus on the radio and gamma-ray emission, as these regimes provide the most insight given currently available observational data. The production of cosmic rays in astrophysical systems can lead to emissions at various wavelengths from radio, to X-ray and gamma-ray [56, 209, 273]. When cosmic ray electrons (CRe) are injected into regions containing magnetic fields, they radiate synchrotron emission at radio wavelengths, whereas through inverse Compton scattering the electrons upscatter ambient photons, such as from the CMB or starlight, to X-ray and gamma-ray energies. Gamma rays can also be produced directly through the decay of neutral pions produced in cosmic-ray proton (CRp) collisions with the interstellar medium

[121, 213]. We note that – as discussed in Ackermann et. al. (2017) [10] – the gamma-ray emission does not seem to be spatially correlated with neutral gas or regions of high star formation, which are typically the regions wherein CRp are expected to be produced and interact with the ISM to produce the π^0 gamma-rays. The magnitudes of these fluxes depend on the components of the astrophysical environment, such as magnetic field, target photon radiation field, and abundance of cosmic ray production mechanisms. The diffusion of the relativistic cosmic rays additionally plays a significant role in the expected signal, as cosmic rays diffuse and escape the system, thus suppressing the expected flux. The mechanism by which cosmic rays are produced and accelerated has been a topic of extensive interest. For galaxies, supernovae remnants (SNR) are considered to be the main sources of cosmic rays [162, 35, 34, 305, 130]. While SNRs are thought to provide the dominant contribution of cosmic rays in galaxies, other mechanisms such as pulsars and their nebula can also provide significant contributions to the total cosmic ray population [13, 158, 176]. The expected power injection from these cosmic ray sources provides a benchmark to which we can compare the cosmic ray power necessary to produce the multi-wavelength emissions in M31.

This chapter is organized as follows: in section 4.2 we detail the relevant physical modeling, including the magnetic field, interstellar radiation field, and diffusion model, as well as the solution to the diffusion equation. In section 4.3 we present the expressions for each radiative process under consideration, then in section 4.4 we present the data used in the analysis. In section 5.5 we present the results of our analysis, in section 4.6 we comment on X-ray diffuse emission constraints, and, finally, we conclude in section 5.6.

4.2 Astrophysical Model of Andromeda

In order to calculate the secondary emission from the production of primary or secondary cosmic-ray electrons, we must first model the relevant astrophysical components of Andromeda. In particular, we require a description of the magnetic field model, which determines the synchrotron emission produced, as well as the inter-stellar radiation field (ISRF) that provides the target photon bath for the inverse Compton (IC) scattering. Also relevant to this analysis is a model of diffusion and radiative energy losses, since the relativistic electrons diffuse out and escape the system, while also losing energy through synchrotron emission, IC emission, Coulomb interactions, and bremsstrahlung. In the following section, we briefly describe the model adopted in this work.

4.2.1 Magnetic Field

The study of radio synchrotron emission in M31 requires some knowledge of the magnetic field in our region of interest, namely within the inner few kpc. In this region, the field structure is turbulent and complex, however estimates of the field strengths as determined by Faraday rotation measures of polarized radio emission are typically around $15 \pm 3\mu$G for $r = 0.2 - 0.4$ kpc, and $19 \pm 3\mu$G for $r = 0.8 - 1.0$ kpc [174, 160]. At larger radii in the disk of the galaxy, the magnetic field falls off to values of roughly $5 \pm 1\mu$G [147]. In our previous study of Andromeda where we considered a dark matter origin of the multi-wavelength emission we selected a spatially dependent magnetic field based on these values, approximating some degree of spherical symmetry in the central region, while noting that that model would not be applicable at larger radii where a multi-dimensional field model would be more appropriate. In this analysis however, we treat the magnetic field strength as one of the free parameters in our fit, and so

we adopt a simplified constant magnetic field where

$$B(r) = B_\mu. \tag{4.1}$$

While this is helpful in that it reduces the parameters we need to fit in order to define our model, it comes at the cost of accuracy in capturing the complexity of the field or any spatial dependence. We can consider the constant field as an average over space, with a consequence of this being that we would expect the values of B_μ to be lower than the quoted central values, and at a roughly similar level to that of the disk.

4.2.2 Inter-stellar Radiation Field

Our inter-stellar radiation field model (ISRF) contains two components: (i) a CMB photon component and (ii) a starlight (SL) component. We have chosen to neglect the infrared (IR) component in the ISRF and instead focus only on the CMB and starlight components in order to simplify the ISRF modelling and fitting procedure, implicitly making the assumption that the starlight component will be the more significant contribution to the IC emission. For the CMB, we simply have a black-body spectrum at $T = 2.73$ K and spatial homogeneity. Thus we have,

$$n_{CMB}(\nu) = \frac{8\pi\nu^2}{c^3} \frac{1}{e^{h\nu/kT} - 1}. \tag{4.2}$$

For the starlight component, we approximate the spectrum as a black-body with temperature $T = 3500$ K, a choice motivated by previous analysis of the ISRF in the Milky Way demonstrating this as a good approximation for starlight spectra. We additionally include a spatial dependence based on the starlight luminosity

profile of M31 [110] incorporating a bulge component of the form:

$$n_{bulge}(r) \propto e^{-b_n\left[\left(\frac{r}{r_b}\right)^{1/n}-1\right]}. \tag{4.3}$$

and a disk component:

$$n_{disk}(r) \propto e^{-\frac{r}{r_d}}. \tag{4.4}$$

Combining these spatial components with the black-body spectral profile yields a starlight photon number density:

$$n_{SL}(\nu, r) = N_{SL}\frac{8\pi\nu^2/c^3}{e^{h\nu/kT}-1}\left[e^{-b_n\left[\left(\frac{r}{r_b}\right)^{1/n}-1\right]} + \frac{e^{-\frac{r}{r_d}}}{135}\right]. \tag{4.5}$$

The parameters r_b, r_d, n, b_n are taken from [110] and the factor of $1/135$ in the disk component was chosen to recreate the bulge to disk luminosity ratio in [110]. The factor N_{SL} is a dimensionless normalization constant that is to be determined in the later sections as a free parameter in our fit. To get a sense for what value this parameter should be, we can consider the stellar luminosity of the inner region of M31. The stellar luminosity within a 1 kpc radius of M31 has previously been reported as $L = 10^{9.9}L_{\odot}$ [170, 127]. We can roughly estimate the luminosity as

$$L = 4\pi r^2 c\,\bar{u}_{SL}, \tag{4.6}$$

where the bar refers to a spatial average over the volume. Taking the radius to be ~ 1 kpc, a stellar luminosity of $L = 10^{9.9}L_{\odot}$ corresponds to $\bar{u}_{SL} \approx 5$ eV cm^{-3}, or $N_{SL} \approx 5 \times 10^{-12}$. A reasonable, albeit somewhat large, range of values for the stellar energy density in the inner regions of galaxies is $\bar{u}_{SL} \approx 1 - 10$ eV cm^{-3} [259, 257], which roughly corresponds to a normalization fit range of

$N_{SL} \in (10^{-12}, 10^{-11})$.

4.2.3 Solution to the Diffusion Equation

After being injected into the system, the CRe undergo both radiative losses and diffusion. Diffusion is particularly important on shorter distance scales, such as the few kpc scales considered in this work, and we have demonstrated in our previous M31 paper (see Fig. 6 from [219]) that it significantly impacts the expected fluxes. The diffusion and radiative energy loss mechanisms of the CRe are accounted for in the diffusion equation:

$$\frac{\partial}{\partial t}\frac{dn_{e^{\pm}}}{dE} = \boldsymbol{\nabla}\left[D(E,\mathbf{r})\boldsymbol{\nabla}\frac{dn_{e^{\pm}}}{dE}\right] \\ + \frac{\partial}{\partial E}\left[b(E,\mathbf{r})\frac{dn_{e^{\pm}}}{dE}\right] + Q(E,\mathbf{r}). \tag{4.7}$$

where we neglect convection and reacceleration effects which can be safely ignored for energies greater than a few GeV [119, 118]. Particularly in a quiescent galaxy such as M31 with its low star-formation rate [149, 261], the effects of convection are expected to be less prominent than in galaxies with higher star-formation activity [218, 199, 315] such as starbursts or even the Milky Way, and thus we treat diffusion as the dominant escape term. In equation 4.7, $\partial n_e/\partial E$ is the electron/positron equilibrium spectrum with units of GeV^{-1} cm^{-3}, $D(E,\mathbf{r})$ is the diffusion coefficient, $b(E,\mathbf{r})$ is the energy loss term, and $Q(E,\mathbf{r})$ is the CRe source term that we specify in later sections and has units of GeV^{-1} s^{-1} cm^{-3}. In the energy loss term, we include contributions from synchrotron, IC, Coulomb, and

bremsstrahlung processes, with the full expression given by:

$$b(E, \mathbf{r}) = b_{IC}(E, \mathbf{r}) + b_{Synch.}(E, \mathbf{r}) + b_{Coul.}(E) + b_{Brem.}(E)$$

$$= b_{IC}^0 u_{CMB} E^2 + b_{IC}^0 u_{SL}(r) E^2 + b_{Synch.}^0 B^2(r) E^2$$

$$+ b_{Coul.}^0 \bar{n}_e \left(1 + \log \left(\frac{E/m_e}{\bar{n}_e} \right) / 75 \right) \tag{4.8}$$

$$+ b_{Brem.}^0 \bar{n}_e \left(\log \left(\frac{E/m_e}{\bar{n}_e} \right) + 0.36 \right).$$

The b^0 coefficients in this expression have units GeV s^{-1} with values $b_{syn}^0 \simeq 0.0254$, $b_{IC}^0 \simeq 0.76$, $b_{brem}^0 \simeq 1.51$, and $b_{Coul}^0 \simeq 6.13$ [209, 106]. The photon energy density for the CMB is $u_{CMB} = 0.25$ eV cm^{-3} and for the starlight photons can be computed from equation (4.5) to be $u_{SL}(r) = h\nu_0^2 n_{SL}(\nu_0, r)$, where ν_0 is taken to be the peak frequency. Finally, $\bar{n}_e$ in equation (4.8) refers to the average thermal electron density and is taken to be $\bar{n}_e \approx 0.01$ cm^{-3} [153, 40, 41, 87, 86].

For the diffusion coefficient we assume a homogeneous power law of the form:

$$D(E) = D_0 E^\delta \tag{4.9}$$

with $\delta = 1/3$ and $D_0 = 3 \times 10^{28}$ cm^2 s^{-1} [295, 317, 24, 322]. The choices of these parameters are motivated by assuming that M31 has roughly similar diffusion properties to the Milky Way, with these values being determined by measurements of the stable (e.g. B/C) or unstable (e.g. Be^{10}/Be^9) secondary to primary ratios, and also supported by studies of the far-infrared - radio correlation in M31 and other galaxies that infer similar values [39, 237]. Equation (4.7) can be solved analytically using the Green's function method (see e.g. [106, 162]) and in the steady state case where the left-hand side of equation (4.7) is set to zero the

appropriate Green's function with free-escape boundary conditions is given by:

$$G(r, \Delta v) = \frac{1}{\sqrt{4\pi\Delta v}} \sum_{n=-\infty}^{\infty} (-1)^n \int_0^{r_h} dr' \frac{r'}{r_n} \left(\frac{Q(E, r')}{Q(E, r)} \right)$$
$$\times \left[\exp\left(-\frac{(r' - r_n)^2}{4\Delta v} \right) - \exp\left(-\frac{(r' + r_n)^2}{4\Delta v} \right) \right],$$

(4.10)

where $r_h \approx 5$ kpc is the diffusion zone radius and the locations of the image charges used to implement the free-escape boundary condition are $r_n = (-1)^n r + 2nr_h$. The value Δv is defined as $\Delta v = v(E) - v(E')$ with

$$v(E) = \int_E^{\infty} d\tilde{E} \frac{D(\tilde{E})}{b(\tilde{E})}.$$

(4.11)

where we have approximated a spatially independent form of the energy loss term by taking a spatial average of $u_{SL}(r)$ and $B(r)$ in equation (4.8). In the above expression, E' represents the energy of the electron at the source, while E is the interaction energy. The quantity $\sqrt{\Delta v}$ has units of distance, and represents the diffusion length scale of the particles. The final form of the electron equilibrium spectrum is then given by,

$$\frac{dn_{e\pm}}{dE}(E, r) = \frac{1}{b(E, r)} \int_E^{\infty} dE' G(r, \Delta v) Q(E, r).$$

(4.12)

Here we use the full spatially dependent form of the energy loss expression, rather than the homogeneous form used in equation (4.11).

4.3 Multi-wavelength Emission

Once we have obtained the electron equilibrium spectrum $dn_{e\pm}/dE$ by solving the diffusion equation, we can then proceed to calculate the emissivity j_i, by

integrating the electron spectrum with the power for the given radiative process, namely the synchrotron radiation and IC scattering for our purposes. This gives

$$j_i(\nu, r) = 2 \int_{m_e}^{\infty} dE \, P_i(\nu, E, r) \frac{dn_{e^{\pm}}}{dE}(E, r) \qquad (4.13)$$

where the factor of two accounts for electrons and positrons and P_i is the power of a radiative process i which we calculate in the following sections. From here, the flux density is given by the integral of the emissivity over volume,

$$S_i(\nu) = \frac{1}{4\pi d^2} \int dV j_i(\nu, r) \approx \frac{1}{d^2} \int dr \, r^2 j_i(\nu, r) \qquad (4.14)$$

where d is the distance to M31, taken to be $d = 780$ kpc [289]. In this work, we make use of the publicly available RX-DMFIT tool [220] to solve the differential diffusion equation and then to perform the various secondary emission calculations. Models used in this analysis can be obtained from the authors.

4.3.1 Synchrotron Power

In the presence of ambient magnetic fields, the relativistic CRe undergo synchrotron radiation, producing radio emission. The synchrotron power for a frequency ν averaged over all directions is [293, 209]

$$P_{syn}(\nu, E, r) = \int_0^{\pi} d\theta \frac{\sin\theta}{2} 2\pi\sqrt{3} r_0 m_e c \nu_0 \sin\theta F\left(\frac{x}{\sin\theta}\right), \qquad (4.15)$$

where $r_0 = e^2/(m_e c^2)$ is the classical electron radius, θ is the pitch angle, and $\nu_0 = eB/(2\pi m_e c)$ is the non-relativistic gyrofrequency. The x and F terms are defined as,

$$x \equiv \frac{2\nu m_e^2}{3\nu_0 E^2}, \qquad (4.16)$$

$$F(s) \equiv s \int_s^\infty d\zeta K_{5/3}(\zeta) \simeq 1.25 s^{1/3} e^{-s} \left[648 + s^2\right]^{1/12},\tag{4.17}$$

where $K_{5/3}$ is the Bessel function of order $5/3$.

4.3.2 Inverse Compton Power

With the photon number density $n(\epsilon, r) = n_{CMB}(\epsilon) + n_{SL}(\epsilon, r)$, and the IC scattering cross-section $\sigma(E_\gamma, \epsilon, E)$, the IC power is

$$P_{IC}(E_\gamma, E, r) = c E_\gamma \int d\epsilon \, n(\epsilon, r) \sigma(E_\gamma, \epsilon, E)\tag{4.18}$$

where ϵ is the energy of the target photons, E is the energy of the relativistic electrons and positrons, and E_γ is the energy of the photons after scattering (note that $E_\gamma = h\nu$ for observing frequency ν in equation (4.13)). The scattering cross-section, $\sigma(E_\gamma, \epsilon, E)$, is given by the Klein-Nishina formula:

$$\sigma(E_\gamma, \epsilon, E) = \frac{3\sigma_T}{4\epsilon\gamma^2} G(q, \Gamma),\tag{4.19}$$

where σ_T is the Thomson cross-section and $G(q, \Gamma)$ is given by [56]:

$$G(q, \Gamma) = \left[2q \ln q + (1 + 2q)(1 - q) + \frac{(2q)^2 (1 - q)}{2(1 + \Gamma q)}\right],\tag{4.20}$$

where,
$$\Gamma = \frac{4\epsilon\gamma}{m_e c^2} = \frac{4\gamma^2 \epsilon}{E}, \qquad q = \frac{E_\gamma}{\Gamma(E - E_\gamma)}\tag{4.21}$$

The kinematics of inverse Compton scattering set the range of q to be $1/(4\gamma^2) \leq q \leq 1$ [106, 56, 273].

4.3.3 Gamma-ray Flux

In addition to gamma rays produced from IC scattering, we also consider gamma rays resulting from the decay of neutral pions produced in cosmic-ray proton collisions. When the pions are produced they decay rapidly within a time span of $\sim 10^{-16}$ s. The gamma rays do not experience diffusion or radiative loss effects, and thus we do not need to consider equation (4.7). Instead, for a π^0 gamma-ray source injection Q_γ (in units of GeV^{-1} cm^{-3} s^{-1}), the flux is simply given by integrating over the volume of the source [106, 264, 219]:

$$F_\gamma = \frac{1}{d^2} \int dr\, r^2 E^2 Q_\gamma\left(E, r\right). \tag{4.22}$$

4.4 Gamma-ray and Radio Data

The gamma-ray data points are taken from the analysis performed in Ackermann et. al. (2017) [10], where they used 88 months of PASS 8 Fermi data collected between August 4, 2008, and December 1, 2015. Reconstructed events within an energy range of 0.1-100 GeV were considered as well as reconstructed directions within a $14° \times 14°$ region centered at $(\alpha, \delta) = (10°.6847, 41°.2687)$. SOURCE class events were used excluding those with zenith angle greater than $90°$ or rocking angle greater than $52°$. The resulting detected emission found in this study was concentrated within the inner 5 kpc, motivating this as the choice of region of interest in our calculations of the gamma-ray emission resulting from IC scattering and pion decay.

Radio observations of M31 have predominantly focused on regions of large radii out to about ~ 16 kpc with a particular emphasis on the star-forming 10 kpc "ring" [38, 161, 30, 29, 31], or alternatively on the central regions within $r \sim 1$

kpc [320, 42]. For our purposes, the available data in the 1 kpc region are most useful, as they allows us to focus our analysis on the inner region and make better comparisons between the 1 kpc ROI for radio emission and the 5 kpc ROI for gamma-ray emission. In each of the spectral energy distributions in the following sections, the synchrotron emission is calculated with $r = 1$ kpc while the IC and gamma-ray emission are calculated with $r = 5$ kpc.

4.5 Results

In our analysis, the multi-wavelength emission in M31 is assumed to be due to the presence of cosmic-rays. We consider here two cosmic-rays production mechanisms: the first is primary production of CRe following a power law with exponential cut-off source injection, which then radiate synchrotron and IC emission. The second source of cosmic-rays we consider is primary production of cosmic-ray protons obeying a power law. The hadronic inelastic interactions of the CRp produce neutral pions that decay into gamma rays, as well as charged pions that decay into secondary CRe which then produce synchrotron and IC emission. Finally, we consider the scenario in which both of these sources provide comparable contributions to the overall cosmic-ray abundance in what we refer to as our "multi-component" model. We then examine to what extent each of these three scenarios can be responsible for the multi-wavelength emission in M31. Of the three cases mentioned, the multi-component model appears the most convincing, while the primary-only and secondary-only models do not easily reproduce the emission in M31 within the range of realistic parameter space.

4.5.1 Emission from primary cosmic ray electrons

We now define the source term of equation (4.7) by considering the case in which the cosmic-ray population is dominated by primary electron production obeying a power law with an exponential cutoff:

$$Q_{e^{\pm}}(E) = N_{CR_e} \left(\frac{E}{\text{GeV}}\right)^{-\alpha_e} e^{-E/E_{cut}}. \tag{4.23}$$

In this section, α_{CR}, N_{CR_e}, E_{cut} in equation (4.23) along with B_μ and N_{SL} are taken to be free parameters that we adjust to fit the observed radio and gamma-ray spectra. Previous studies of cosmic-ray origins can provide some guidance as to reasonable values for these parameters. For example, values of $\alpha_e \sim 2.0 - 2.3$ have been found to be consistent with production of cosmic rays in supernovae (SNe), as well as suggesting E_{cut} values on the order of a few TeV [118, 123, 212, 140, 122]. The normalization N_{CR_e} however is poorly constrained, and in section 4.5.1 we compare the fit values of N_{CR_e} with the corresponding SNe power output.

In table 4.1 we list the results for the best-fitting model and plot the SED in figure 4.1. Throughout this analysis we fit the parameters by minimizing the standard χ^2 metric using a Nelder-Mead simplex algorithm [244, 258] to two decimal tolerance and employ a penalty function to enforce the fit range constraints. Additionally, the expansion, contraction, and shrink parameters are determined using a dimension dependent implementation [157]. For the source term parameters α_e and E_{cut}, we see a general agreement with expectations as described above, albeit with a cutoff energy somewhat lower than the TeV level. The starlight component is also suppressedto the lower end of the allowed range, with a normalization factor $N_{SL} = 1.02 \times 10^{-12}$ which is a factor of ~ 5 lower than the value derived in section 4.2.2. We find a magnetic field value of $B_\mu = 1.7\mu G$ which is relatively small in

comparison to those discussed in section 4.2.1. While the actual structure of the field would involve higher central values with some spatially dependent fall-off, the average strength of the field over the space can be expected to take a smaller value. However, even with this in mind the magnetic field value is particularly low and likely not representative of the field strength within the inner regions of M31, especially the inner ~ 1 kpc where the synchrotron emission is calculated. Thus, we instead seek a configuration that allows for a higher magnetic field value.
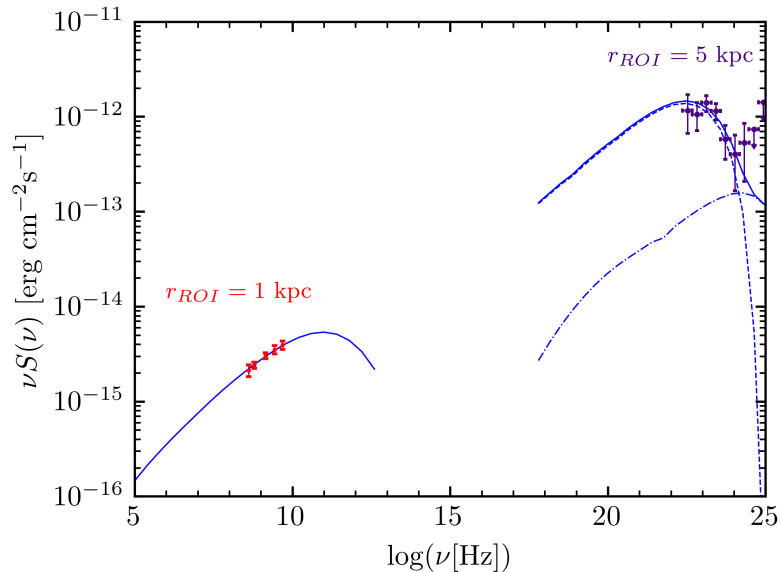
Figure 4.1: Synchrotron and IC emission from primary production of CRe for the best fit model in table 4.1. The dashed lines are the CMB IC contribution, the dash-dot are the SL IC contribution, and the total emissions are the solid lines. Radio data are taken from [320] and gamma-ray data are taken from [10]

One way in which we can potentially achieve a higher magnetic field is to take into consideration the case where the radio emission is due to synchrotron radiation from cosmic-ray electrons, but the IC emission is not sufficient to recreate the Fermi observations, and remain agnostic as to the source of the gamma-ray emission. To do this, we increase the strength of the magnetic field and change N_{CR_e} to reproduce the radio emission. In figure 4.2 we show these fluxes for a

α_e	E_{cut} (GeV)	N_{CR_e} (GeV^{-1}cm^{-3}s^{-1})	B_μ (μG)	N_{SL}	$\chi^2_{min}/d.o.f$
2.14	514	1.1×10^{-25}	1.7	1.02×10^{-12}	3.32/7
		Observational Values			
$2.0 - 2.3$	$10^3 - 10^4$	—	$5 - 10$	$10^{-12} - 10^{-11}$	—

Table 4.1: Free parameters and their values in our best-fit model for a power law with exponential cutoff primary electron source. For reference, we have included in the bottom row the experimental values for the parameters as described in the text. Reference values for the source normalization are discussed in the context of CR power output in section 4.5.1.

few values of the magnetic field, and list the normalization factors in table 4.2. In this approach, we are essentially assuming that for reasonable magnetic field values the radio synchrotron emission in M31 can be produced predominantly by primary cosmic-ray electrons, while the source of the gamma ray emission remains unaccounted for. In later sections we use this approach in conjunction with comic-ray secondaries to account for the full spectrum of emission.
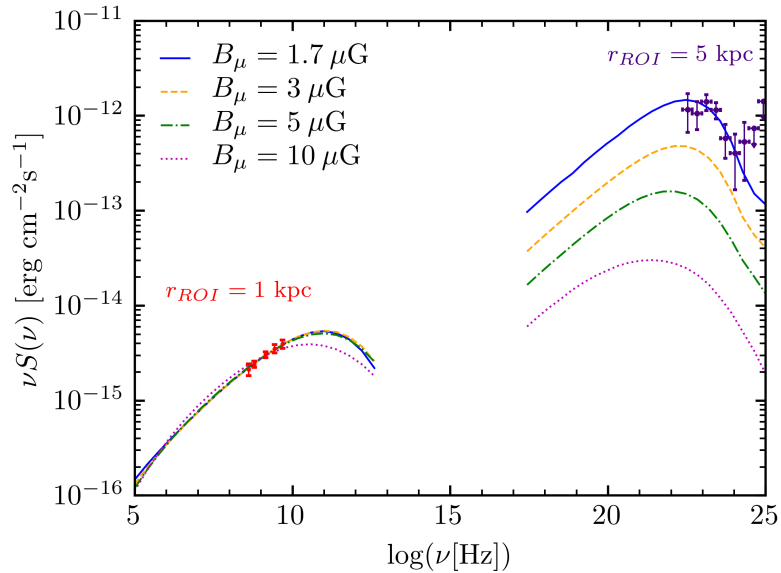
Figure 4.2: Spectrum due to synchrotron and IC emission from primary CRe for various values of the magnetic field, normalized to the observed radio emission. The best fit model is shown in green. Radio data are taken from [320] and gamma-ray data are taken from [10]

B_μ (μG)	N_{CR_e} (GeV^{-1}cm^{-3}s^{-1})
3	3.39×10^{-26}
5	1.28×10^{-26}
10	3.85×10^{-27}

Table 4.2: Normalization factors for various magnetic field strengths in the case of CRe primaries, normalized to the radio emission.

Cosmic-ray Electron Power

In order to place our value for the source term normalization N_{CR_e} into a physical context, we can compare the total power output injected into cosmic-ray electrons with physical processes such as supernovae explosions. The power injected into the CRe for the source term of equation (4.23) is given by,

$$P_{CR_e} = \int dV \int_{m_e}^{\infty} dE \, E \, Q_e(E), \qquad (4.24)$$

where V is the diffusion volume. Meanwhile, the power injected into cosmic-ray electrons from supernovae is given by the expression,

$$P_{SN,\,e} = \eta_e \Gamma E_{SN} \qquad (4.25)$$

where Γ is the supernova (SN) rate, E_{SN} is the total energy released in the SN explosion and η_e is the efficiency of the SN energy transferred to the CRe. The SNe rate can be estimated from the observed star-formation rate (SFR), which in the case of M31 has been measured to be $\sim 0.2 - 0.4$ M$_\odot$ yr^{-1} [149, 261]. Adopting a value of $SFR = 0.25$ M$_\odot$ yr^{-1} [149], the rate is then given by [178, 59]

$$\Gamma = SFR \times \frac{\int_{M_{min}}^{M_{max}} \psi(M) dM}{\int_{0.1 M_\odot}^{100 M_\odot} \psi(M) M dM}. \qquad (4.26)$$

We use the Salpeter initial mass function (IMF) [276] defined over the main-sequence mass range of $0.1 - 100 \, M_\odot$ wherein $\psi(M) \propto M^{-2.35}$ and $\psi(M)dM$ gives the number of stars in the mass range $M + dM$. We take $M_{min} = 8 M_\odot$ and $M_{max} = 40 M_\odot$ in line with canonical CC SNe parameters [178]. This yields a SNe rate of 0.17 per century, and the total energy output of for one supernova explosion is $E_{SN} \sim 10^{51}$ erg. While the efficiency at which energy is imparted to

electrons during SN explosions is not well constrained, several estimates suggest values of $\eta_e = 10^{-5} - 10^{-3}$ [300, 118]. Putting these together, we obtain a lower limit on the power injected into CRe in SNe explosions to be $P_{SN,e} \approx 5.1 \times 10^{35}$ erg s^{-1}, and an upper limit of $P_{SN,e} \approx 5.1 \times 10^{37}$ erg s^{-1}. In figure 4.3 we show the power injected into CRe implied by our best-fit model while increasing the magnetic field and normalizing to the radio data (as in figure 4.2). We compare this with the estimated range of SNe power output for CRe and see that the necessary normalization to fit the radio data produces a power requirement that is substantially greater than the estimated SNe power budget for the lower magnetic fields, including at the best-fit value when also fitting the gamma-ray data at $B_\mu = 1.7\mu$G. Although the SNe power calculations involve a great deal of uncertainty, it is unlikely that the uncertainty is so great that it can be reconciled with the power output implied by our parameter model. Potential other cosmic-ray acceleration mechanisms such as PWNe could also contribute to the power total, however we can briefly demonstrate that this contribution is not enough to overcome the difference. For the case of pulsars, the relevant quantity is the spin down luminosity which can be expressed as

$$P_{PWN} = \frac{\eta W_0}{t_0 \left[1 + \left(\frac{t_p}{t_0}\right)\right]^2} \tag{4.27}$$

where η is the injection efficiency, W_0 is the pulsar energy output, t_0 is the typical pulsar decay timescale and t_p is the pulsar lifetime [118, 211, 120, 206]. If we take as fiducial values, $\eta = 0.1$, $W_0 = 10^{50}$ erg, $t_0 = 1$ kyr and assume $t_p \approx t_0$ we obtain a power contribution from pulsars of

$$P_{PWN} = \frac{\eta W_0}{4 t_0} \approx 8 \times 10^{37} \text{erg s}^{-1}. \tag{4.28}$$

While this value suggests that PWNe can contribute a significant amount of the CRe power, the estimate here is not sufficient to account for the necessary CRe power of our best-fit models, and thus does not have a significant impact on the results shown in figure 4.3.
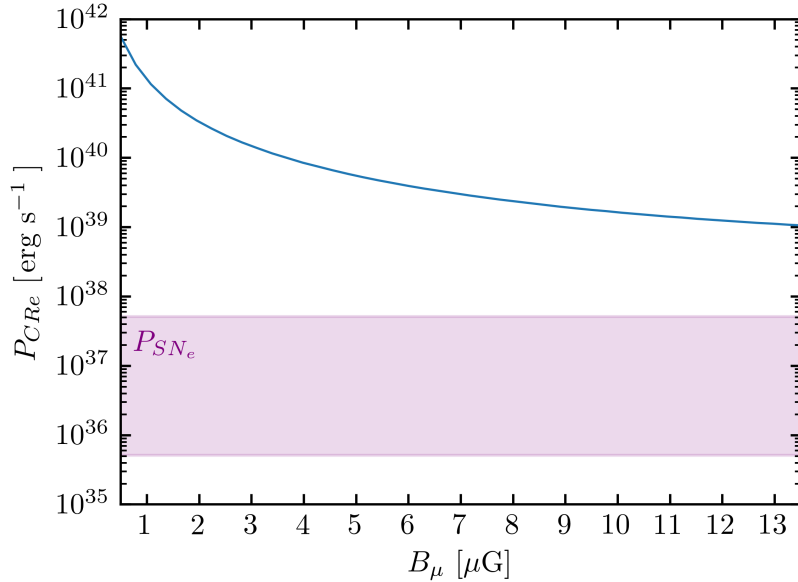
Figure 4.3: Power injection into CR_e according to equation (4.24) for increasing magnetic field strength, normalized to the radio data. The purple region shows the range estimate for the electron power injection due to SNe as calculated using Eq. (4.25).

4.5.2   Emissions from cosmic rays of hadronic origin

We next consider the scenario in which the dominant contribution to the cosmic-ray population is in the form of primary cosmic-ray protons. Inelastic interactions between the CRp and the interstellar medium produce neutral and charged pions. The neutral pions decay into gamma-rays, while the charged pions decay into muons and neutrinos, which in turn decay into neutrinos and secondary

CRe. This can be summarized as:

$$\pi^0 \to 2\gamma$$

$$\pi^\pm \to \mu^\pm + \nu_\mu/\bar{\nu}_\mu \to e^\pm + \nu_e/\bar{\nu}_e \tag{4.29}$$

For the most common astrophysical model of the CRp distribution we assume a simple power law:

$$n_{CR_p}(E) = N_{CR_p} \left(\frac{E}{\text{GeV}} \right)^{-\alpha_p} \tag{4.30}$$

with N_{CR_p} in units of GeV^{-1} cm^{-3}. The resulting source terms for the gamma rays and cosmic-ray electrons have been previously calculated for this choice of CRp source distribution [255, 213, 278]. Following [255] for the gamma-ray source term from π^0 decay yields the expression:

$$Q_\gamma(E,r) = N_{CR_p} \, n_N(r) c\sigma_{pp} \frac{4\xi^{2-\alpha_\gamma}}{3\alpha_\gamma} \left(\frac{m_{\pi^0}}{\text{GeV}} \right)^{-\alpha_\gamma}$$

$$\times \left[\left(\frac{2E_\gamma}{m_{\pi^0}} \right)^\delta + \left(\frac{2E_\gamma}{m_{\pi^0}} \right)^{-\delta} \right]^{-\alpha_\gamma/\delta} \tag{4.31}$$

with, $\alpha_\gamma = 4/3 \left(\alpha_p - 0.5 \right)$, and the source for $e^\pm$ from the charged pion decay is given by

$$Q_{e^\pm}(E,r) \simeq 2^6 N_{CR_p} \, n_N(r) c\sigma_{pp} \left(\frac{24E}{\text{GeV}} \right)^{-\alpha_\gamma} , \tag{4.32}$$

as described in [125]. Here, $n_N(r)$ is the nucleon number density, which we take to be proportional to the thermal electron number density with $n_N(r) = \frac{1}{1-\frac{1}{2}X_H} n_e(r)$ where $X_H = 0.24$ is the the primordial ^{4}He mass fraction. The thermal electron

density $n_e(r)$ can be modeled as a beta-fit of the form

$$n_e = n_{e,0} \left[1 + \left(\frac{r}{r_c} \right)^2 \right]^{-\frac{3}{2}\beta} \tag{4.33}$$

with $\beta = 0.49$ and $r_c = 54''$ [207] and assuming $n_{e,0} \sim 0.1$ cm^{-3} [87, 86]. The neutral pion mass is $m_{\pi^0} = 135$ GeV, ξ gives the pion multiplicity taken to be $\xi = 2$ for π^0, and $\sigma_{pp} = 32$ mbarn is the proton collision cross-section. The shape parameter δ is given by $\delta = 0.14\alpha_\gamma^{-1.6} + 0.44$. For this case, when fitting to both the radio and gamma-ray data using the same free parameters as the previous section (but with E_{cut} excluded and N_{CR_e}, α_e replaced with N_{CR_p}, α_p) we are unable to find a reasonable fit, due to the significant difference between the index required to fit the synchrotron emission to the radio simultaneously as the π^0 decay to the gamma-ray emission. Additionally, if we ignore the contribution from π^0 gamma rays and assume that synchrotron and IC emission from secondary electrons are dominantly responsible for the observed radio and gamma-ray emission we similarly do not find a good fit to the data.

Instead, we determine α_p and N_{CR_p} by only fitting the π^0 gamma rays to the Fermi data, while leaving the other parameters to be determined separately. With the only contribution to the fit being from the π^0 gamma ray contribution, we are find a best fit with $\alpha_p = 2.66$ and $N_{CR_p} = 8.89 \times 10^{-8}$ GeV^{-1} cm^{-3}, also listed in table 4.3. The gamma-ray spectrum is shown in figure 4.4 along with a few other values of α_p, normalized appropriately. In the selection of the remaining parameters that need to be determined (i.e. B_μ and N_{SL}) we are mainly constrained by the requirement that we are consistent with the field values in section 4.2.1 while not overproducing the radio emission, and N_{SL} does not result in IC emission that significantly impacts the spectrum from pion decay gamma rays in the Fermi data energy range. In figure 4.5 we show the result of

this procedure with various values for the magnetic fields, and for simplicity a single starlight normalization $N_{SL} = 5 \times 10^{-12}$ in accordance with the discussion of section 4.2.2. In this figure, two things are evident: first, the gamma-ray emission provides a good fit to the Fermi data; and second, the spectral index required for this fit results in a significant mismatch to the radio data regardless of normalization or field strength. The index of the CRp distribution obtained is in agreement with other studies that suggest $\alpha_p \sim 2.5 - 2.75$ [52, 180, 251].
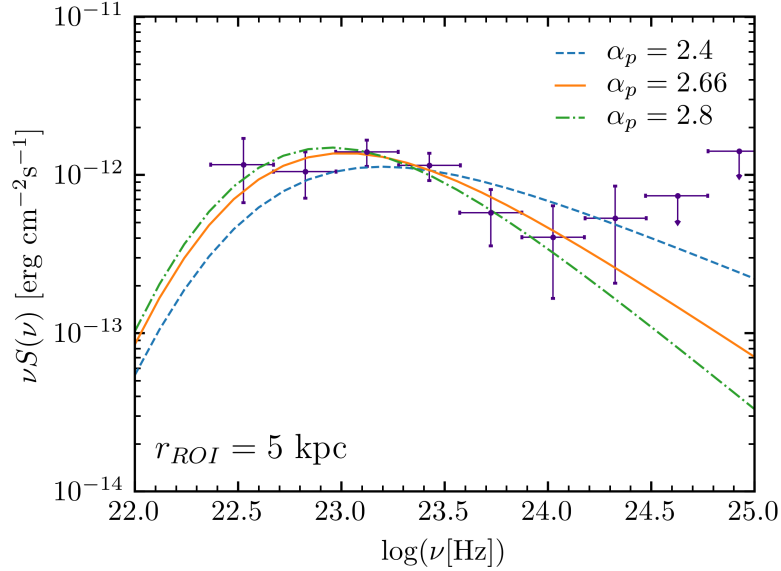
Figure 4.4: Spectrum due to π^0 decay for a few values of α_p, normalized to the Fermi data from [10].

α_p	N_{CR_p} (GeV^{-1}cm^{-3})	$\chi^2_{min}/d.o.f$
2.66	8.89×10^{-8}	2.25 / 5

Table 4.3: Parameters and their values in our best-fit model for a power law primary proton source.
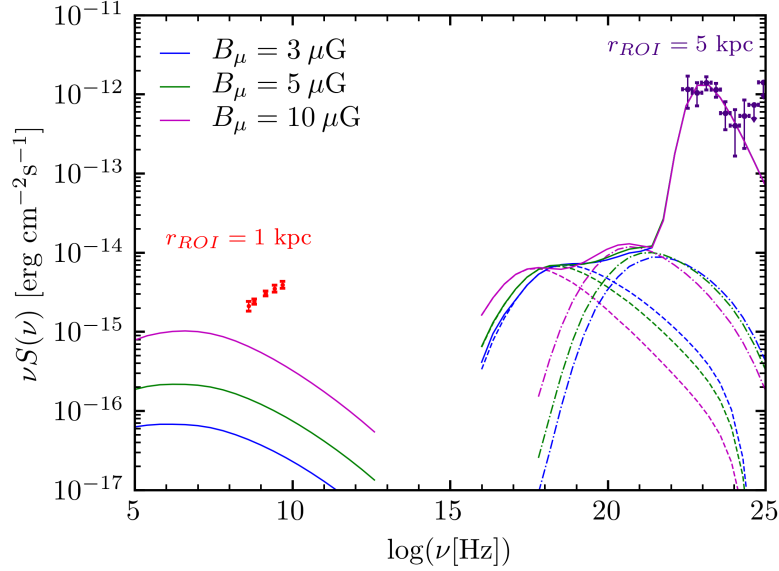
Figure 4.5: Emission due to decay of $\pi^{\pm}, \pi^0$ into $e^{\pm}, \gamma$. Parameters were determined by fitting the pion decay gamma rays to the Fermi data with only the normalization N_{CR_p} and the injection index α_p as free parameters, and for a selection of magnetic field strengths. The dashed lines are the CMB IC contribution, the dash-dot are the SL IC contribution, and the total emissions are the solid lines. Radio data are taken from [320] and gamma-ray data are taken from [10].

Cosmic-ray Proton Power

As we did in section 4.5.1, we can again compare the power injected into CRp as implied by our fit parameters to the energy budget of SNe produced CRp. The power injection from SNe to CRp is of the same form as the CRe;

$$P_{SN,\,p} = \eta_p E_{SN} \Gamma_{SN} \tag{4.34}$$

where the only difference is in the value of the power injection efficiency, η_p. While [300] inferred a value of $\eta_p \sim 10^{-5} - 10^{-4}$, others have adopted higher values of $\eta_p \sim 10^{-3}$ [93]. Additionally, gamma ray observations suggest that up to $3 - 30\%$ of the SN kinetic energy can be imparted into the cosmic-ray protons [8, 305]. We

therefore have quite a large range of possible values, finding $P_{SN,p} \approx 5.1 \times 10^{35}$ erg s^{-1} for our lower bound and $P_{SN,p} \approx 1.53 \times 10^{40}$ erg s^{-1} as an upper bound.

To calculate the implied CRp power from our models, we take into account the diffusive properties of the CRp source distribution n_{CR_p}. Noting that for the heavier cosmic-ray protons the radiative energy losses of equation (4.8) are unimportant, we can consider only the propagation of the CRp by diffusion. The steady-state distribution of cosmic-ray protons has a characteristic diffusion timescale of $t_D(E) \approx r_h^2 / D(E)$ [301, 252, 155, 209, 50], which gives us an injection source term $n_{CR_p}(E)/t_D(E)$. We then have for the power injected into CRp:

$$P_{CR_p} = \int dV \int_{m_p}^{\infty} dE \left(E \frac{n_{CR_p}(E)}{t_D(E)} \right). \tag{4.35}$$

In figure 4.6 we show the contours of the implied power injected into CRp. In this case the power determined by the fit parameters still exceeds the estimated SNe power injection. This discrepancy between the SNe estimates and our calculated power is not as extreme as in the primary P_{CR_e} scenario for lower magnetic fields, though for higher field values, the CRe power is just over an order of magnitude greater than the upper SNe power, as opposed to the almost two order of magnitude difference for the CRp seen here.

4.5.3 Multi-component cosmic ray source model

In the previous sections we were working under the assumption that the cosmic-ray source was dominated by either primary production of CRe or hadronic production of secondary CRe and π^0 gamma rays. However, another possible scenario would be where both of these cosmic-ray production mechanisms are incorporated. We can therefore consider a multi-component model that includes contributions of both the primary source as well as the hadronically produced
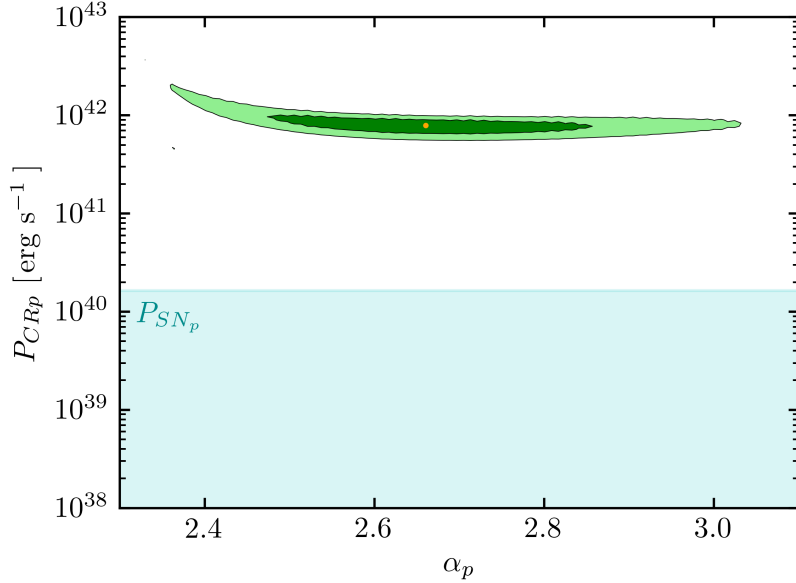
Figure 4.6: 1σ and 2σ contours of power injection into CR_p according to equation (4.35) with N_{CR_p} and α_p as free parameters and fitting only contributions from π^0 gamma rays. The light blue region shows a portion of the range estimate for the proton power injection due to SNe as calculated using equation (4.34). The best-fit point is given by the orange dot.

sources. For the gamma-ray source term, the only contribution is from the decay of pions produced in inelastic hadronic collisions as described by (4.31). The electron source term for the multi-component model is the sum of the source terms in equations (4.23) and (4.32):

$$
\begin{aligned}
Q_{e^\pm}^{MC}(E,r) = &\, N_{CR_e} \left(\frac{E}{\text{GeV}} \right)^{-\alpha_e} e^{-E/E_{cut}} \\
&+ 2^6 N_{CR_p}\, n_N(r) c\sigma_{pp} \left(\frac{24E}{\text{GeV}} \right)^{-\alpha_\gamma}
\end{aligned}
\tag{4.36}
$$

with, $\alpha_\gamma = 4/3\,(\alpha_p - 0.5)$. The best-fit results are listed in table 4.4 along with a selection of parameter sets with fixed magnetic fields or fixed N_{SL}. The SED for the best fit is shown in figure 4.7.

For the injection indices, we obtain values of $\alpha_e = 2.04$ and $\alpha_p = 2.75$, which

α_e	α_p	E_{cut} (GeV)	N_{CRe} (GeV^{-1}s^{-1}cm^{-3})	N_{CRp} (GeV^{-1}cm^{-3})	B_μ (μG)	N_{SL}	$\chi^2_{min}/d.o.f$
2.04	2.75	1658	1.32×10^{-26}	7.48×10^{-8}	4.8	1.10×10^{-12}	2.27/5
2.09	2.75	854	3.29×10^{-26}	5.24×10^{-8}	[a]3	1.02×10^{-12}	2.41/6
1.92	2.71	1633	6.17×10^{-27}	7.75×10^{-8}	[a]7	1.12×10^{-12}	2.42/6
1.71	2.67	1550	2.73×10^{-27}	7.01×10^{-8}	[a]10	1.44×10^{-12}	2.80/6
1.57	2.70	1353	1.77×10^{-27}	7.13×10^{-8}	12.4	[a]5×10^{-12}	3.25/6

Table 4.4: Parameters and their values in a selection of well fitting models for the multi-component model, along with the corresponding χ^2_{min}. The best-fit model parameters are given in the top row and the corresponding SED is plotted in figure 4.7. Parameters that are held fixed in a given model are denoted with the a prescript.
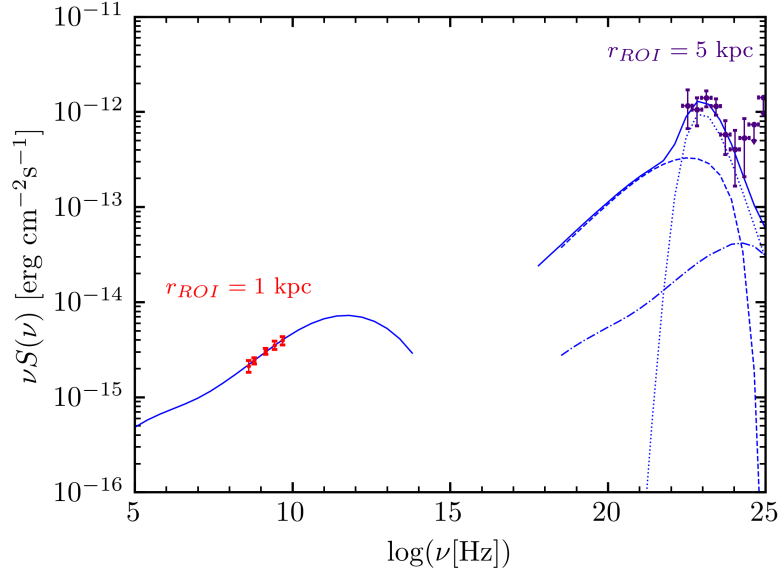
Figure 4.7: SED of the best-fitting multi-component CR model, including contributions from primary CRe, as well as secondary CRe and gamma rays of hadronic origin. Fit parameters are listed in the top row of Table 4.4. The dashed lines are the IC CMB contribution, the dash-dot are the IC SL contribution, dotted lines are the π^0 gamma-rays, and the total emissions are the solid lines. Radio data are taken from [320] and gamma-ray data are taken from [10]

are both within the ranges discussed in sections 4.5.1 and 4.5.2, while the normalization factors N_{CRe} and N_{CRp} do not deviate significantly from the values found in those sections. The cutoff energy $E_{cut} = 1658$ GeV is in line with the $\sim$ TeV level used in previous cosmic-ray studies [118, 123, 212, 140, 122], but higher than in the primary-only case. The magnetic field is also higher here than in the primary only case and is in good agreement with M31 magnetic field estimates. The similarity between the parameters of the multi-component model and the primary-only or secondary-only models is reflected in that for the multi-component model each of the two components (primary and secondary) have separate regimes of dominance. That is to say, the radio is predominantly due to the primary CRe whereas the gamma-rays are mainly due to the neutral pion decay gamma rays.
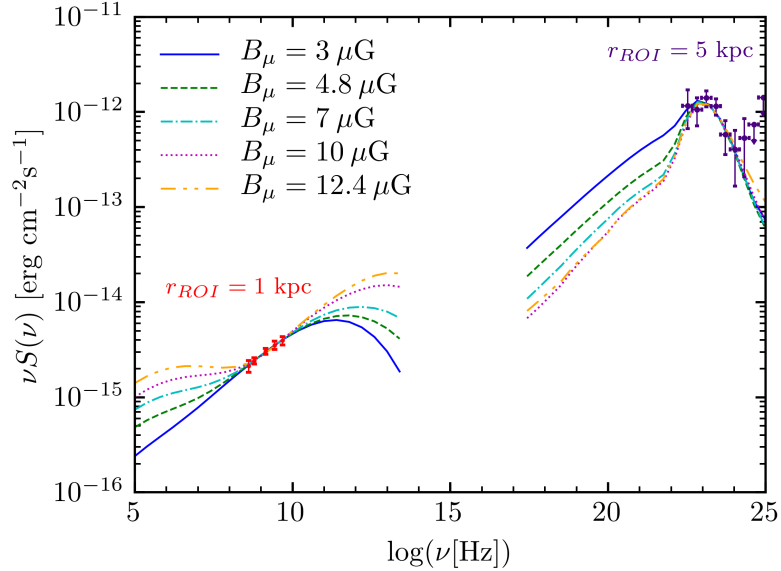
Figure 4.8: SED of the multi-component CR model for each of the parameter sets in table 4.4. Radio data are taken from [320] and gamma-ray data are taken from [10]

This resolves the discrepancy in the model with purely hadronically produced CRe between the spectrum of radio data and the predicted synchrotron emission. In addition to the best-fit model, we also list in table 4.4 models in which we hold the magnetic field fixed and fit for the remaining free parameters. We do this as well where we instead hold N_{SL} fixed to the value discussed in 4.2.2 and fit the remaining parameters. In either case, the parameter held fixed is denoted in table 4.4 by the 'a' superscript. The spectra for each model in 4.4 are plotted in figure 4.8. With different field strengths we are still able to find good fits to the data, with only very slight changes to the χ^2_{min}. This suggests that in the multi-component model there is no issue with a suppressed magnetic field as in the primary-only case. Again we see that the starlight normalization is highly suppressed and the IC emission is heavily dominated by the CMB component. Since this appears to be a fairly extreme scenario for the central region of the

galaxy, we try to achieve a more reasonable value by holding the normalization fixed at $N_{SL} = 5 \times 10^{-12}$ as derived in section 4.2.2 and fit the remaining parameters. We are still able to achieve a good fit, however it requires a relatively higher magnetic field of $B_\mu = 12.4\mu G$ in order to suppress the stellar IC component, as well as a low injection index of $\alpha_e = 1.57$.

We once again compare the power injection into CRe and CRp implied by the parameters of our fit with the estimated SN injected power. Noting that the source term parameters for the CRe and CRp do not deviate significantly from the values found in section 4.5.1 and 4.5.2, similar results in this comparison can be expected here. In fact, that is essentially what we see in figure 4.9, wherein we show the implied CR power from our models for the various magnetic field values compared with the SN power injection estimates of sections 4.5.1 and 4.5.2. We see that the implied CRe power injection decreases for models with higher magnetic field (cf. figure 4.3), while the CRp injection remains relatively constant with some slight increase due to suppression of the primary CRe induced IC emission. However, neither are within their respective ranges for the SN source power. Although there is a discrepancy between the implied power injection of our cosmic-ray parameter sets and the estimated supernovae contribution, the great deal of uncertainty in the SNe power estimates makes it difficult to make concrete statements on the viability of these models on this basis alone.

4.6   Diffuse X-ray Emission in M31

While the focus of this analysis has been on the radio and gamma-ray emission, X-ray emission in M31 provides another potential avenue to study. However, several observations of the X-ray emission in the bulge of M31 have detected the presence of an unresolved diffuse component, using data from *ROSAT* [297, 298],
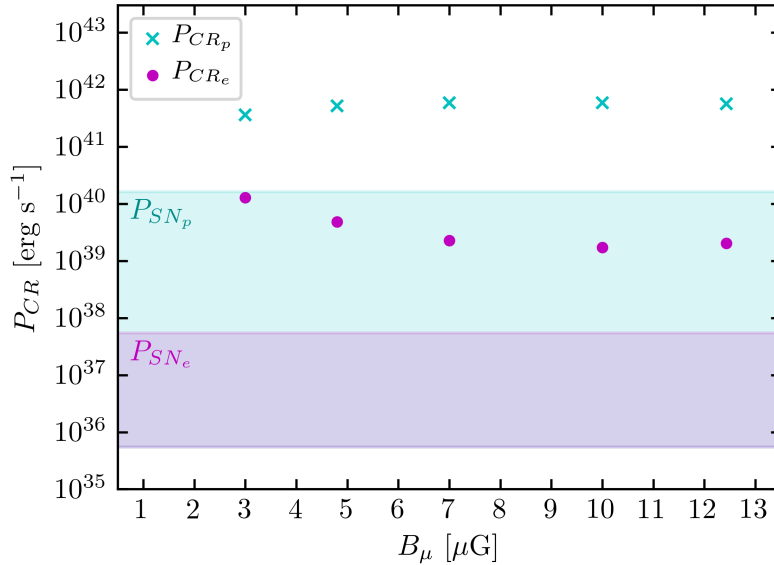
Figure 4.9: Power injection into CRe and CRp for each of the models in table 4.4, plotted against magnetic field. Note that the region of SNe power into CRp (cyan) fully overlaps the SNe power injection into CRe region (magenta).

XMM-Newton [280], and *CHANDRA* [205]. In each of these studies, diffuse X-ray flux in the inner ~ 1 kpc of M31 is observed at a flux level of falling roughly between $\sim 3-5 \times 10^{-12}$ erg cm^{-2} s^{-1}, and can likely be attributed to the presence of thermal hot gas and unresolved X-ray point sources. We note that this observed X-ray emission within 1 kpc has a higher flux than the X-rays produced in any of our cosmic-ray models from the previous sections, even despite the computed X-ray emission being within a 5 kpc radius. We thus conclude that for these cosmic ray models and our astrophysical setup the X-ray emission in M31 does not provide particularly useful information due to the bright diffuse emission in the bulge of M31 being considerably brighter than what we would obtain in our models.

4.7 Conclusion

We have examined the possibility of a cosmic-ray origin for the multi-wavelength emission in the Andromeda galaxy, specifically addressing the origin of the recently detected extended gamma-ray emission. We considered three models for the production of cosmic rays. First, we considered a primary injection of CRe obeying a power law with an exponential cutoff, then considered production of secondary CRe and gamma rays produced from interactions of a power law distribution of primary CRp. Finally, we looked at a multi-component model that incorporates both of these cosmic-ray sources. We then fit the synchrotron and IC fluxes arising due to the presence of the primary and secondary CRe, as well as the gamma ray emission from neutral pion decay, to available radio data and a recent Fermi gamma-ray detection in M31.

For the primary CRe scenario, we find best fit parameters for the injection spectrum $\alpha_e = 2.14$ and cutoff energy $E_{cut} = 514$ GeV. The injection index is consistent with expected values for CRe sources such as SNR. The cutoff energy is slightly lower than expected, however not wholly inconsistent with expected values on the order of TeV. The magnetic field value of $B_\mu = 1.7$ μG and the starlight normalization are both suppressed in the fit. We also considered higher magnetic fields and renormalized the synchrotron emission to match the radio data. This suppresses the IC gamma-ray emission, requiring that we account for the Fermi data separately which was done in the multi-component model. We then compared the power injection into CRe implied by our model with the expected range of power injection due to SNe. We saw that even by increasing the magnetic field in order to lower the normalization constant N_{CRe}, the power injection implied by our models was well above the expected output from astrophysical sources such as PWNe and SNe.

In the case where we considered contributions from only secondary cosmic rays of hadronic origin, we were unable to find a good fit to both the radio and gamma-ray data simultaneously. Rather, we assumed that the gamma rays were purely from the neutral pion decay and found a CRp distribution index of $\alpha_p = 2.66$, consistent with previous results for π^0 gamma-ray studies, along with a CRp distribution coefficient of $N_{CR_p} = 8.89 \times 10^{-8}$ GeV^{-1} cm^{-3}. With this arrangement we then manually selected the magnetic field and starlight energy density, and found that for a variety of field strengths the calculated flux remains below the radio data, and even for a higher selected value of $N_{SL} = 5 \times 10^{-12}$ there was no conflict between the IC emission and the gamma-ray data. We again compared the power injection into CRp from SNe with the implied power output of our models, and found that the CRp injection is also greater than the estimated SNe output.

Finally, we consider a combined "multi-component model" that incorporates the contributions from both the primary CRe as well as the secondary CRe of hadronic origin. Although here the power budget concerns remained due to minimal variation in the best fit normalization constants, this scenario gives the best overall fit to the data, while still providing similar parameter values as in the primary-only and secondary-only cases. We found the best-fit $\alpha_e = 2.04$ and $\alpha_p = 2.75$, both similar to the values discussed in sections 4.5.1 and 4.5.2 respectively, while the best-fit magnetic field was found to be $B_\mu = 4.8$ μG and E_{cut} was 1658 GeV. Additionally, the multi-component model offers a large degree of flexibility in the parameter choices, as evidenced by good fits for a range of multiple magnetic fields values and E_{cut} on the order of a few TeV, as well as for higher N_{SL} values in accordance with the observed stellar luminosity in the central region of M31. In our final power comparison we saw similar results as

in the primary-only and secondary-only scenarios. That is, both the implied CRe and CRp power in our models were greater than the estimated power output from astrophysical sources, and this held at a wide range of magnetic fields values. This suggests that although the spectra can be fit well with a multi-component model, the input power needed for the cosmic-ray sources is consistently more than an order of magnitude above what is expected from supernova as galactic cosmic-ray accelerators. Furthermore, as mentioned in the introduction and discussed more thoroughly in the original detection paper [10] and subsequent Fermi M31 studies [133, 151], the gamma-ray emission does not appear to correlate with star-formation or gas-rich regions. CRp produced at larger radii that then diffuse into the emission region may contribute to the observed signal, although this does not address the lack of gas for the CRp to interact with in the interior regions of the galaxy. Another possibility is that the CRp are remnants from a previous period of higher star-formation. However, the stellar population of the bulge is dominated by stars with ages $\gtrsim 4 - 12$ Gyr [248, 275, 126], compared to a CRp escape time of $\sim 10 - 100$ Myr, which suggests that the majority of CRp would have likely left the system in the time since this higher star-formation activity in M31. This morphological point along with the power discrepancy combine to disfavour a purely CR explanation, particularly one that relies on π^0 gamma-rays from CRp to explain the observed gamma-ray emission.

Chapter 5

X-Ray Shapes of Elliptical Galaxies and Implications for Self-Interacting Dark Matter

5.1 Introduction

The cold dark matter (CDM) paradigm has been immensely successful in explaining many aspects of the universe and is particularly strong at describing large-scale structure [286]. This has naturally led to CDM as the benchmark for dark matter (DM) studies and the most extensively investigated class of DM candidates. However, the lack of indirect or direct observational evidence of collisionless cold dark matter (e.g. WIMPs), along with purported shortcomings of CDM at small scales has led to interest in alternative DM frameworks. In regards to the latter point, challenges at small scales such as the missing satellites [197, 234], "Too-Big-To Fail" [62, 63], and core-cusp [148, 233, 192] problems are troubling for the CDM paradigm. Solutions to these problems based on bary-

onic effects alone have been explored [67, 243, 168, 19], however it is not clear that these effects are sufficient to account for the discrepancies between observations and simulations. An intriguing solution to these problems is to consider self-interacting dark matter (SIDM) that is not fully collisionless.

N-body simulations as well as analytical arguments suggest that DM self-interactions can have observable effects on the macroscopic properties of halos that can address some of the problems that arise in a collisionless CDM scenario. Particularly, self-interactions can flatten the centrally peaked cusps in the inner regions of galaxies and are capable of disrupting the development of the dense satellite galaxies expected from simulations that are at the crux of the core-cusp and TBTF problems [318, 254, 137]. SIDM is also predicted to affect the shapes of DM halos through isotropized particle scattering [254, 284, 115], producing more spheroidal halos than seen in CDM. These predictions for the macroscopic effects of SIDM provide an opportunity to probe the microscopic properties of the DM interaction. Specifically, the figure of merit for SIDM is the ratio of the collisional cross-section to the DM mass σ/m. In order to alleviate the small-scale challenges discussed above, several groups have found that the necessary interaction strength is roughly $\sigma/m \approx 0.5 - 10$ cm^2/g [318, 254, 137, 284, 115, 72].

However, studies of the predicted effects of SIDM in comparison with observations have been performed that place constraints on the interaction cross section. These observational probes include cluster lensing [231, 254, 20], mergers [262, 214], and X-ray ellipticities [81]. While early constraints on SIDM in clusters suggested low cross section values of $\sigma/m \lesssim 0.02$ cm^2/g [231], subsequent higher resolution simulations indicated that these limits were overly optimistic and that cross sections of $\sigma/m \lesssim 1$ cm^2/g are consistent with simulations across a variety of mass scales [268, 254]. Furthermore, observations at a wide range of halo masses

indicate that a velocity dependent cross-section is needed in order to alleviate small-scale issues while also abiding by cluster constraints [193], thus providing compelling motivation for studies at a range of halo mass scales. Specifically, the interaction cross-section must decrease with larger relative velocity (e.g in clusters). This can naturally be achieved in SIDM models wherein the interactions are governed by a Yukawa potential [142, 208, 71, 312, 311].

An interesting class of targets for SIDM studies is elliptical galaxies with halo masses of order $\sim 10^{12} - 10^{13} M_\odot$. In particular, elliptical galaxies are interesting to DM studies in part because the interstellar X-ray emitting gas fills the gravitational potential, acting as a tracer of the underlying gravitational potential well beyond the regime of stellar dynamics [79]. However, this relies on the assumption that the gas is in a state of hydrostatic equilibrium with the potential. If the elliptical galaxies in question can reasonably be treated as being in hydrostatic equilibrium, the gas traces the gravitating potential, and determination of shape of the the X-ray gas allows for probes of the DM dominated mass distribution. Thus, by observing the X-ray shapes of elliptical galaxies, the shape of the DM halo can be inferred and compared with predictions of CDM and SIDM halos shapes from simulations. This "X-ray Shape Theorem" first was developed by [48] and has been applied to studies of elliptical galaxies and clusters [74, 75, 77, 78, 81].

Applying this method to the NGC 720 elliptical galaxy using Chandra X-ray data, Ref. [81] determined the ellipticity of the DM halo was roughly $\epsilon \approx 0.35 - 0.4$. Simulations for cross-sections of $\sigma/m = 0, 0.1, 1$ cm^2/g showed that the NGC 720 ellipticity was consistent with interaction cross-section ~ 0.1 cm^2/g as well as with CDM ($\sigma/m = 0$ cm^2/g) [254]. While these results presented convincing evidence that $\sigma/m = 1$ cm^2/g was incompatible with the NGC 720 observation, strong assertions for lower cross-sections are difficult to make given

the singular observation and significant scatter in the ellipticities of the simulated halos. Expanding on the NGC 720 results by performing a shape analysis of an ensemble of elliptical galaxies can potentially lead to more concrete statements. Still, the results of the X-ray ellipticity measurements of NGC 720 have been useful in applications to a wide range of DM models including hidden sector hydrogen [113], dissipative and "double-disk" dark matter [139], charged DM [222, 141, 12], as well as alternative gravity theories for DM phenomena such as MOND [230]. By analyzing a sample of elliptical galaxies while leveraging the capabilities of the Chandra and XMM telescopes, we aim to build upon the previous X-ray shape measurements and provide data on the ellipticities of $M \sim 10^{12} - 10^{13} M_\odot$ mass DM halos that will impact future studies of SIDM models.

The remainder of this chapter is as follows. In section 5.2 we describe the calculations needed to relate the mass distribution to the X-ray ellipticities, including discussion of the hydrostatic equilibrium condition. In section 5.3 we present the criteria for galaxy sample selection and describe the Chandra and XMM data reduction procedures. We describe the analysis of the processed data including the ellipticities and surface brightness profile calculations and fitting procedures in section 5.4. We present the results of these procedures in section 5.5 and discuss the implications of them for the DM self-interaction cross-section. Finally we present conclusions in section 5.6.

5.2 X-ray Emissivity as a Tracer of the Mass Distribution

5.2.1 Gravitational Potential of an Ellipsoidal Mass Distribution

For this study we use the "X-ray Shape Theorem" [48, 74, 75, 77, 78, 75, 81] in order to determine the shape of the gravitating mass through observations of the X-ray emitting gas. This approach relies on the assumption that the gas is in hydrostatic equilibrium and therefore traces the gravitational potential. Thus, it is necessary that we are able to determine the gravitational potential produced by the total mass distribution. The gravitational potential for an ellipsoidal mass distribution, $\rho(a)$, is given by the expression [47, 80]

$$\Phi(a) = -\pi G p q \int_0^\infty \frac{\psi\left(a^2(\tau, \mathbf{x})\right) \, d\tau}{\sqrt{(\tau+1)(\tau+p^2)(\tau+q^2)}} \tag{5.1}$$

where,

$$a(\tau, \mathbf{x})^2 = \frac{x^2}{\tau+1} + \frac{y^2}{\tau+p^2} + \frac{z^2}{\tau+q^2} \tag{5.2}$$

and

$$\psi\left(a^2(\tau, \mathbf{x})\right) = \int_{a^2(\tau, \mathbf{x})}^\infty \rho(\tilde{a}^2) d\tilde{a}^2. \tag{5.3}$$

The elliptical radius a is defined as

$$a^2 = x^2 + \frac{y^2}{p^2} + \frac{z^2}{q^2}. \tag{5.4}$$

In this notation, the principal axes a, b, and c are aligned along the x, y, and z axes respectively with the values $p = b/a$ and $q = c/a$ being the axis ratios. The ellipticity is defined as $\epsilon = 1 - p = 1 - b/a$. As we are interested in the flattening

of the halo profile, we consider the two cases of oblate and prolate spheroids defined by $q = p$ (oblate) and $q = 1$ (prolate) with the axis of symmetry along the line of sight. This in effect brackets the range of projected ellipticities of a triaxial ellipsoid. We take into consideration the following three mass distribution densities in our analysis: (i) a Navarro-Frenck-White (NFW) profile [241], (ii) a Hernquist profile [172], and (iii) a pseudo-isothermal profile (pIso). Explicitly, these are of the form

$$\text{NFW:} \qquad \rho \propto \frac{1}{a(a_s + a)^2} \tag{5.5}$$

$$\text{Hernquist:} \qquad \rho \propto \frac{1}{a(a_s + a)^3} \tag{5.6}$$

$$\text{pIso:} \qquad \rho \propto \frac{1}{(a_s^2 + a^2)} \tag{5.7}$$

where a_s is the scale radius.

5.2.2 Hydrostatic Equilibrium – Gas Density and X-ray Emissivity

The isolated, relaxed elliptical galaxies are assumed to be in a state of hydrostatic equilibrium so that we may treat the X-ray gas as a tracer of the potential. This is expressed as a balance of the forces from internal gas pressure and gravitation given by the relation:

$$\boldsymbol{\nabla} P_{gas} = -\rho_{gas} \boldsymbol{\nabla} \Phi \tag{5.8}$$

Where P_{gas} is the pressure of the gas, ρ_{gas} is the gas mass density and Φ is the total gravitational potential. Taking the curl of both sides yields $(\boldsymbol{\nabla} \rho_{gas}) \times (\boldsymbol{\nabla} \Phi) =$

0, implying that surfaces of constant gas density are also surfaces of constant gravitational potential. For approximately isothermal gas distributions, the X-ray emissivity (j_X) is related to the gas density as $j_X \propto \rho_{gas}^2$ [75, 77]. Since surfaces of constant ρ_{gas} are isopotential surfaces, it is also true that surfaces of constant ρ_{gas}^2, and consequently, surfaces of constant j_X are isopotential surfaces as well [48, 74, 77, 78, 75, 81]. In practice, what we observe is not the 3-D emissivity itself, but rather the X-ray surface brightness, Σ_X, which is the 2-D projection of the emissivity along the line of sight and is given in terms of the gas density by the relation:

$$\Sigma_X \propto \int_{los} j_X \propto \int_{los} \rho_{gas}^2. \tag{5.9}$$

For an isothermal gas equation 5.8 can be solved for the the gas density [47, 75]:

$$\rho_{gas}(a) = \rho_{gas,\,0} \exp\left[-\frac{\mu m |\Phi_0|}{k_b T}\left(1 - \frac{\Phi(a)}{\Phi_0}\right)\right] \tag{5.10}$$

We express this in a more compact manner as

$$\tilde{\rho}_{gas}(a) = \exp\left[-\Gamma\left(1 - \tilde{\Phi}(a)\right)\right] \tag{5.11}$$

Where the tildes denote the dimensionless form for the expression normalized at the galaxy center and $\Gamma = \mu m |\Phi_0|/k_b T$.

Once a model for the mass distribution (Eqs. 5.5-5.7) has been chosen, the parameters of interest in modeling the X-ray emission of a galaxy are a_s, Γ, and ϵ, along with an appropriate normalization of the surface brightness. In each panel of figures 5.1 and 5.2 we show the the individual effects of varying each of these parameters on the surface brightness profiles and ellipticity profiles respectively. For illustrative purposes only we adopt base parameter values of $a_s = 30''$, $\Gamma = 5$,

and $\epsilon = 0.4$ and assume an NFW profile. While the surface brightness profile unsurprisingly has a strong dependence on a_s and Γ, the effects of varying the ellipticity of the halo are less pronounced. In the X-ray ellipticity profile, the a_s and Γ parameters have almost no discernible effects aside from a slight decrease in observed ϵ_X at the lowest values ($a_s \sim 20$", $\Gamma \sim 4$). Naturally, the ellipticity of the matter distribution used in the model has a major impact on the X-ray ellipticity profile. In addition, for more elliptical mass distributions the X-ray profile also tends to exhibit a radial dependence.
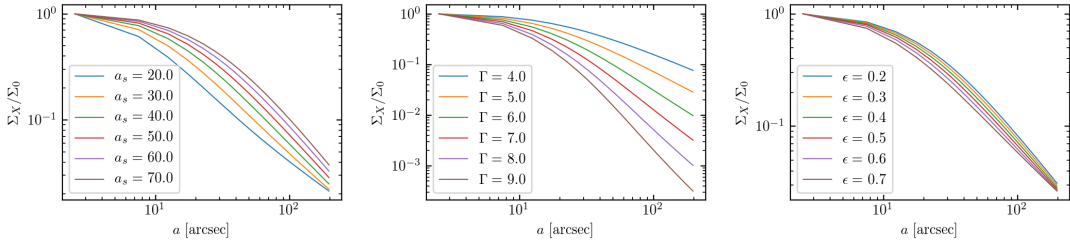
Figure 5.1: Normalized surface brightness profiles for a fiducial NFW galaxy with $a_s = 30''$, $\Gamma = 5$, and $\epsilon = 0.4$ while varying a_s *(left)*, Γ *(middle)*, and ϵ *(right)*.
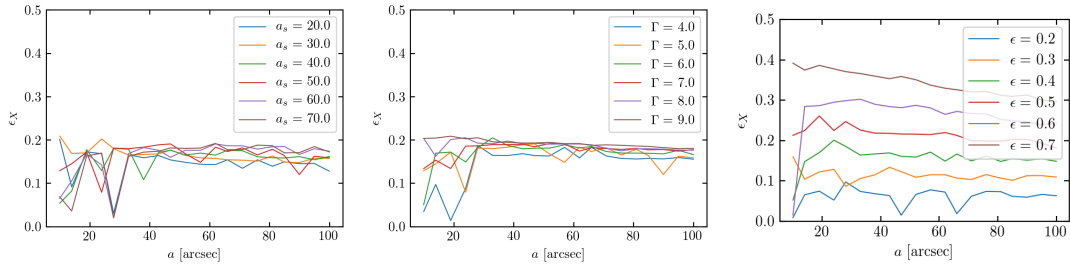
Figure 5.2: Ellipticity profiles for a fiducial NFW galaxy with $a_s = 30''$, $\Gamma = 5$, and $\epsilon = 0.4$ while varying a_s *(left)*, Γ *(middle)*, and ϵ *(right)*.

5.3   Galaxy Sample and Data Reduction

5.3.1   Galaxy Selection

The selection of galaxies used in this analysis is guided by a few conditions that justify the assumption of hydrostatic equilibrium. We focus our attention on relaxed, isolated elliptical galaxies. Thus, we seek candidates that exhibit regular, circular or elliptical X-ray morphologies as expected for a suitably relaxed galaxy [184, 79]. In particular, we avoid galaxies with bright central AGN or significant AGN feedback. The elliptical galaxy NGC 4374 (M84) [94] provides an example case where this relaxation condition does not hold due to significant disruption of the X-ray gas from AGN feedback. The isolation criteria include (i) no close neighbors, (ii) no signs of interaction, and (iii) no evidence for a recent merger. Additionally, since the stellar mass dominates the overall mass distribution in the central regions, we seek galaxies for which existing observational data extends far beyond the effective stellar radius. This is necessary in order to probe the underlying mass distribution in the outer regions where the dark matter component is the dominant contribution to the gravitational potential. The galaxies that fit these criteria and are used in this analysis are listed in 5.1 along with some basic properties including their distance and K-Band effective radius taken from the Two Micron All Sky Survey (2MASS) Extended Source Catalog (XSC) [181].

Galaxy	Dist. (Mpc)	”/kpc	r_e (kpc)
IC4451	55.8 [287]	0.27	4.07
IC4956	70.1 [304]	0.34	4.59
NGC1521	69.5 [313]	0.34	5.53
NGC4125	24.0 [313]	0.12	3.65
NGC4555	110 [277]	0.53	5.97
NGC57	70.1 [304]	0.34	4.98
NGC6482	59.2 [210]	0.29	3.47
NGC7785	48.4 [304]	0.23	4.05
NGC7796	51.3 [313]	0.25	4.03
NGC953	66.3 [112]	0.32	2.91
NGC720	25.7 [306]	0.12	3.14

Table 5.1: Sample of galaxies used in this analysis. References for the distances are provided. The effective radius r_e is the K-band effective radius taken from the 2MASS XSC catalog [181].

| | XMM | | Chandra | |
| | MOS1 + MOS2 | | | |
Galaxy	ObsID	Exp_{1+2} (ks)	ObsID	Exp. (ks)
IC4451	0503480501	4.26 + 6.02	13808	25.05
	0673080101	66.04 + 66.58	–	–
IC4956	0503480801	0.96 + 3.38	–	–
	0693190401	81.44 + 86.74	–	–
NGC1521	0552510101	98.15 + 100.82	10539	40.79
NGC4125	0141570201	98.15 + 100.82	2071	54.76
NGC4555	0403100101	62.64 + 62.26	1884	24.44
NGC57	0202190201	21.17 + 21.23	10547	8.69
NGC6482	0304160401	7.92 + 7.9	3218	18.94
	0304160801	5.21 + 5.39	19584	23.50
	–	–	19585	17.00
	–	–	20850	17.97
	–	–	20857	20.00
	–	–	20978	17.97
	–	–	20979	8.44
	–	–	20980	67.77

Table 5.2: Sample of galaxies and their corresponding ObsIDs and cleaned exposure times from XMM and Chandra (see section 5.3.2 for details). For the XMM exposure time, we show the individual cleaned exposure for each of the MOS1 and MOS2 EPIC cameras.

| | XMM | | Chandra | |
| | MOS1 + MOS2 | | | |
Galaxy	ObsID	Exp_{1+2} (ks)	ObsID	Exp. (ks)
NGC7785	0206060101	16.5 + 17.08	–	–
NGC7796	0693190101	47.64 + 56.74	7401	16.91
	–	–	7061	44.20
NGC953	0722360201	69.49 + 75.84	11262	5.92
	0762220101	95.55 + 95.04	14899	37.03
NGC720	602010101	81.76 + 81.71	492	21.69

Table 5.3: (Cont.) Sample of galaxies and their corresponding ObsIDs and cleaned exposure times from XMM and Chandra (see section 5.3.2 for details). For the XMM exposure time, we show the individual cleaned exposure for each of the MOS1 and MOS2 EPIC cameras.

5.3.2 Observations and Data Reduction

XMM-Newton

Each galaxy in our sample has at least one observation with the XMM-Newton telescope. We use archival data from the EPIC MOS1 and MOS2 cameras in the soft X-ray energy band $0.5 - 2$ keV. The processing of the data is performed with the Science Analysis Software (SAS[1] v16.1.0) and the Extended Source Analysis Software (ESAS) [281] following the steps outlined in the ESAS Cookbook[2] for diffuse emission. Specifically, we run the `emchain` program to prepare the events list products for use with the ESAS tasks. The `mos-filter` routine (which in turn calls the SAS routine `espfilt`) is used to remove periods of high background and determine the good time intervals (GTI). Light curves for each observation and MOS camera were inspected manually to ensure quality and observations that were not adequate (see e.g. the examples in the ESAS cookbook) are not included in this work. Nearly all observations exhibited some periods of high background that were subsequently removed. The remaining clean exposure times can be found in table 5.3. Images and exposure maps are then created for each observation and MOS camera using the `mos-spectra` routine and then combined. During the ESAS processing, images are binned to pixel sizes of $\sim 2.5'' \times 2.5''$.

Chandra

For nine out of the 11 galaxies in our sample there exists archival Chandra data that is suitable for this analysis. We restrict our analysis to the ACIS S3 chip and again consider the $0.5 - 2$ keV energy band. The data are processed with

---

[1]"Users Guide to the XMM-Newton Science Analysis System", Issue 15.0, 2019 (ESA: XMM-Newton SOC).

[2]`https://heasarc.gsfc.nasa.gov/docs/xmm/esas/cookbook/xmm-esas.html`

the CIAO 4.11[3] [152] software along with the corresponding Chandra calibration database (CALDB) v4.8.2 following the standard procedure for Chandra data. The Chandra data are binned into pixels of size $\sim 1"\times 1"$. For flare removal we use the `lc_clean` routine with default parameters and again manually inspect the light curves before proceeding. The remaining cleaned exposure times are shown for each ObsID in 5.3.

Point Source Removal

Since we are interested in the extended diffuse emission of the galaxies, it is necessary to remove bright point sources. Further, simply removing or masking the point sources is insufficient as the empty source regions in the image can significantly affect the ellipticity measurements. We therefore need to both identify the point sources and reasonably model the true diffuse emission in their place. For the identification of the point sources we use the `wavdetect` CIAO routine which provides a wavelet function source detection method. We supply this routine with the psf map built by running `fluximage` (and thus, `mkpsfmap`) for the Chandra data. In the XMM data we use a psfmap with a constant size of 5". The exposure maps created by `fluximage` and `mos-spectra` are used for the Chandra and XMM images, respectively. Identified source regions were then removed and filled using the CIAO `dmfilth` task which takes as input source and background regions produced by the `roi` routine. When running `dmfilth` we use the `POISSON` method, which replaces the source region by sampling from the Poisson distribution whose mean is that of the pixel values in the background region. In figure 5.3 we show example Chandra and XMM images of NGC 6482 before source detection, after source detection and replacement, as well as an image smoothed using the CIAO task `csmooth`.

---

[3]`https://cxc.cfa.harvard.edu/ciao/`

5.4 X-ray Ellipticity and Brightness Profiles

The ellipticities of the X-ray images for each galaxy in our data set are calculated using the image moments method as outlined in [309, 225, 75, 81, 92] which we briefly review. We begin by finding the centroid of a circular aperture at the desired semi-major radius a. The centroid of the radius is then calculated from the first order moment and the aperture shifted to that point. This process is repeated until the centroid shift changes less than some tolerance (roughly ~ 1 pixel). With the centroid found, we again start with a circular aperture of radius a, and calculate the second order image moments. These are effectively the elements of the inertia tensor of the image within the aperture, and allow the determination of the ellipticity within the aperture and orientation angle of the semi-major axis [309, 225, 75, 92]. This process is performed iteratively until the measured ellipticities and orientations converge. For the error estimation of the ellipticity profile, we follow the procedure of [81] and use a Monte Carlo approach. The pixel counts are assumed to follow Poisson statistics, so we create a simulated image by sampling the pixel values from a Poisson distribution with the original pixel count as the mean. We then calculate the ellipticity for each radii a as in the case of the original data image, repeating this for 100 instances. The standard deviation of the samples generated through this process is taken to be the 1σ error of our ellipticity.

In addition to the ellipticity radial profile, we also require the radial surface brightness profile in order to characterize the shape of the gravitating mass distribution. This is calculated by adding the counts within several annuli and dividing by the area of each annulus. Errors are calculated assuming Gaussian statistics (i.e. $\sigma_i \sim \sqrt{N_i}$ for N_i counts in annulus i) based on the lowest counts per bin in our samples being on the order of $\gtrsim 100$.

To perform the fitting procedure we begin by generating a model image for each assumed mass distribution and either prolate or oblate configuration based on the calculations in sections 5.2.1 and 5.2.2. The ellipticity and surface brightness profiles are calculated for the model image and a χ^2 statistic is used to determine the fit to the data. We then minimize the χ^2 statistic with a_s, Γ, and ϵ as free parameters using a Nelder-Mead simplex algorithm [244, 258] with a dimension dependent implementation of the expansion, contraction, and shrink parameters [157].

During this process, we treat the background modeling in a slightly different manner for the ellipticity and brightness profiles. The constant background model is estimated from the flattening of the brightness profile at large radii. This is illustrated in figure 5.4. For the ellipticity measurements, we subtract this background from the data and fit to the model generated profiles.

However, for the surface brightness profiles there can be odd behavior at the larger radius bins if the profile is calculated from the background subtracted image due to over subtraction. Essentially, some annular bins may have average counts per pixel slightly less than the background model. To avoid these problems we model the background simultaneously with the calculated model image rather than subtracting from the data. For the ellipticity profiles, over subtracting the observed counts is not an issue due to the elliptical aperture that contains the bright central regions and ensures that the average counts per pixel are greater than the background model.

5.5 Results

In figures 5.5 and 5.6 we show the best fit profiles for an NFW oblate mass configuration overlaid on the data for each galaxy. Figure 5.7 shows the best-fit

profiles for each configuration overlaid on the IC 4956 XMM data. The best-fit results for the XMM and Chandra data are summarized in tables 5.5 and 5.7 respectively, along with the reduced χ^2 values. In each case there are 37 total degrees of freedom. In most cases, the χ^2 statistic does not provide a quantitatively "good" fit to the data. In the case of the surface brightness profile this can at least partially be attributed to small error bars that amplify the χ^2 value despite what appears to be a fairly strong qualitative agreement between the data and the model. This is similar to what was found in the study of NGC 720 from Ref. [81]. However, it is clear from looking at figure 5.5 that a large contributor to the χ^2 is that the data for several of the galaxies does not follow the relatively flat ellipticity profiles of the model. This is not too surprising, since in this analysis we are assuming either prolate or oblate spheroidal mass-distributions with a constant ellipticity. More realistically, many of these galaxies are likely to be better represented by a triaxial distribution. They would therefore be expected to exhibit an isophotal "twist" and variations in their X-ray ellipticity profile [76, 269]. Rotating cooling flows may also alter the X-ray isophotes and contribute to variations in the radial profiles [76]. Nevertheless, since we have used the prolate and oblate configurations as a way to bracket the triaxial case we treat the results as relatively representative of the underlying mass distribution, though keeping in mind the potential need for more sophisticated modeling of the halo shape and possible astrophysical activity.

Another point of note is the radial range chosen for the fitting procedure. In our basic approach the minimum of the range was chosen to be 10 pixels for stability of the iterative moment method when calculating the ellipticity. The maximum radial limit was taken to be the point at which the emission region became background dominated (see figure 5.4) or the chip edge was reached. However, there

are good reasons to restrict this range from both ends on a galaxy-by-galaxy basis. In the inner regions, the stellar component contributes significantly to the overall mass distribution. For some of the galaxies in our sample, previous studies have been able to model the mass distribution to give a detailed description of how the mass profile and its constituent components change with radius (for example, see [226, 73, 183, 185, 250, 184]). In cases for which the full mass modeling has not been performed, it can be roughly assumed that the stellar mass has a non-negligible contribution within the effective radius r_e [65, 159]. In choosing a more restrictive minimum radius these characteristics of the galaxies should be kept in mind.

At larger radii, it is less clear that there is a natural maximum limit smaller than the background limit. In the NGC 720 study from Ref. [81], the upper radial limit $\sim 150''$ was chosen because of strange behavior observed at larger radii wherein the profile diverged from the values at smaller radii. Applying this to our sample there are potentially six galaxies (IC 4451, NGC 1521, NGC 57, NGC 6482, NGC 953, NGC 720) that exhibit this behavior to some extent for at least one of the observations. The origin of this divergence is unclear, although one physically motivated possibility is that the assumption of hydrostatic equilibrium does not accurately apply at these radii.

However, Ref. [81] also points out that for their observation the region $\gtrsim 150''$ is near the CCD edge which may be causing the strange behavior, and that observations with a wider field of view such as XMM could give insight into whether this is an observational or physical effect. In some of our galaxies, we find that in these large radius regimes the Chandra data exhibits this behavior to a much greater degree and diverges from the XMM profile. For example, the Chandra ellipticity diverges from the XMM values for NGC 6482, NGC 1521, and NGC 720

at $a \gtrsim 40, 20, 18$ kpc respectively (note that for NGC 720, 18 kpc $\approx 150''$). This suggests the strange behavior at large radii is likely due to observational effects rather than a failure of hydrostatic equilibrium, and furthermore that removing regions at large radii exhibiting this behavior could improve the accuracy of the fits.

Fits to the data were fairly consistent across the various mass configurations for a given galaxy. The slope parameter Γ varies from galaxy to galaxy ranging from $\sim 6-9$ but is otherwise roughly consistent across mass configurations. An interesting note is that the scale radius a_s in the pIso models is almost always considerably smaller than for the NFW or Hernquist profiles. As the scale radius characterizes the core in the pIso profile, this seems to suggest that the X-ray emission prefers a small-core, nearly isothermal $\rho \propto a^{-2}$ profile. In figure 5.8 we show the ellipticities for each galaxy and mass distribution configuration. For comparison, we also show the ellipticity for NGC 720 determined in [81] as horizontal colored lines. In general, their measured ellipticity falls comfortably within the range of the measured ellipticities of our ensemble. The values found in our analysis for NGC 720 tend to be slightly lower, although this could potentially be due to exposure corrections (see section 2 of [81]) or calibration effects. In addition, there does not appear to be any significant relationship between the ellipticity and the mass configuration for a given galaxy (e.g. NFW halos do not consistently result in the lowest ellipticities) .

		XMM							
		Prolate				Oblate			
Galaxy	Profile	a_s (")	Γ	ϵ	χ^2_{red}	a_s (")	Γ	ϵ	χ^2_{red}
	NFW	61.0	7.8	0.34	8.3	24.5	7.9	0.35	8.2
IC4451	Hernq.	126.2	7.0	0.31	9.8	45.8	6.8	0.34	9.6
	pIso	10.2	6.6	0.32	10.2	4.8	7.4	0.26	14.1
	NFW	40.7	8.4	0.17	0.9	15.8	8.4	0.19	0.9
IC4956	Hernq.	85.0	7.8	0.16	1.0	34.2	7.8	0.16	1.1
	pIso	6.1	7.0	0.15	0.9	2.4	7.4	0.12	1.2
	NFW	56.9	7.9	0.43	13.1	21.7	8.0	0.44	12.7
NGC1521	Hernq.	104.6	6.8	0.44	14.3	40.8	6.9	0.46	13.7
	pIso	8.7	6.6	0.42	14.0	2.7	6.9	0.49	13.6
	NFW	77.0	7.4	0.48	1.3	29.0	7.6	0.5	1.2
NGC4125	Hernq.	123.9	6.2	0.48	1.3	49.6	6.3	0.51	1.3
	pIso	11.2	6.2	0.48	1.3	4.2	6.3	0.52	1.2
	NFW	24.2	6.9	0.28	5.2	8.0	6.9	0.28	4.9
NGC4555	Hernq.	58.2	6.2	0.36	7.6	19.5	6.2	0.32	7.0
	pIso	1.8	7.6	0.27	2.3	0.6	7.7	0.31	2.2

Table 5.4: Results of the best-fitting parameters for the XMM data. We show the results for both the prolate and oblate configurations for each mass profile. The reduced-χ^2 is also provided and all fits have 37 degrees of freedom.

		XMM							
		Prolate				Oblate			
Galaxy	Profile	a_s (")	Γ	ϵ	χ^2_{red}	a_s (")	Γ	ϵ	χ^2_{red}
	NFW	46.3	8.0	0.21	7.9	16.6	7.9	0.23	7.8
NGC6482	Hernq.	102.9	7.2	0.22	10.6	40.0	7.2	0.26	11.0
	pIso	5.6	7.6	0.2	6.6	2.2	7.6	0.23	6.4
	NFW	52.0	7.6	0.23	4.4	20.6	7.8	0.25	4.2
NGC7785	Hernq.	194.4	9.8	0.17	2.0	47.9	7.5	0.18	3.1
	pIso	29.8	9.7	0.16	1.2	7.3	7.8	0.21	1.8
	NFW	47.9	7.3	0.45	3.0	22.9	8.0	0.43	3.6
NGC7796	Hernq.	107.4	6.7	0.42	3.6	40.9	6.6	0.44	3.6
	pIso	4.8	6.6	0.42	2.7	5.9	7.6	0.32	7.4
	NFW	36.8	8.2	0.27	3.2	11.3	7.7	0.24	2.9
NGC953	Hernq.	73.4	7.6	0.22	3.9	28.0	7.6	0.29	4.0
	pIso	3.8	7.4	0.25	2.9	1.4	7.4	0.24	2.8
	NFW	79.1	7.6	0.34	8.9	30.7	7.6	0.35	8.4
NGC720	Hernq.	126.7	6.4	0.26	12.2	60.0	6.7	0.33	9.5
	pIso	13.2	6.5	0.3	10.7	4.6	6.6	0.34	9.9

Table 5.5: Results of the best-fitting parameters for the XMM data. We show the results for both the prolate and oblate configurations for each mass profile. The reduced-χ^2 is also provided and all fits have 37 degrees of freedom.

		Chandra							
		Prolate				Oblate			
Galaxy	Profile	a_s (")	Γ	ϵ	χ^2_{red}	a_s (")	Γ	ϵ	χ^2_{red}
	NFW	24.0	7.8	0.34	8.3	24.5	7.9	0.35	8.2
IC4451	Hernq.	49.7	7.0	0.31	9.8	45.8	6.8	0.34	9.6
	pIso	4.0	6.6	0.32	10.2	4.8	7.4	0.26	14.1
	NFW	22.4	7.9	0.43	13.1	21.7	8.0	0.44	12.7
NGC1521	Hernq.	41.2	6.8	0.44	14.3	40.8	6.9	0.46	13.7
	pIso	3.4	6.6	0.42	14.0	2.7	6.9	0.49	13.6
	NFW	30.3	7.4	0.48	1.3	29.0	7.6	0.5	1.2
NGC4125	Hernq.	48.8	6.2	0.48	1.3	49.6	6.3	0.51	1.3
	pIso	4.4	6.2	0.48	1.3	4.2	6.3	0.52	1.2
	NFW	9.5	6.9	0.28	5.2	8.0	6.9	0.28	4.9
NGC4555	Hernq.	22.9	6.2	0.36	7.6	19.5	6.2	0.32	7.0
	pIso	0.7	7.6	0.27	2.3	0.6	7.7	0.31	2.2
	NFW	10.1	8.5	0.2	1.0	10.0	8.4	0.21	0.9
NGC57	Hernq.	22.6	7.8	0.2	1.2	22.0	7.6	0.22	1.2
	pIso	1.5	8.0	0.2	1.0	1.3	7.7	0.27	1.3

Table 5.6: Results of the best-fitting parameters for the Chandra data. We show the results for both the prolate and oblate configurations for each mass profile. The reduced-χ^2 is also provided and all fits have 37 degrees of freedom.

		Chandra							
		Prolate				Oblate			
Galaxy	Profile	a_s (")	Γ	ϵ	χ^2_{red}	a_s (")	Γ	ϵ	χ^2_{red}
	NFW	18.2	8.0	0.21	7.9	16.6	7.9	0.23	7.8
NGC6482	Hernq.	40.5	7.2	0.22	10.6	40.0	7.2	0.26	11.0
	pIso	2.2	7.6	0.2	6.6	2.2	7.6	0.23	6.4
	NFW	18.9	7.3	0.45	3.0	22.9	8.0	0.43	3.6
NGC7796	Hernq.	42.3	6.7	0.42	3.6	40.9	6.6	0.44	3.6
	pIso	1.9	6.6	0.42	2.7	5.9	7.6	0.32	7.4
	NFW	14.5	8.2	0.27	3.2	11.3	7.7	0.24	2.9
NGC953	Hernq.	28.9	7.6	0.22	3.9	28.0	7.6	0.29	4.0
	pIso	1.5	7.4	0.25	2.9	1.4	7.4	0.24	2.8
	NFW	31.1	7.6	0.34	8.9	30.7	7.6	0.35	8.4
NGC720	Hernq.	49.9	6.4	0.26	12.2	60.0	6.7	0.33	9.5
	pIso	5.2	6.5	0.3	10.7	4.6	6.6	0.34	9.9

Table 5.7: (Cont.) Results of the best-fitting parameters for the Chandra data. We show the results for both the prolate and oblate configurations for each mass profile. The reduced-χ^2 is also provided and all fits have 37 degrees of freedom.

5.5.1 Implications for the Cross-section of Dark Matter Interactions

In line with early analytic arguments concerning SIDM [284], simulations have demonstrated that the DM self-interactions produce halos with greater sphericity than in CDM [254, 115]. In Ref. [254], DM halos were simulated for cross-sections of $\sigma/m = 0$ cm^2/g (CDM), 0.1 cm^2/g, and 1 cm^2/g. These simulations were originally motivated by the results of the NGC 720 study [81], and therefore use halos models based on NGC 720 with a mass range of $(3 - 10) \times 10^{12} M_\odot$ and ellipticities calculated within 8.5 kpc $< r <$ 14 kpc (roughly corresponding to $2.7 r_e < r < 4.5 r_e$ based on the effective radius given in table 5.1). The resulting ellipticities of the simulated halos were then compared with the observed ellipticities of NGC 720 [81]. It was found that the NGC 720 DM halo ellipticity ($\epsilon \approx 0.35 - 0.4$) was consistent with both the CDM and 0.1 cm^2/g interaction regimes (cf. Figure 8 of [254]). However the distribution in ellipticity of the simulated halos exhibited considerable scatter, making concrete conclusions based on the one observed galaxy difficult. With the supplement provided in this analysis we can consider a similar comparison, though now with a sample of galaxies rather than the singular case of NGC 720 from Ref. [81]. In figure 5.9 we show the normalized distribution of halo ellipticities of our sample for an NFW profile overlaid with the results of the simulations from [254]. Here it can be seen the halo ellipticities of our sample are consistent with some non-negligible DM interactions. Particularly for the Chandra data, the distribution of ellipticities is in strong agreement with $\sigma/m = 0.1$ cm^2/g, and the Buote et. al. (2002) [81] analysis of NGC 720 aligns close to the peak of the distribution. The ellipticities taken from the XMM data tend toward lower ellipticities, though also having more greater spread and essentially overlapping to some degree the histogram for each

interaction strength. This may to some extent be attributable to the larger PSF of XMM producing a somewhat more "smoothed" image compared to the Chandra data, although further investigation would be needed to determine whether this is a meaningful effect. The sample of measured ellipticities can be applied to comparisons between additional existing and future halo simulations, as well as for placing direct constraints on SIDM models.

5.6 Conclusions

In this analysis we have studied a sample of isolated elliptical galaxies as a probe of the dark matter halo shape. Using data from the XMM-Newton and Chandra telescopes we analyzed the X-ray surface brightness and ellipticity profiles of 11 elliptical galaxies. By selecting galaxies that meet the criteria of being relaxed, isolated, and approximately isothermal, we made the assumption that these galaxies were in hydrostatic equilibrium with the gravitational potential. Under this assumption we showed the relation between the shape of the 3D matter distribution and the 2D projected X-ray image, which allowed us to model the 3D matter distribution and fit to the data, thereby determining the underlying shape for the assumed matter distribution.

We considered three separate spheroidal mass distributions including an NFW, Hernquist, and pseudo-isothermal profile. Additionally, we considered both prolate and oblate configurations for each profile, effectively bracketing the range of triaxial models. The best fitting ellipticities did not appear to have a significant relation to the profile.

For most of the galaxies in the sample the ellipticities fell roughly within the range of $\epsilon \approx 0.2 - 0.5$. Comparing the measured ellipticities with simulations of DM halos that have varying degrees of self-interactions shows consistency with

interaction cross-sections of $\sigma/m = 0.1$ cm^2/g. However, the simulations of Ref. [254] used for this comparison reported significant scatter. This is also apparent in our observational results, and the ellipticity distribution also overlaps significantly with the distribution for CDM halos. We note that these findings are highly consistent with the comparison between the simulations and the ellipticity analysis of NGC 720 performed in Ref. [81].

In section 5.5 we discuss how the choice of radial range over which the ellipticity fitting procedure was performed could be modified, noting that there may be a better motivated range to fit. Specifically, we note that the inner regions likely have non-negligible influence from stellar components of the mass and that these regions are also more susceptible to point source removal and replacement. At larger radii we discuss that there are effects that appear to be largely instrumental, and that removing the large radii regimes is appropriate. Also, the comparison with simulations is more applicable when similar radial regimes are being compared. In future aspects of this work we plan to implement a more selective and well-motivated fit range.

While the work of Ref. [81] and subsequent studies have shown that X-ray shapes of elliptical galaxies can have powerful constraining ability on SIDM, the results presented now allow for a comparison using a statistical meaningful sample. For specific models, direct constraints can be determined (see for example [222, 141, 12]), while our sample also provides for detailed comparison with simulations that contain only DM as well as future simulations that also seek to incorporate baryonic effects.
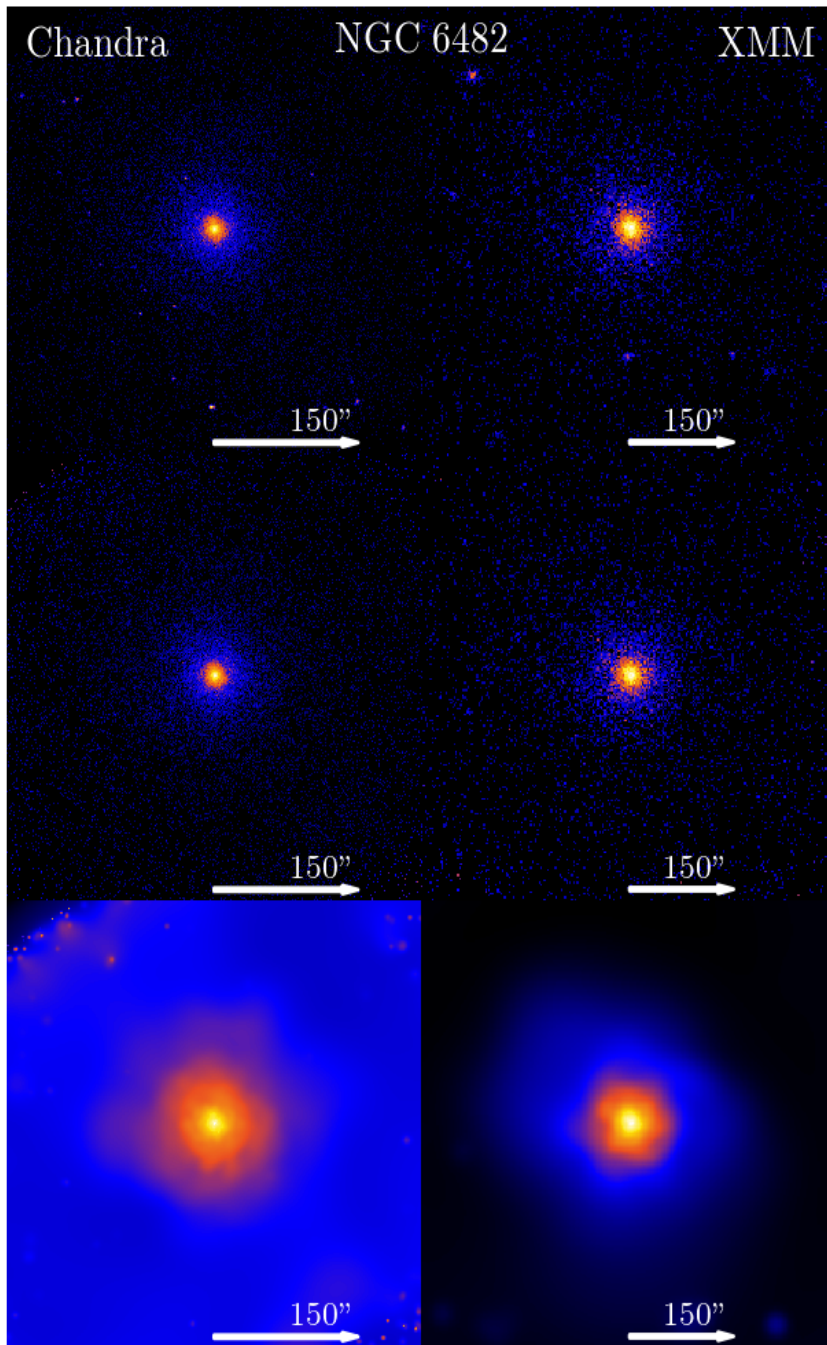
Figure 5.3: Chandra (left column) and XMM-Newton (right column) images of NGC6482. The top row is prior to point source detection. The middle row is after running the `wavdetect` and `dmfilth` routines to remove points sources. Finally, the bottom row shows the point source cleaned, smoothed, and exposure corrected images.
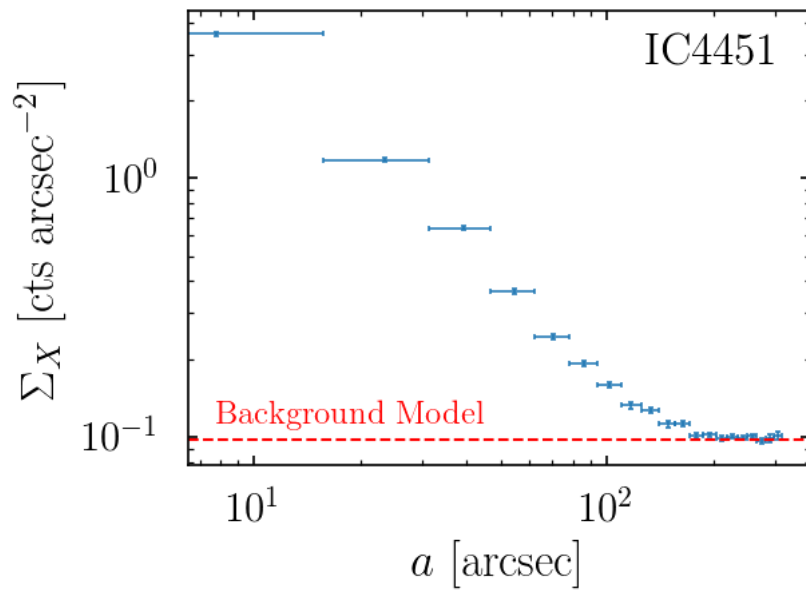
Figure 5.4: Surface brightness profile of IC 4451 without background subtraction. The red line shows the background model used in later portions of the analysis.
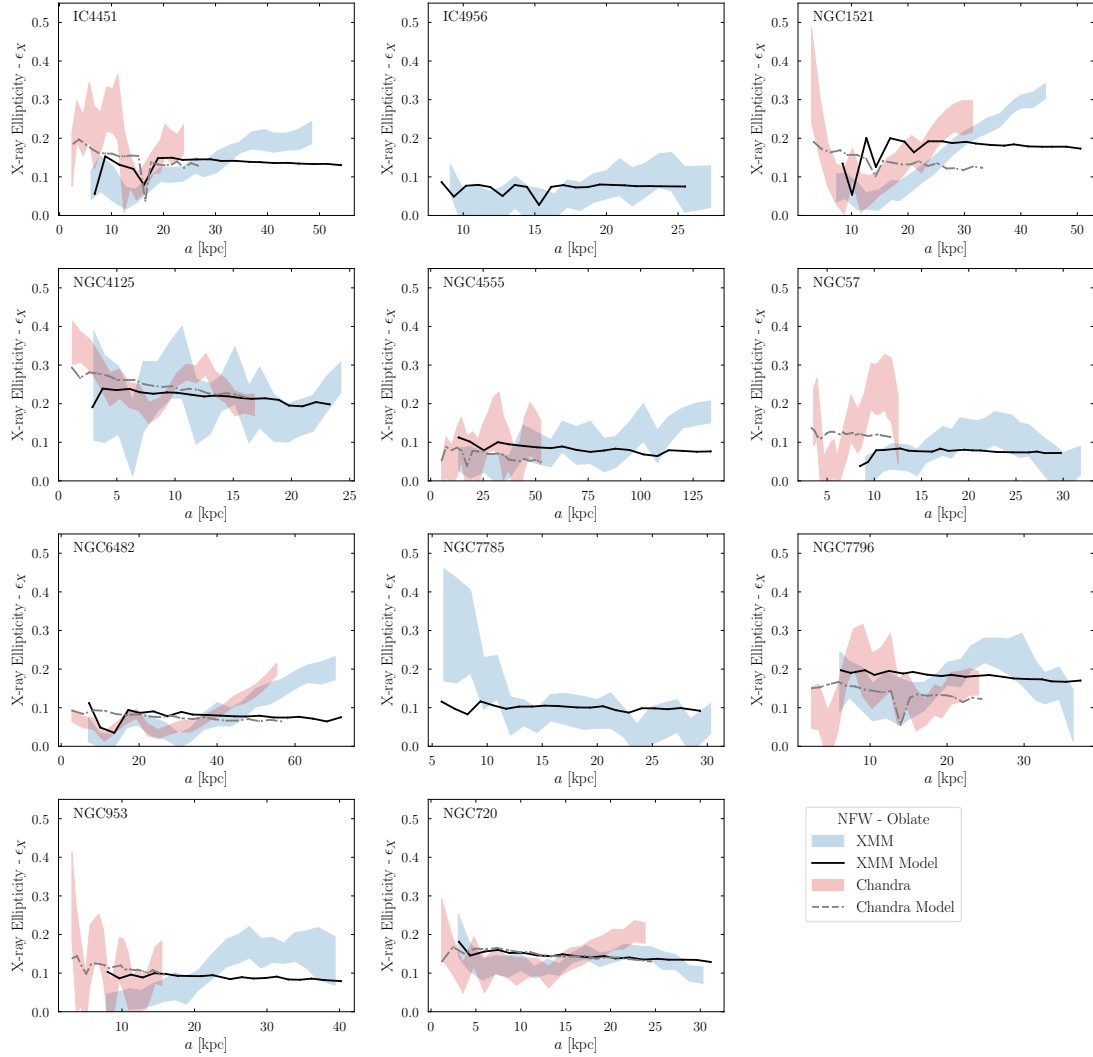
Figure 5.5: Ellipticity profiles of the best-fit models for each galaxy assuming an oblate NFW mass distribution plotted along with the profiles from the observational data.
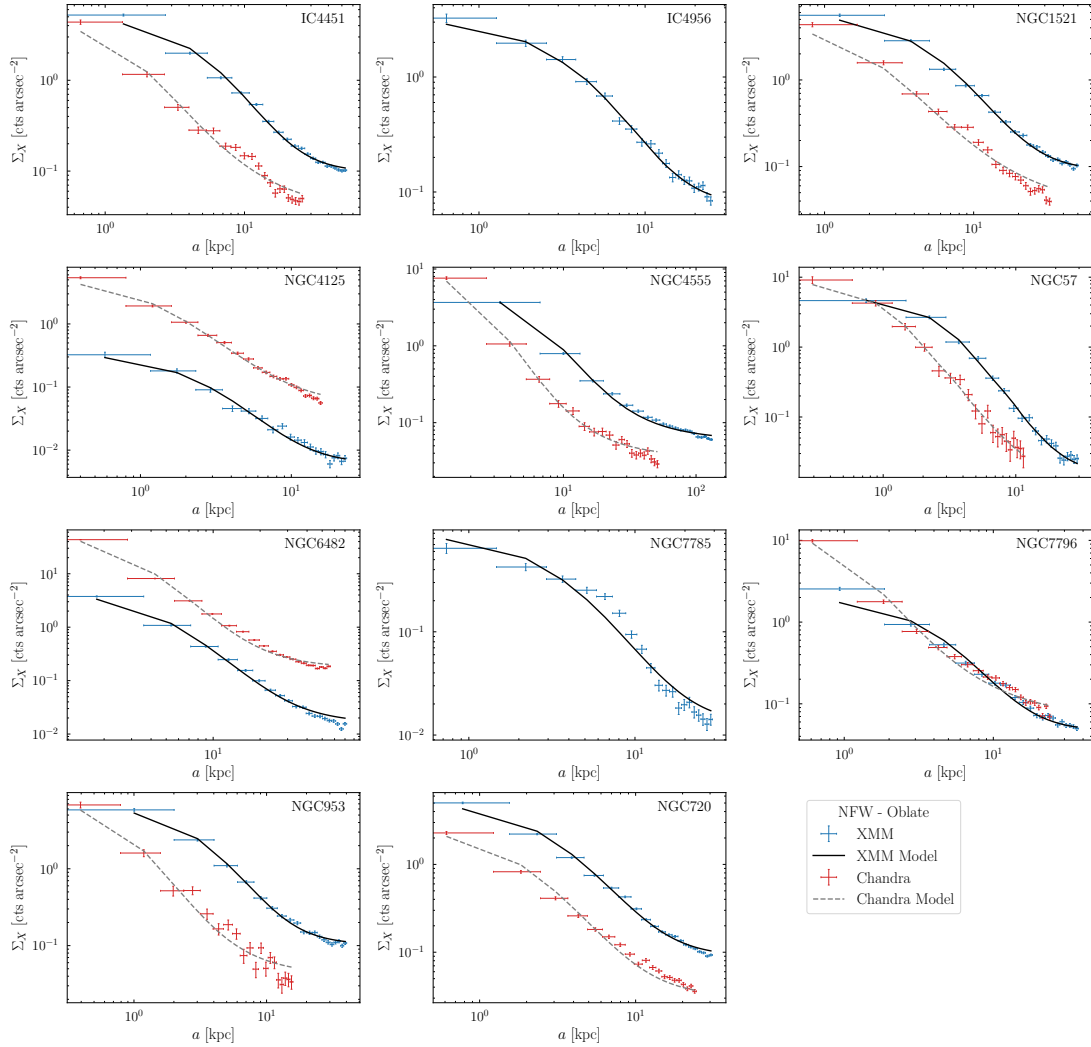
Figure 5.6: Surface brightness profiles of the best-fit models for each galaxy assuming an oblate NFW mass distribution plotted along with the profiles from the observational data.
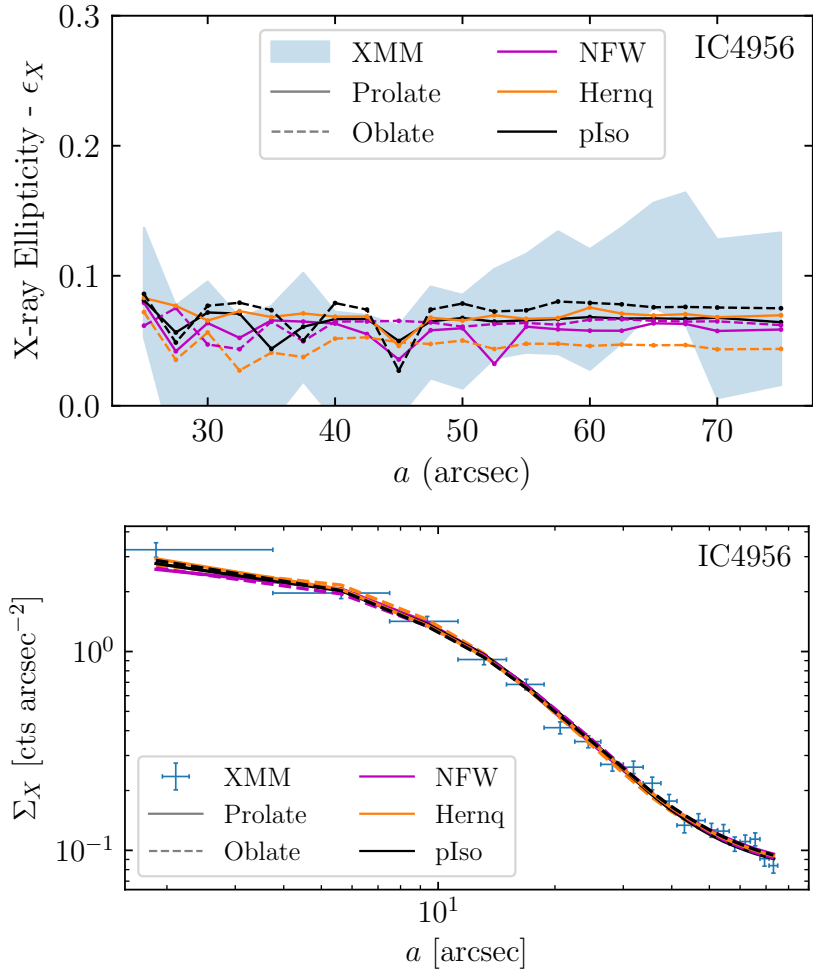
Figure 5.7: Best-fit ellipticity and surface brightness profiles for the XMM observations of IC4956. Here we show the best fitting profiles for each mass distribution configuration. Colors correspond to different profiles, while the solid and dashed lines refer to to the prolate and oblate configurations respectively.
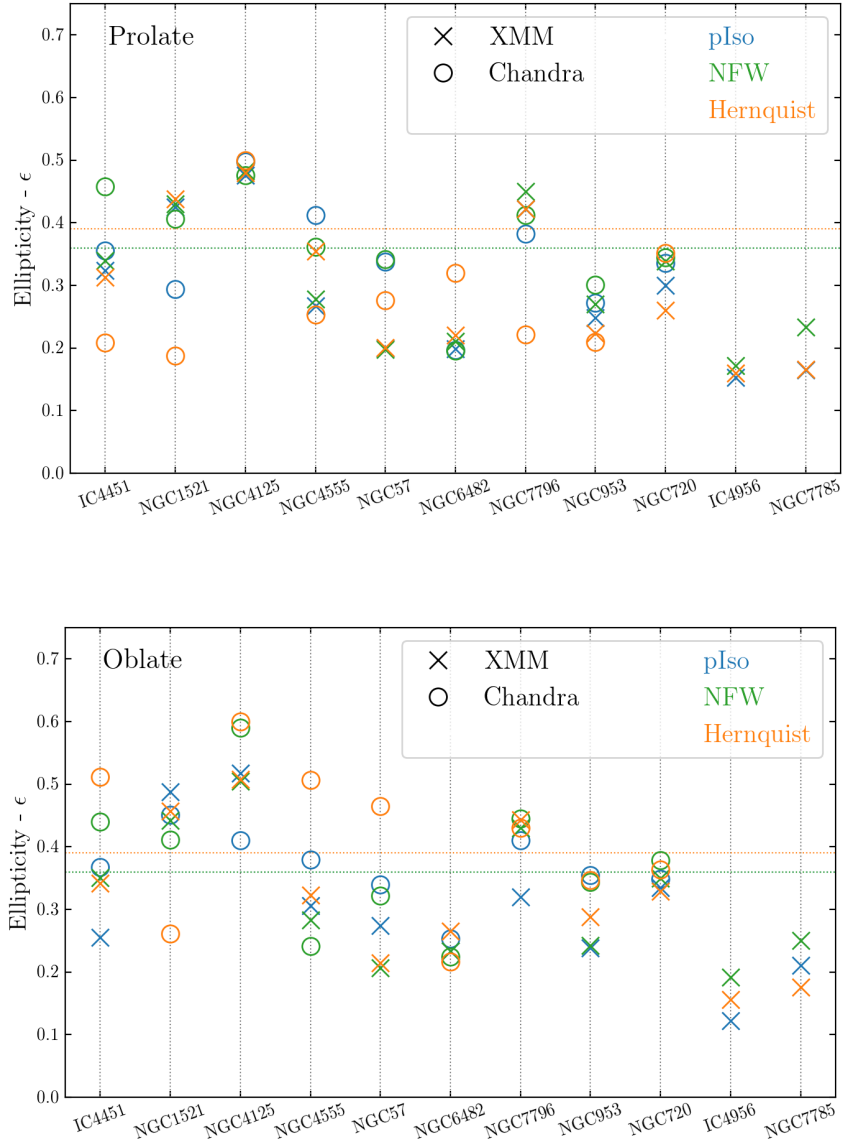
Figure 5.8: Best-fit DM halo ellipticities ϵ for each galaxy in our sample determined from the XMM (X's) and Chandra (circles) observations. The top panel shows the prolate configuration, while in the bottom panel we show the oblate configuration. The horizontal lines show the values found for NGC720 in [81] (Note that in the prolate configuration the ellipticities for the $\rho \sim a^{-2}$ and NFW halos are overlapping.)
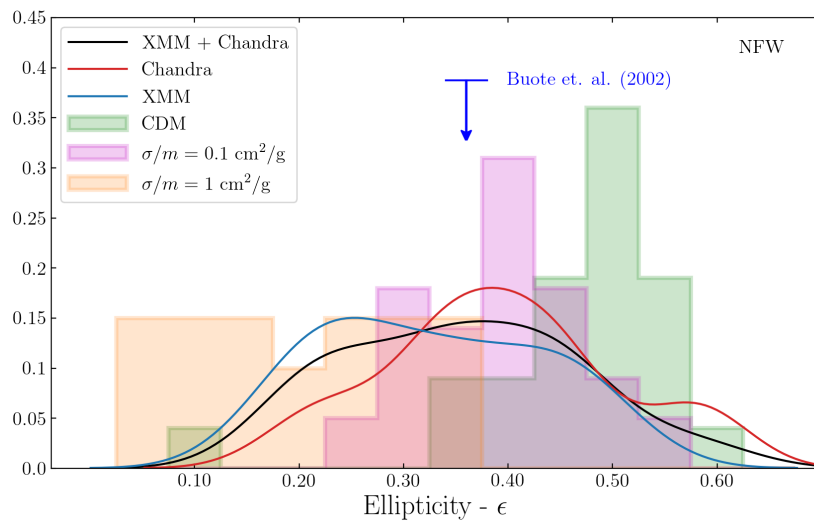
Figure 5.9: Normalized distributions of the best fit galaxy ellipticities from the Chandra (red) and XMM (blue) data for an NFW profile, as well as the combined distribution (black). The histograms show the simulated ellipticities for various interaction cross sections from Figure 8 of [254]. We also show for reference the best-fit model and errors for the analysis of NGC 720 preformed in Ref. [81].

Chapter 6

Conclusion

The nature of dark matter remains an open and perplexing question in astroparticle physics despite the significant progress made in theoretical descriptions and observational methods. However, there is much to be excited about going forward, with development of new DM models and increasingly advanced search techniques across collider, direct detection, and indirect detection approaches. Each of these techniques has shown great promise in strengthening DM constraints and potentially discovering smoking gun signals of DM.

Indirect detection searches in particular play a critical role in our current and future knowledge of DM, and offer various complementary multi-messenger and multiwavelength probes. Specifically, multiwavelength observations of annihilating DM are a promising avenue to constrain well-motivated DM models. In chapter 2 we presented the RX-DMFIT tool, which we developed to allow for the computation of multi-wavelength emission from DM annihilation while incorporating complex astrophysical effects such as diffusion and radiative losses. While gamma-ray observations have provided some of the best indirect observations, utilizing the full emission spectrum in a variety of astrophysical systems will be a powerful technique in future efforts to identify DM.

This work is particularly timely as the future of multiwavelength indirect DM searches is bright. First, new targets for indirect searches are currently being identified. In recent years the number of discovered dwarf galaxies has increased thanks to the Dark Energy Survey (DES), and this trend is expected to continue as the upcoming Vera C. Rubin Observatory (formerly Large Synoptic Survey Telescope (LSST)) aims to begin observing in the 2020's [129]. Meanwhile, additional targets for DM indirect detection such as low surface brightness galaxies [46] and globular clusters [68] have also been drawing attention as potential targets for multiwavelength DM searches that have yet to be fully exploited.

Beyond simply identifying more targets, new and upcoming facilities will provide drastic increases in our ability to constrain DM across the electromagnetic spectrum. Radio observations are particularly exciting as a new generation of radio telescopes emerges. The planned Square Kilometer Array (SKA) offers major improvements over current radio capabilities and is predicted to greatly strengthen constraints on annihilating and decaying DM [293, 194, 96, 88]. Currently, precursors and pathfinders of SKA are already making contributions to radio probes of DM [109, 319]. In X-ray energy bands, next-generation facilities may be able to contribute meaningful complementary constraints to DM searches [326]. This is especially true in regards to X-ray line searches from decaying DM [245], as well as potentially for constraints from the inverse compton X-ray emission arising from the $e^{\pm}$ annihilation and decay products, which has previously not been as competitive with radio and gamma-ray searches [190]. Upcoming gamma-ray instruments are also likely to contribute to our understanding of DM and its multiwavelength signatures. Proposed MeV telescopes such as e-Astrogam [117] and AMEGO [223] can provide the capability of studying the emission spectrum in the relatively poorly explored MeV regime. In addition to important astrophysical

phenomena in this regime, the MeV band is also of relevance to many light DM models [89, 270, 108]. At the higher gamma-ray energies, the Cherenkov Telescope Array will be at the forefront of capabilities for DM searches with gamma-rays greater $\gtrsim 1$ TeV [235].

One of the most actively studied DM search targets for indirect detection has been the Milky Way Galactic Center, gaining much attention due in part to observed gamma-ray emission consistent with annihilating WIMP DM. The recent observation of somewhat similar gamma-ray emission in M31 adds to the intrigue. However, a DM annihilation origin for the emission would also have signatures at other wavelengths. We were among the first groups to study the full multiwavelength spectrum in the context of DM annihilation, comparing both whether GCE DM models could account for the observed emission in M31, and whether models that can reproduce the gamma-ray emission are consistent with observations at other wavelengths. The results of this work presented in chapter 3 show that GCE DM models produce spectra in tension with the observed M31 emission. Fitting the gamma-ray emission required lower masses than the GCE models and also produces radio spectra that does not match radio observations, and in some cases led to overproduction of the radio emission.

In order to better understand the role that DM might play in the multi wavelength emission of M31, it is critical to also consider the role astrophysical phenomena play. Non-DM sources of the GCE have been explored extensively, and many possible explanations proposed could also potentially account for the M31 emission. MSPs, and cosmic-rays provide intriguing explanations. Studies of MSPs have shown that while the energetics can be fit, the total pulsar luminosity expected in M31 is not sufficient to account for the Fermi observation. An injection of cosmic-rays is also a possibility to explain the observed emission and

– as in the DM scenario – would exhibit a distinct multi-wavelength spectrum. Exploring this possibility in chapter 4, we found several CR models that had energetics consistent with the observed multi-wavelength spectrum and astrophysical parameters in reasonable ranges with respect to other measurements. However, a persistent problem with these cosmic-ray models was that the power output from SNe and pulsars required to produce the emission was consistently higher than expected for M31.

Understanding the origin of the emission in M31 will continue to be a challenge with significant implications for DM. Meaningful data will come from a variety of venues, including a better understanding of the GCE, as well as more in depth studies of the DM distribution in M31 and the gamma-ray signal. Particularly, observations of the gamma-ray emission throughout larger regions of the galaxy can shed light on a potential DM annihilation signal, as well as observations with higher energy gamma-ray instruments such as HAWC [196, 18]. Additionally, more sophisticated modeling of the cosmic ray production and transport in M31 will likely prove useful in disentangling the multi-wavelength emission produced by DM from that of astrophysical origins.

Despite the extensive research efforts to search for WIMP DM across collider, direct detection, and indirect detection studies, the lack of a convincing detection and increasingly robust constraints makes non-WIMP DM models appealing. Self-interacting dark matter models are a particularly interesting class of candidates, as they can potentially resolve some of the small-scale challenges of the ΛCDM framework.

One way to probe SIDM interaction strengths is by studying the shapes of DM halos, as SIDM tends to produce more spherical halos than CDM. In chapter 5 we presented our analysis of X-ray ellipticity measurements as a probe of the DM

halo shape in elliptical galaxies. Comparisons between the measured ellipticities we found and the shapes of simulated SIDM halos showed consistency with some interactions cross section $\sigma/m \lesssim 1 \text{ cm}^2/\text{g}$ as well as with CDM. While many SIDM studies focus on dwarf or cluster scale halos, our measurements provide greater insights into the role of SIDM in halos with $M \approx 10^{12} - 10^{13} M_\odot$. However, it is important to keep in mind that the simulations are performed assuming DM only, and the effects of baryonic matter can potentially have significant effects that may be revealed in more realistic simulations at this halo mass scale. Additional advances in understanding potential DM self-interactions will be aided by the dwarf discovery space of DES and the Rubin Observatory that will be able to identify and study the properties of nearby low mass and faint DM halos [129]. Ultimately, constraints on SIDM will require several complementary probes at various halo mass scales in order to constrain both the absolute magnitude of DM self interactions, as well as their velocity dependence.

Through the concerted efforts of theorists and experimentalists across particle physics, astrophysics, astronomy, and cosmology, there have been great strides made in developing and constraining the DM landscape. In the coming years and decades, theoretical and technological advancements will push the bounds of our understanding of DM even further towards a more complete and robust framework.

Bibliography

[1] Planck Collaboration a. Planck 2015 results. XIII. Cosmological parameters. A&A, 594:A13, September 2016.

[2] K. N. Abazajian, N. Canac, S. Horiuchi, and M. Kaplinghat. Astrophysical and dark matter interpretations of extended gamma-ray emission from the Galactic Center. Phys. Rev. D, 90(2):023526, July 2014.

[3] K. N. Abazajian and R. E. Keeley. Bright gamma-ray Galactic Center excess and dark dwarfs: Strong tension for dark matter annihilation despite Milky Way halo profile and diffuse emission uncertainties. Phys. Rev. D, 93(8):083514, April 2016.

[4] A. A. Abdo et al. Fermi Large Area Telescope observations of Local Group galaxies: detection of M 31 and search for M 33. A&A, 523:L2, November 2010.

[5] A. Abramowski et al. Search for a Dark Matter Annihilation Signal from the Galactic Center Halo with H.E.S.S. *Physical Review Letters*, 106(16):161301, April 2011.

[6] A. Abramowski et al. Search for dark matter annihilation signatures in H.E.S.S. observations of dwarf spheroidal galaxies. Phys. Rev. D, 90(11):112012, December 2014.

[7] M. Ackermann et al. Constraints on dark matter annihilation in clusters of galaxies with the Fermi large area telescope. J. Cosmology Astropart. Phys., 5:025, May 2010.

[8] M. Ackermann et al. Detection of the Characteristic Pion-Decay Signature in Supernova Remnants. *Science*, 339:807–811, February 2013.

[9] M. Ackermann et al. Searching for Dark Matter Annihilation from Milky Way Dwarf Spheroidal Galaxies with Six Years of Fermi Large Area Telescope Data. *Physical Review Letters*, 115(23):231301, December 2015.

[10] M. Ackermann et al. Observations of M31 and M33 with the Fermi Large Area Telescope: A Galactic Center Excess in Andromeda? ApJ, 836:208, February 2017.

[11] M. Ackermann et al. The Fermi Galactic Center GeV Excess and Implications for Dark Matter. ApJ, 840:43, May 2017.

[12] Prateek Agrawal, Francis-Yan Cyr-Racine, Lisa Randall, and Jakub Scholtz. Make dark matter charged again. J. Cosmology Astropart. Phys., 2017(5):022, May 2017.

[13] F. A. Aharonian, A. M. Atoyan, and H. J. Voelk. High energy electrons and positrons in cosmic rays as an indicator of the existence of a nearby cosmic tevatron. A&A, 294:L41–L44, February 1995.

[14] F. A. Aharonian et al. Search for TeV gamma ray emission from the Andromeda galaxy. A&A, 400:153–159, Mar 2003.

[15] M. Ajello et al. Fermi-LAT Observations of High-Energy Gamma-Ray Emission toward the Galactic Center. ApJ, 819(1):44, March 2016.

[16] D. S. Akerib et al. Results from a search for dark matter in the complete lux exposure. *Phys. Rev. Lett.*, 118:021303, Jan 2017.

[17] Shadab Alam et al. The clustering of galaxies in the completed SDSS-III Baryon Oscillation Spectroscopic Survey: cosmological analysis of the DR12 galaxy sample. MNRAS, 470(3):2617–2652, September 2017.

[18] A. Albert. Search for dark matter gamma-ray emission from the Andromeda Galaxy with the High-Altitude Water Cherenkov Observatory. J. Cosmology Astropart. Phys., 6:043, June 2018.

[19] N. C. Amorisco, J. Zavala, and T. J. L. de Boer. Dark Matter Cores in the Fornax and Sculptor Dwarf Galaxies: Joining Halo Assembly and Detailed Star Formation Histories. ApJ, 782(2):L39, February 2014.

[20] Kevin E. Andrade, Quinn Minor, Anna Nierenberg, and Manoj Kaplinghat. Detecting dark matter cores in galaxy clusters with strong lensing. MNRAS, 487(2):1905–1926, August 2019.

[21] Giorgio Arcadi, Maíra Dutra, Pradipta Ghosh, Manfred Lindner, Yann Mambrini, Mathias Pierre, Stefano Profumo, and Farinaldo S. Queiroz. The waning of the WIMP? A review of models, searches, and constraints. *European Physical Journal C*, 78(3):203, March 2018.

[22] W. B. Atwood et al. The Large Area Telescope on the Fermi Gamma-Ray Space Telescope Mission. ApJ, 697(2):1071–1102, June 2009.

[23] Horace W. Babcock. The rotation of the Andromeda Nebula. *Lick Observatory Bulletin*, 498:41–51, January 1939.

[24] E. A. Baltz and J. Edsjö. Positron propagation and fluxes from neutralino annihilation in the halo. Phys. Rev. D, 59(2):023511, January 1999.

[25] V. Barger, W. Y. Keung, D. Marfatia, and G. Shaughnessy. PAMELA and dark matter. *Physics Letters B*, 672(2):141–146, February 2009.

[26] R. Bartels, S. Krishnamurthy, and C. Weniger. Strong Support for the Millisecond Pulsar Origin of the Galactic Center GeV Excess. *Physical Review Letters*, 116(5):051102, February 2016.

[27] S. Baur. Dark Matter Searches with the IceCube Upgrade. In *36th International Cosmic Ray Conference (ICRC2019)*, volume 36 of *International Cosmic Ray Conference*, page 506, July 2019.

[28] G. Beck and S. Colafrancesco. A multi-frequency analysis of possible dark matter contributions to M31 gamma-ray emissions. *Journal of Cosmology and Astro-Particle Physics*, 2017:007, Oct 2017.

[29] R. Beck, E. M. Berkhuijsen, and P. Hoernes. A deep lambda 20 CM radio continuum survey of M 31. A&AS, 129:329–336, April 1998.

[30] R. Beck, E. M. Berkhuijsen, and R. Wielebinski. Distribution of polarised radio emission in M31. Nature, 283:272–275, January 1980.

[31] R. Beck and R. Graeve. The distribution of thermal and nonthermal radio continuum emission of M31. A&A, 105:192–199, January 1982.

[32] J. Bekenstein and M. Milgrom. Does the missing mass problem signal the breakdown of Newtonian gravity? ApJ, 286:7–14, November 1984.

[33] Jacob D. Bekenstein. Relativistic gravitation theory for the modified Newtonian dynamics paradigm. Phys. Rev. D, 70(8):083509, October 2004.

[34] A.R. Bell. Cosmic ray acceleration. *Astroparticle Physics*, 43:56 – 70, 2013. Seeing the High-Energy Universe with the Cherenkov Telescope Array - The Science Explored with the CTA.

[35] E. G. Berezhko. Origin of Galactic Cosmic Rays from Supernova Remnants. *Nuclear Physics B Proceedings Supplements*, 256:23–35, November 2014.

[36] L. Bergström. Non-baryonic dark matter: observational evidence and detection methods. *Reports on Progress in Physics*, 63:793–841, May 2000.

[37] L. Bergström. Dark matter evidence, particle physics candidates and detection methods. *Annalen der Physik*, 524:479–496, October 2012.

[38] E. M. Berkhuijsen, R. Beck, and P. Hoernes. The polarized disk in M 31 at lambda 6 cm. A&A, 398:937–948, February 2003.

[39] E. M. Berkhuijsen, R. Beck, and F. S. Tabatabaei. How cosmic ray electron propagation affects radio-far-infrared correlations in M 31 and M 33. MNRAS, 435:1598–1609, October 2013.

[40] E. M. Berkhuijsen, D. Mitra, and P. Mueller. Filling factors and scale heights of the diffuse ionized gas in the Milky Way. *Astronomische Nachrichten*, 327:82–96, January 2006.

[41] E. M. Berkhuijsen and P. Müller. Densities and filling factors of the diffuse ionized gas in the Solar neighbourhood. A&A, 490:179–187, October 2008.

[42] E. M. Berkhuijsen, R. Wielebinski, and R. Beck. A radio continuum survey of M31 at 4850 MHz. I - Observations - List of sources. A&A, 117:141–144, January 1983.

[43] G. Bertone, D. Hooper, and J. Silk. Particle dark matter: evidence, candidates and constraints. Phys. Rep., 405:279–390, January 2005.

[44] Gianfranco Bertone and Dan Hooper. History of dark matter. *Reviews of Modern Physics*, 90(4):045002, October 2018.

[45] M. Betoule et al. Improved cosmological constraints from a joint analysis of the SDSS-II and SNLS supernova samples. A&A, 568:A22, August 2014.

[46] Pooja Bhattacharjee, Pratik Majumdar, Mousumi Das, Subinoy Das, Sayan Biswas, and Partha S. Joarder. Multiwavelength analysis of low surface brightness galaxies to study probable dark matter signature. *arXiv e-prints*, page arXiv:1911.00369, November 2019.

[47] J. Binney and S. Tremaine. *Galactic Dynamics: Second Edition*. Princeton Series in Astrophysics. Princeton University Press, 2011.

[48] James Binney and Oliver Strimpel. Predicting the X-ray brightness distributions of cluster sources - 1. Estimating the potentials. MNRAS, 185:473–484, November 1978.

[49] R. Bird and VERITAS Collaboration. VERITAS Observations of M31 (the Andromeda Galaxy). In *34th International Cosmic Ray Conference (ICRC2015)*, volume 34, page 851, Jul 2015.

[50] P. Blasi and E. Amato. Escape of cosmic rays from the Galaxy and effects on the circumgalactic medium. *arXiv e-prints*, page arXiv:1901.03609, January 2019.

[51] P. Blasi and S. Colafrancesco. Cosmic rays, radio halos and nonthermal X-ray emission in clusters of galaxies. *Astroparticle Physics*, 12:169–183, November 1999.

[52] Pasquale Blasi and Elena Amato. Diffusive propagation of cosmic rays from supernova remnants in the Galaxy. I: spectrum and chemical composition. *Journal of Cosmology and Astro-Particle Physics*, 2012:010, January 2012.

[53] Jan J. Blom, Timothy A. D. Paglione, and Alberto Carramiñana. Diffuse Gamma-Ray Emission from Starburst Galaxies and M31. ApJ, 516:744–749, May 1999.

[54] G. R. Blumenthal, S. M. Faber, R. Flores, and J. R. Primack. Contraction of dark matter galactic halos due to baryonic infall. ApJ, 301:27–34, February 1986.

[55] G. R. Blumenthal, S. M. Faber, J. R. Primack, and M. J. Rees. Formation of galaxies and large-scale structure with cold dark matter. Nature, 311:517–525, October 1984.

[56] G. R. Blumenthal and R. J. Gould. Bremsstrahlung, Synchrotron Radiation, and Compton Scattering of High-Energy Electrons Traversing Dilute Gases. *Reviews of Modern Physics*, 42:237–271, 1970.

[57] Paul Bode, Jeremiah P. Ostriker, and Neil Turok. Halo Formation in Warm Dark Matter Models. ApJ, 556(1):93–107, July 2001.

[58] A. Bonafede, L. Feretti, M. Murgia, F. Govoni, G. Giovannini, D. Dallacasa, K. Dolag, and G. B. Taylor. The Coma cluster magnetic field from Faraday rotation measures. A&A, 513:A30, April 2010.

[59] M. T. Botticella, S. J. Smartt, R. C. Kennicutt, E. Cappellaro, M. Sereno, and J. C. Lee. A comparison between star formation rate diagnostics and rate of core collapse supernovae within 11 Mpc. A&A, 537:A132, Jan 2012.

[60] Antonio Boveia and Caterina Doglioni. Dark Matter Searches at Colliders. *Annual Review of Nuclear and Particle Science*, 68:429–459, October 2018.

[61] A. Boyarsky, D. Iakubovskyi, O. Ruchayskiy, and V. Savchenko. Constraints on decaying dark matter from XMM-Newton observations of M31. MNRAS, 387:1361–1373, July 2008.

[62] Michael Boylan-Kolchin, James S. Bullock, and Manoj Kaplinghat. Too big to fail? The puzzling darkness of massive Milky Way subhaloes. MNRAS, 415(1):L40–L44, July 2011.

[63] Michael Boylan-Kolchin, James S. Bullock, and Manoj Kaplinghat. The Milky Way's bright satellites as an apparent failure of ΛCDM. MNRAS, 422(2):1203–1218, May 2012.

[64] T. D. Brandt and B. Kocsis. Disrupted Globular Clusters Can Explain the Galactic Center Gamma-Ray Excess. ApJ, 812:15, October 2015.

[65] Fabrizio Brighenti and William G. Mathews. X-Ray Observations and the Structure of Elliptical Galaxies. ApJ, 486(2):L83–L86, September 1997.

[66] Alyson Brooks. Re-examining astrophysical constraints on the dark matter model. *Annalen der Physik*, 264(7-8):294–308, August 2014.

[67] Alyson M. Brooks and Adi Zolotov. Why Baryons Matter: The Kinematics of Dwarf Spheroidal Satellites. ApJ, 786(2):87, May 2014.

[68] Anthony M. Brown, Thomas Lacroix, Sheridan Lloyd, Céline BÅ'hm, and Paula Chadwick. Understanding the γ-ray emission from the globular cluster 47 Tuc: Evidence for dark matter? Phys. Rev. D, 98(4):041301, August 2018.

[69] G. Brunetti, P. Blasi, O. Reimer, L. Rudnick, A. Bonafede, and S. Brown. Probing the origin of giant radio haloes through radio and γ-ray data: the case of the Coma cluster. MNRAS, 426:956–968, October 2012.

[70] J. Buch, M. Cirelli, G. Giesen, and M. Taoso. PPPC 4 DM secondary: a Poor Particle Physicist Cookbook for secondary radiation from Dark Matter. J. Cosmology Astropart. Phys., 9:037, September 2015.

[71] Matthew R. Buckley and Patrick J. Fox. Dark matter self-interactions and light force carriers. Phys. Rev. D, 81(8):083522, April 2010.

[72] James S. Bullock and Michael Boylan-Kolchin. Small-Scale Challenges to the ΛCDM Paradigm. ARA&A, 55(1):343–387, August 2017.

[73] David A. Buote. The Unusually High Halo Concentration of the Fossil Group NGC 6482: Evidence for Weak Adiabatic Contraction. ApJ, 834(2):164, January 2017.

[74] David A. Buote and Claude R. Canizares. X-Ray Constraints on the Shape of the Dark Matter in Five Abell Clusters. ApJ, 400:385, December 1992.

[75] David A. Buote and Claude R. Canizares. Geometrical Evidence for Dark Matter: X-Ray Constraints on the Mass of the Elliptical Galaxy NGC 720. ApJ, 427:86, May 1994.

[76] David A. Buote and Claude R. Canizares. The Twisting X-Ray Isophotes of the Elliptical Galaxy NGC 720. ApJ, 468:184, September 1996.

[77] David A. Buote and Claude R. Canizares. X-Ray Constraints on the Intrinsic Shape of the Lenticular Galaxy NGC 1332. ApJ, 457:177, January 1996.

[78] David A. Buote and Claude R. Canizares. X-ray isophote shapes and the mass of NGC 3923. MNRAS, 298(3):811–823, August 1998.

[79] David A. Buote and Philip J. Humphrey. *Dark Matter in Elliptical Galaxies*, volume 378 of *Astrophysics and Space Science Library*. 2012.

[80] David A. Buote and Philip J. Humphrey. Spherically averaging ellipsoidal galaxy clusters in X-ray and Sunyaev-Zel'dovich studies - II. Biases. MN-RAS, 421(2):1399–1420, April 2012.

[81] David A. Buote, Tesla E. Jeltema, Claude R. Canizares, and Gordon P. Garmire. Chandra Evidence of a Flattened, Triaxial Dark Matter Halo in the Elliptical Galaxy NGC 720. ApJ, 577(1):183–196, September 2002.

[82] J. O. Burns, E. J. Hallman, B. Gantner, P. M. Motl, and M. L. Norman. Why Do Only Some Galaxy Clusters Have Cool Cores? ApJ, 675:1125–1140, March 2008.

[83] F. Calore, I. Cholis, C. McCabe, and C. Weniger. A tale of tails: Dark matter interpretations of the Fermi GeV excess in light of background model systematics. Phys. Rev. D, 91(6):063003, March 2015.

[84] Francesca Calore, Ilias Cholis, and Christoph Weniger. Background model systematics for the Fermi GeV excess. J. Cosmology Astropart. Phys., 2015(3):038, March 2015.

[85] N. Cappelluti, Y. Li, A. Ricarte, B. Agarwal, V. Allevato, T. Tasnim Ananna, M. Ajello, F. Civano, A. Comastri, M. Elvis, A. Finoguenov, R. Gilli, G. Hasinger, S. Marchesi, P. Natarajan, F. Pacucci, E. Treister, and C. M. Urry. The Chandra COSMOS Legacy Survey: Energy Spectrum of the Cosmic X-Ray Background and Constraints on Undetected Populations. ApJ, 837:19, March 2017.

[86] D. Caprioli, E. Amato, and P. Blasi. The contribution of supernova remnants to the galactic cosmic ray spectrum. *Astroparticle Physics*, 33:160–168, April 2010.

[87] Damiano Caprioli. Understanding hadronic gamma-ray emission from supernova remnants. *Journal of Cosmology and Astro-Particle Physics*, 2011:026, May 2011.

[88] Andrea Caputo, Carlos Peña Garay, and Samuel J. Witte. Looking for axion dark matter in dwarf spheroidal galaxies. Phys. Rev. D, 98(8):083024, October 2018.

[89] Regina Caputo, Tim Linden, John Tomsick, Chanda Prescod-Weinstein, Manuel Meyer, Carolyn Kierans, Zorawar Wadiasingh, J. Patrick Harding, and Joachim Kopp. Looking Under a Better Lamppost: MeV-scale Dark Matter Candidates. **??***jnlBAAS*, 51(3):78, May 2019.

[90] C. L. Carilli and G. B. Taylor. Cluster Magnetic Fields. ARA&A, 40:319–348, 2002.

[91] E. Carlson, S. Profumo, and T. Linden. Cosmic-Ray Injection from Star-Forming Regions. *Physical Review Letters*, 117(11):111101, September 2016.

[92] D. Carter and N. Metcalfe. The morphology of clusters of galaxies. MNRAS, 191:325–337, May 1980.

[93] Gamil Cassam-Chenaï, John P. Hughes, Jean Ballet, and Anne Decourchelle. The Blast Wave of Tycho's Supernova Remnant. ApJ, 665:315–340, August 2007.

[94] K. W. Cavagnolo, B. R. McNamara, P. E. J. Nulsen, C. L. Carilli, C. Jones, and L. Bîrzan. A Relationship Between AGN Jet Power and Radio Power. ApJ, 720(2):1066–1072, September 2010.

[95] A. Cavaliere and R. Fusco-Femiano. X-rays from hot plasma in clusters of galaxies. A&A, 49:137–144, May 1976.

[96] Jose A. R. Cembranos, Álvaro de la Cruz-Dombriz, Viviana Gammaldi, and Miguel Méndez-Isla. SKA-Phase 1 sensitivity to synchrotron radio emission from multi-TeV Dark Matter candidates. *Physics of the Dark Universe*, 27:100448, January 2020.

[97] M. H. Chan. Revisiting the constraints on annihilating dark matter by the radio observational data of M31. Phys. Rev. D, 94(2):023507, July 2016.

[98] E. Charles et al. Sensitivity projections for dark matter searches with the Fermi large area telescope. Phys. Rep., 636:1–46, June 2016.

[99] Y. Chen, T. H. Reiprich, H. Böhringer, Y. Ikebe, and Y.-Y. Zhang. Statistics of X-ray observables for the cooling-core and non-cooling core galaxy clusters. A&A, 466:805–812, May 2007.

[100] I. Cholis, C. Evoli, F. Calore, T. Linden, C. Weniger, and D. Hooper. The Galactic Center GeV excess from a series of leptonic cosmic-ray outbursts. J. Cosmology Astropart. Phys., 12:005, December 2015.

[101] Ilias Cholis, Tim Linden, and Dan Hooper. A robust excess in the cosmic-ray antiproton spectrum: Implications for annihilating dark matter. Phys. Rev. D, 99(10):103026, May 2019.

[102] M. Cirelli and P. Panci. Inverse Compton constraints on the Dark Matter e excesses. *Nuclear Physics B*, 821:399–416, November 2009.

[103] Douglas Clowe, Maru**s**a Brada**c**, Anthony H. Gonzalez, Maxim Markevitch, Scott W. Randall, Christine Jones, and Dennis Zaritsky. A Direct Empirical Proof of the Existence of Dark Matter. ApJ, 648(2):L109–L113, September 2006.

[104] Alain Coc, Elisabeth Vangioni-Flam, Pierre Descouvemont, Abderrahim Adahchour, and Carmen Angulo. Updated Big Bang Nucleosynthesis Compared with Wilkinson Microwave Anisotropy Probe Observations and the Abundance of Light Elements. ApJ, 600(2):544–552, January 2004.

[105] S. Colafrancesco and P. Blasi. Clusters of galaxies and the diffuse gamma-ray background. *Astroparticle Physics*, 9:227–246, October 1998.

[106] S. Colafrancesco, S. Profumo, and P. Ullio. Multi-frequency analysis of neutralino dark matter annihilations in the Coma cluster. A&A, 455:21–43, August 2006.

[107] S. Colafrancesco, S. Profumo, and P. Ullio. Detecting dark matter WIMPs in the Draco dwarf: A multiwavelength perspective. Phys. Rev. D, 75(2):023513, January 2007.

[108] Adam Coogan, Logan Morrison, and Stefano Profumo. Hazma: a python toolkit for studying indirect detection of sub-GeV dark matter. J. Cosmology Astropart. Phys., 2020(1):056, January 2020.

[109] R. H. W. Cook et al. Searching for dark matter signals from local dwarf spheroidal galaxies at low radio frequencies in the GLEAM survey. MNRAS, 494(1):135–145, March 2020.

[110] S. Courteau, L. M. Widrow, M. McDonald, P. Guhathakurta, K. M. Gilbert, Y. Zhu, R. L. Beaton, and S. R. Majewski. The Luminosity Profile and Structural Parameters of the Andromeda Galaxy. ApJ, 739:20, September 2011.

[111] R. M. Crocker, D. I. Jones, F. Aharonian, C. J. Law, F. Melia, T. Oka, and J. Ott. Wild at Heart: the particle astrophysics of the Galactic Centre. MNRAS, 413:763–788, May 2011.

[112] Aidan C. Crook, John P. Huchra, Nathalie Martimbeau, Karen L. Masters, Tom Jarrett, and Lucas M. Macri. Groups of Galaxies in the Two Micron All Sky Redshift Survey. ApJ, 655(2):790–813, February 2007.

[113] Francis-Yan Cyr-Racine and Kris Sigurdson. Cosmology of atomic dark matter. Phys. Rev. D, 87(10):103515, May 2013.

[114] Dark Energy Survey Collaboration. Dark Energy Survey year 1 results: Cosmological constraints from galaxy clustering and weak lensing. Phys. Rev. D, 98(4):043526, August 2018.

[115] Romeel Davé, David N. Spergel, Paul J. Steinhardt, and Benjamin D. Wandelt. Halo Properties in Cosmological Simulations of Self-interacting Cold Dark Matter. ApJ, 547(2):574–589, February 2001.

[116] T. Daylan, D. P. Finkbeiner, D. Hooper, T. Linden, S. K. N. Portillo, N. L. Rodd, and T. R. Slatyer. The characterization of the gamma-ray signal from the central Milky Way: A case for annihilating dark matter. *Physics of the Dark Universe*, 12:1–23, June 2016.

[117] A. de Angelis et al. Science with e-ASTROGAM. A space mission for MeV-GeV gamma-ray astrophysics. *Journal of High Energy Astrophysics*, 19:1–106, August 2018.

[118] T. Delahaye, J. Lavalle, R. Lineros, F. Donato, and N. Fornengo. Galactic electrons and positrons at the Earth: new estimate of the primary and secondary fluxes. A&A, 524:A51, December 2010.

[119] T. Delahaye, R. Lineros, F. Donato, N. Fornengo, J. Lavalle, P. Salati, and R. Taillet. Galactic secondary positron flux at the Earth. A&A, 501(3):821–833, Jul 2009.

[120] S. Della Torre, M. Gervasi, P. G. Rancoita, D. Rozza, and A. Treves. Pulsar Wind Nebulae as a source of the observed electron and positron excess at high energy: The case of Vela-X. *Journal of High Energy Astrophysics*, 8:27–34, December 2015.

[121] C. D. Dermer. Secondary production of neutral pi-mesons and the diffuse galactic gamma radiation. A&A, 157:223–229, March 1986.

[122] Giuseppe Di Bernardo, Carmelo Evoli, Daniele Gaggero, Dario Grasso, and Luca Maccione. Cosmic ray electrons, positrons and the synchrotron emission of the Galaxy: consistent analysis and implications. *Journal of Cosmology and Astro-Particle Physics*, 2013:036, March 2013.

[123] M. Di Mauro, F. Donato, N. Fornengo, R. Lineros, and A. Vittino. Interpretation of AMS-02 electrons and positrons data. *Journal of Cosmology and Astro-Particle Physics*, 2014:006, April 2014.

[124] Scott Dodelson. The Real Problem with MOND. *International Journal of Modern Physics D*, 20(14):2749–2753, January 2011.

[125] K. Dolag and T. A. Enßlin. Radio halos of galaxy clusters from hadronic secondary electron injection in realistic magnetic field configurations. A&A, 362:151–157, October 2000.

[126] Hui Dong, Knut Olsen, Tod Lauer, Abhijit Saha, Zhiyuan Li, Ruben García-Benito, and Rainer Schödel. The star formation history in the M31 bulge. MNRAS, 478(4):5379–5403, Aug 2018.

[127] B. T. Draine, G. Aniano, O. Krause, B. Groves, K. Sandstrom, R. Braun, A. Leroy, U. Klaas, H. Linz, H.-W. Rix, E. Schinnerer, A. Schmiedeke, and F. Walter. Andromeda's Dust. ApJ, 780:172, January 2014.

[128] A. Drlica-Wagner et al. Eight Ultra-faint Galaxy Candidates Discovered in Year Two of the Dark Energy Survey. ApJ, 813(2):109, November 2015.

[129] Alex Drlica-Wagner et al. Probing the Fundamental Nature of Dark Matter with the Large Synoptic Survey Telescope. *arXiv e-prints*, page arXiv:1902.01055, February 2019.

[130] Luke O'C. Drury. Origin of cosmic rays. *Astroparticle Physics*, 39-40:52 – 60, 2012. Cosmic Rays Topical Issue.

[131] John Dubinski and R. G. Carlberg. The Structure of Cold Dark Matter Halos. ApJ, 378:496, September 1991.

[132] L. Dugger, T. E. Jeltema, and S. Profumo. Constraints on decaying dark matter from Fermi observations of nearby galaxies and clusters. J. Cosmology Astropart. Phys., 12:015, December 2010.

[133] C. Eckner, X. Hou, P. D. Serpico, M. Winter, G. Zaharijas, P. Martin, M. di Mauro, N. Mirabal, J. Petrovic, T. Prodanovic, and J. Vandenbrouck. Millisecond pulsar origin of the Galactic center excess and extended gamma-ray emission from Andromeda - a closer look. *ArXiv e-prints*, November 2017.

[134] A. E. Egorov and E. Pierpaoli. Constraints on Dark Matter Annihilation by Radio Observations of M31. In *American Astronomical Society Meeting Abstracts #221*, volume 221 of *American Astronomical Society Meeting Abstracts*, page 125.06, January 2013.

[135] A. E. Egorov and E. Pierpaoli. Constraints on dark matter annihilation by radio observations of M31. Phys. Rev. D, 88:023504, Jul 2013.

[136] J. Einasto. On the Construction of a Composite Model for the Galaxy and on the Determination of the System of Galactic Parameters. *Trudy Astrofizicheskogo Instituta Alma-Ata*, 5:87–100, 1965.

[137] Oliver D. Elbert, James S. Bullock, Shea Garrison-Kimmel, Miguel Rocha, Jose Oñorbe, and Annika H. G. Peter. Core formation in dwarf haloes with self-interacting dark matter: no fine-tuning necessary. MNRAS, 453(1):29–37, October 2015.

[138] Oliver D. Elbert, James S. Bullock, Manoj Kaplinghat, Shea Garrison-Kimmel, Andrew S. Graus, and Miguel Rocha. A Testable Conspiracy: Simulating Baryonic Effects on Self-interacting Dark Matter Halos. ApJ, 853(2):109, February 2018.

[139] JiJi Fan, Andrey Katz, Lisa Randall, and Matthew Reece. Double-Disk Dark Matter. *Physics of the Dark Universe*, 2(3):139–156, September 2013.

[140] Kun Fang, Bing-Bing Wang, Xiao-Jun Bi, Su-Jie Lin, and Peng-Fei Yin. Perspective on the Cosmic-ray Electron Spectrum above TeV. ApJ, 836:172, February 2017.

[141] Jonathan L. Feng, Manoj Kaplinghat, Huitzu Tu, and Hai-Bo Yu. Hidden charged dark matter. J. Cosmology Astropart. Phys., 2009(7):004, July 2009.

[142] Jonathan L. Feng, Manoj Kaplinghat, and Hai-Bo Yu. Halo-Shape and Relic-Density Exclusions of Sommerfeld-Enhanced Dark Matter Explanations of Cosmic Ray Excesses. Phys. Rev. Lett., 104(15):151301, April 2010.

[143] Li Feng, Zhiyuan Li, Meng Su, Pak-Hin T. Tam, and Yang Chen. Searching for GeV gamma-ray emission from the bulge of M31. *arXiv e-prints*, page arXiv:1810.10721, October 2018.

[144] L. Feretti, G. Giovannini, F. Govoni, and M. Murgia. Clusters of galaxies: observational properties of the diffuse radio emission. A&A Rev., 20:54, May 2012.

[145] K. Ferrière, W. Gillard, and P. Jean. Spatial distribution of interstellar gas in the innermost 3 kpc of our galaxy. A&A, 467:611–627, May 2007.

[146] C. E. Fichtel, R. C. Hartman, D. A. Kniffen, D. J. Thompson, G. F. Bignami, H. Ögelman, M. E. Özel, and T. Tümer. High-energy gamma-ray results from the second Small Astronomy Satellite. ApJ, 198:163–182, May 1975.

[147] A. Fletcher, E. M. Berkhuijsen, R. Beck, and A. Shukurov. The magnetic field of M 31 from multi-wavelength radio polarization observations. A&A, 414:53–67, January 2004.

[148] Ricardo A. Flores and Joel R. Primack. Observational and Theoretical Constraints on Singular Dark Matter Halos. ApJ, 427:L1, May 1994.

[149] George P. Ford, Walter K. Gear, Matthew W. L. Smith, Steve A. Eales, Maarten Baes, George J. Bendo, Médéric Boquien, Alessandro Boselli, Asantha R. Cooray, and Ilse De Looze. Herschel Exploitation of Local Galaxy Andromeda (HELGA). III. The Star Formation Law in M31. ApJ, 769(1):55, May 2013.

[150] N. Fornengo, L. Pieri, and S. Scopel. Neutralino annihilation into γ rays in the Milky Way and in external galaxies. Phys. Rev. D, 70:103529, Nov 2004.

[151] G. Fragione, F. Antonini, and O. Y. Gnedin. Millisecond Pulsars and the Gamma-Ray Excess in Andromeda. ApJ, 871:L8, January 2019.

[152] Antonella Fruscione, Jonathan C. McDowell, Glenn E. Allen, Nancy S. Brickhouse, Douglas J. Burke, John E. Davis, Nick Durham, Martin Elvis, Elizabeth C. Galle, Daniel E. Harris, David P. Huenemoerder, John C. Houck, Bish Ishibashi, Margarita Karovska, Fabrizio Nicastro, Michael S. Noble, Michael A. Nowak, Frank A. Primini, Aneta Siemiginowska, Randall K. Smith, and Michael Wise. *CIAO: Chandra's data analysis system*, volume 6270 of *Society of Photo-Optical Instrumentation Engineers (SPIE) Conference Series*, page 62701V. 2006.

[153] B. M. Gaensler, G. J. Madsen, S. Chatterjee, and S. A. Mao. The Vertical Structure of Warm Ionised Gas in the Milky Way. *Publications of the Astronomical Society of Australia*, 25:184–200, November 2008.

[154] D. Gaggero, M. Taoso, A. Urbano, M. Valli, and P. Ullio. Towards a realistic astrophysical interpretation of the gamma-ray Galactic center excess. J. Cosmology Astropart. Phys., 12:056, December 2015.

[155] Daniele Gaggero and Mauro Valli. Impact of cosmic-ray physics on dark matter indirect searches. *arXiv e-prints*, page arXiv:1802.00636, February 2018.

[156] Mark Galassi, Jim Davies, James Theiler, Brian Gough, Gerard Jungman, Michael Booth, and Fabrice Rossi. *GNU Scientific Library Reference Manual - Third Edition.* Network Theory Ltd., 3rd edition, 2009.

[157] Fuchang Gao and Lixing Han. Implementing the nelder-mead simplex algorithm with adaptive parameters. *Computational Optimization and Applications*, 51(1):259–277, May 2010.

[158] Leo Gendelev, Stefano Profumo, and Michael Dormody. The contribution of Fermi gamma-ray pulsars to the local flux of cosmic-ray electrons and positrons. *Journal of Cosmology and Astro-Particle Physics*, 2010:016, February 2010.

[159] Ortwin Gerhard, Andi Kronawitter, R. P. Saglia, and Ralf Bender. Dynamical Family Properties and Dark Halo Scaling Relations of Giant Elliptical Galaxies. AJ, 121(4):1936–1951, April 2001.

[160] R. Gießübel and R. Beck. The magnetic field structure of the central region in M 31. A&A, 571:A61, November 2014.

[161] R. Gießübel, G. Heald, R. Beck, and T. G. Arshakian. Polarized synchrotron radiation from the Andromeda galaxy M 31 and background sources at 350 MHz. A&A, 559:A27, November 2013.

[162] V. L. Ginzburg and S. I. Syrovatskii. *The Origin of Cosmic Rays.* 1964.

[163] G. Giovannini, A. Bonafede, L. Feretti, F. Govoni, M. Murgia, F. Ferrari, and G. Monti. Radio halos in nearby (z < 0.4) clusters of galaxies. A&A, 507:1257–1270, December 2009.

[164] Tobias Goerdt, Oleg Y. Gnedin, Ben Moore, Jürg Diemand , and Joachim Stadel. The survival and disruption of cold dark matter microhaloes: implications for direct and indirect detection experiments. MNRAS, 375(1):191–198, February 2007.

[165] P. Gondolo, J. Edsjö, P. Ullio, L. Bergström, M. Schelke, and E. A. Baltz. DarkSUSY: computing supersymmetric dark matter properties numerically. J. Cosmology Astropart. Phys., 7:008, July 2004.

[166] L. Goodenough and D. Hooper. Possible Evidence For Dark Matter Annihilation In The Inner Milky Way From The Fermi Gamma Ray Space Telescope. *ArXiv e-prints*, October 2009.

157

[167] Chris Gordon and Oscar Macías. Dark matter and pulsar model constraints from galactic center fermi-lat gamma-ray observations. *Phys. Rev. D*, 88:083521, Oct 2013.

[168] F. Governato, C. Brook, L. Mayer, A. Brooks, G. Rhee, J. Wadsley, P. Jonsson, B. Willman, G. Stinson, T. Quinn, and P. Madau. Bulgeless dwarf galaxies and dark matter cores from supernova-driven outflows. Nature, 463(7278):203–206, January 2010.

[169] F. Govoni, G. B. Taylor, D. Dallacasa, L. Feretti, and G. Giovannini. The magnetic field in Abell 514. *Highlights of Astronomy*, 12:537, 2002.

[170] B. Groves, O. Krause, K. Sandstrom, A. Schmiedeke, A. Leroy, H. Linz, M. Kapala, H.-W. Rix, E. Schinnerer, F. Tabatabaei, F. Walter, and E. da Cunha. The heating of dust by old stellar populations in the bulge of M31. MNRAS, 426:892–902, October 2012.

[171] Stephen Hawking. Gravitationally collapsed objects of very low mass. MNRAS, 152:75, January 1971.

[172] Lars Hernquist. An Analytical Model for Spherical Galaxies and Bulges. ApJ, 356:359, June 1990.

[173] G. Hinshaw, D. Larson, E. Komatsu, D. N. Spergel, C. L. Bennett, J. Dunkley, M. R. Nolta, M. Halpern, R. S. Hill, N. Odegard, L. Page, K. M. Smith, J. L. Weiland, B. Gold, N. Jarosik, A. Kogut, M. Limon, S. S. Meyer, G. S. Tucker, E. Wollack, and E. L. Wright. Nine-year Wilkinson Microwave Anisotropy Probe (WMAP) Observations: Cosmological Parameter Results. ApJS, 208(2):19, October 2013.

[174] P. Hoernes, R. Beck, and E. M. Berkhuijsen. Properties of synchrotron emission and magnetic fields in the central region of M31. In Y. Sofue, editor, *The Central Regions of the Galaxy and Galaxies*, volume 184 of *IAU Symposium*, page 351, 1998.

[175] D. Hooper and L. Goodenough. Dark matter annihilation in the Galactic Center as seen by the Fermi Gamma Ray Space Telescope. *Physics Letters B*, 697:412–428, March 2011.

[176] Dan Hooper, Pasquale Blasi, and Pasquale Dario Serpico. Pulsars as the sources of high energy cosmic ray positrons. *Journal of Cosmology and Astro-Particle Physics*, 2009:025, January 2009.

[177] Dan Hooper and Tim Linden. Origin of the gamma rays from the Galactic Center. Phys. Rev. D, 84(12):123005, December 2011.

[178] Shunsaku Horiuchi, John F. Beacom, Christopher S. Kochanek, Jose L. Prieto, K. Z. Stanek, and Todd A. Thompson. The Cosmic Core-collapse Supernova Rate Does Not Match the Massive-star Formation Rate. ApJ, 738(2):154, Sep 2011.

[179] Wayne Hu, Rennan Barkana, and Andrei Gruzinov. Fuzzy Cold Dark Matter: The Wave Properties of Ultralight Particles. Phys. Rev. Lett., 85(6):1158–1161, August 2000.

[180] C.-Y. Huang. Gamma-Ray Energy Spectra through Decays of Neutral Pions Produced in Proton-Proton Interactions. *International Cosmic Ray Conference*, 4:2297, July 2003.

[181] John P. Huchra, Lucas M. Macri, Karen L. Masters, Thomas H. Jarrett, Perry Berlind, Michael Calkins, Aidan C. Crook, Roc Cutri, Pirin Erdo**g**du, Emilio Falco, Teddy George, Conrad M. Hutcheson, Ofer Lahav, Jeff Mader, Jessica D. Mink, Nathalie Martimbeau, Stephen Schneider, Michael Skrutskie, Susan Tokarz, and Michael Westover. The 2MASS Redshift Survey—Description and Data Release. ApJS, 199(2):26, April 2012.

[182] D. S. Hudson, R. Mittal, T. H. Reiprich, P. E. J. Nulsen, H. Andernach, and C. L. Sarazin. What is a cool-core cluster? a detailed analysis of the cores of the X-ray flux-limited HIFLUGCS cluster sample. A&A, 513:A37, April 2010.

[183] Philip J. Humphrey, David A. Buote, Claude R. Canizares, Andrew C. Fabian, and Jon M. Miller. A Census of Baryons and Dark Matter in an Isolated, Milky Way Sized Elliptical Galaxy. ApJ, 729(1):53, March 2011.

[184] Philip J. Humphrey, David A. Buote, Fabio Gastaldello, Luca Zappacosta, James S. Bullock, Fabrizio Brighenti, and William G. Mathews. A Chandra View of Dark Matter in Early-Type Galaxies. ApJ, 646(2):899–918, August 2006.

[185] Philip J. Humphrey, David A. Buote, Ewan O'Sullivan, and Trevor J. Ponman. The ElIXr Galaxy Survey. II. Baryons and Dark Matter in an Isolated Elliptical Galaxy. ApJ, 755(2):166, August 2012.

[186] IceCube Collaboration. Search for Neutrinos from Dark Matter Self-Annihilations in the center of the Milky Way with 3 years of IceCube/DeepCore. *arXiv e-prints*, page arXiv:1705.08103, May 2017.

[187] T. Jeltema and S. Profumo. Deep XMM observations of Draco rule out at the 99 per cent confidence level a dark matter decay origin for the 3.5 keV line. MNRAS, 458:3592–3596, June 2016.

[188] T. E. Jeltema and S. Profumo. Fitting the gamma-ray spectrum from dark matter with DMFIT: GLAST and the galactic center region. J. Cosmology Astropart. Phys., 11:003, November 2008.

[189] T. E. Jeltema and S. Profumo. Searching for Dark Matter with X-Ray Observations of Local Dwarf Galaxies. ApJ, 686:1045–1055, October 2008.

[190] T. E. Jeltema and S. Profumo. Dark matter detection with hard X-ray telescopes. MNRAS, 421:1215–1221, April 2012.

[191] G. Jungman, M. Kamionkowski, and K. Griest. Supersymmetric dark matter. Phys. Rep., 267:195–373, March 1996.

[192] Ayuki Kamada, Manoj Kaplinghat, Andrew B. Pace, and Hai-Bo Yu. Self-Interacting Dark Matter Can Explain Diverse Galactic Rotation Curves. Phys. Rev. Lett., 119(11):111102, September 2017.

[193] Manoj Kaplinghat, Sean Tulin, and Hai-Bo Yu. Dark Matter Halos as Particle Colliders: Unified Solution to Small-Scale Structure Puzzles from Dwarfs to Clusters. Phys. Rev. Lett., 116(4):041302, January 2016.

[194] Arpan Kar, Sourav Mitra, Biswarup Mukhopadhyaya, and Tirthankar Roy Choudhury. Heavy dark matter particle annihilation in dwarf spheroidal galaxies: Radio signals at the SKA telescope. Phys. Rev. D, 101(2):023015, January 2020.

[195] I. D. Karachentsev, V. E. Karachentseva, W. K. Huchtmeier, and D. I. Makarov. A Catalog of Neighboring Galaxies. AJ, 127:2031–2068, April 2004.

[196] Chris Karwin, Simona Murgia, Sheldon Campbell, and Igor Moskalenko. Fermi-LAT Observations of Gamma-Ray Emission Towards the Outer Halo of M31. *arXiv e-prints*, page arXiv:1903.10533, Mar 2019.

[197] Anatoly Klypin, Andrey V. Kravtsov, Octavio Valenzuela, and Francisco Prada. Where Are the Missing Galactic Satellites? ApJ, 522(1):82–92, September 1999.

[198] C. G. Lacey and J. P. Ostriker. Massive black holes in galactic halos ? ApJ, 299:633–652, December 1985.

[199] Brian C. Lacki, Todd A. Thompson, and Eliot Quataert. The Physics of the Far-infrared-Radio Correlation. I. Calorimetry, Conspiracy, and Implications. ApJ, 717(1):1–28, Jul 2010.

[200] R. Laha, K. C. Y. Ng, B. Dasgupta, and S. Horiuchi. Galactic Center radio constraints on gamma-ray lines from dark matter annihilation. Phys. Rev. D, 87(4):043516, February 2013.

[201] A. Lazarian and J. Cho. Magnetic Reconnection and Turbulent Mixing: From ISM to Clusters of Galaxies. Ap&SS, 289:307–318, February 2004.

[202] Jae-Weon Lee. Brief History of Ultra-light Scalar Dark Matter Models. In *European Physical Journal Web of Conferences*, volume 168 of *European Physical Journal Web of Conferences*, page 06005, January 2018.

[203] Z. Li, X. Huang, Q. Yuan, and Y. Xu. Constraints on the dark matter annihilation from Fermi-LAT observation of M31. J. Cosmology Astropart. Phys., 12:028, December 2016.

[204] Zhengwei Li, Xiaoyuan Huang, Qiang Yuan, and Yupeng Xu. Constraints on the dark matter annihilation from Fermi-LAT observation of M31. *Journal of Cosmology and Astro-Particle Physics*, 2016:028, December 2016.

[205] Zhiyuan Li and Q. Daniel Wang. Chandra Detection of Diffuse Hot Gas in and around the M31 Bulge. ApJ, 668:L39–L42, October 2007.

[206] Tim Linden and Stefano Profumo. Probing the Pulsar Origin of the Anomalous Positron Fraction with AMS-02 and Atmospheric Cherenkov Telescopes. ApJ, 772:18, July 2013.

[207] J. Liu, Q. D. Wang, Z. Li, and J. R. Peterson. X-ray spectroscopy of the hot gas in the M31 bulge. MNRAS, 404:1879–1885, June 2010.

[208] Abraham Loeb and Neal Weiner. Cores in Dwarf Galaxies from Dark Matter with a Yukawa Potential. Phys. Rev. Lett., 106(17):171302, April 2011.

[209] Malcolm S. Longair. *High Energy Astrophysics*. Cambridge University Press, New York, 3 edition, 2011.

[210] Chung-Pei Ma, Jenny E. Greene, Nicholas McConnell, Ryan Janish, John P. Blakeslee, Jens Thomas, and Jeremy D. Murphy. The MASSIVE Survey. I. A Volume-limited Integral-field Spectroscopic Study of the Most Massive Early-type Galaxies within 108 Mpc. ApJ, 795(2):158, November 2014.

[211] Dmitry Malyshev, Ilias Cholis, and Joseph Gelfand. Pulsars versus dark matter interpretation of ATIC/PAMELA. Phys. Rev. D, 80:063005, September 2009.

[212] S. Manconi, M. Di Mauro, and F. Donato. Dipole anisotropy in cosmic electrons and positrons: inspection on local sources. *Journal of Cosmology and Astro-Particle Physics*, 2017:006, January 2017.

[213] K. Mannheim and R. Schlickeiser. Interactions of cosmic ray nuclei. A&A, 286:983–996, June 1994.

[214] M. Markevitch, A. H. Gonzalez, D. Clowe, A. Vikhlinin, W. Forman, C. Jones, S. Murray, and W. Tucker. Direct Constraints on the Dark Matter Self-Interaction Cross Section from the Merging Galaxy Cluster 1E 0657-56. ApJ, 606(2):819–824, May 2004.

[215] M. L. Mateo. Dwarf Galaxies of the Local Group. ARA&A, 36:435–506, 1998.

[216] D. Maurin, F. Donato, R. Taillet, and P. Salati. Cosmic Rays below Z=30 in a Diffusion Model: New Constraints on Propagation Parameters. ApJ, 555:585–596, July 2001.

[217] A. W. McConnachie. The Observed Properties of Dwarf Galaxies in and around the Local Group. AJ, 144:4, July 2012.

[218] A. McCormick, S. Veilleux, and D. S. N. Rupke. Dusty Winds: Extraplanar Polycyclic Aromatic Hydrocarbon Features of Nearby Galaxies. ApJ, 774:126, September 2013.

[219] A. McDaniel, T. Jeltema, and S. Profumo. Multiwavelength analysis of annihilating dark matter as the origin of the gamma-ray emission from M31. Phys. Rev. D, 97(10):103021, May 2018.

[220] A. McDaniel, T. Jeltema, S. Profumo, and E. Storm. Multiwavelength analysis of dark matter annihilation and RX-DMFIT. J. Cosmology Astropart. Phys., 9:027, September 2017.

[221] Alex McDaniel, Tesla Jeltema, and Stefano Profumo. Exploring a cosmic-ray origin of the multiwavelength emission in M31. Phys. Rev. D, 100(2):023014, July 2019.

[222] Samuel D. McDermott, Hai-Bo Yu, and Kathryn M. Zurek. Turning off the lights: How dark is dark matter? Phys. Rev. D, 83(6):063509, March 2011.

[223] Julie McEnery et al. All-sky Medium Energy Gamma-ray Observatory: Exploring the Extreme Multimessenger Universe. In **??**jnlBAAS, volume 51, page 245, September 2019.

[224] Stacy S. McGaugh. A tale of two paradigms: the mutual incommensurability of ΛCDM and MOND. *Canadian Journal of Physics*, 93(2):250–259, February 2015.

[225] S. L. W. McMillan, M. P. Kowalski, and M. P. Ulmer. X-Ray Morphologies of Abell Clusters. ApJS, 70:723, August 1989.

[226] E. Memola, P. Salucci, and A. Babić. Dark matter halos around isolated ellipticals. A&A, 534:A50, October 2011.

[227] Massimo Meneghetti, Naoki Yoshida, Matthias Bartelmann, Lauro Moscardini, Volker Springel, Giuseppe Tormen, and Simon D. M. White. Giant cluster arcs as a constraint on the scattering cross-section of dark matter. MNRAS, 325(1):435–442, July 2001.

[228] M. Milgrom. A modification of the Newtonian dynamics - Implications for galaxies. ApJ, 270:371–389, July 1983.

[229] M. Milgrom. A modification of the Newtonian dynamics as a possible alternative to the hidden mass hypothesis. ApJ, 270:365–370, July 1983.

[230] Mordehai Milgrom. Testing MOND over a Wide Acceleration Range in X-Ray Ellipticals. Phys. Rev. Lett., 109(13):131101, September 2012.

[231] Jordi Miralda-Escudé. A Test of the Collisional Dark Matter Hypothesis from Cluster Lensing. ApJ, 564(1):60–64, January 2002.

[232] Ben Moore. An Upper Limit to the Mass of Black Holes in the Halo of the Galaxy. ApJ, 413:L93, August 1993.

[233] Ben Moore. Evidence against dissipation-less dark matter from observations of galaxy haloes. Nature, 370(6491):629–631, August 1994.

[234] Ben Moore, Sebastiano Ghigna, Fabio Governato, George Lake, Thomas Quinn, Joachim Stadel, and Paolo Tozzi. Dark Matter Substructure within Galactic Halos. ApJ, 524(1):L19–L22, October 1999.

[235] A. Morselli and CTA Consortium. The Dark Matter Programme of the Cherenkov Telescope Array. In *35th International Cosmic Ray Conference (ICRC2017)*, volume 301 of *International Cosmic Ray Conference*, page 921, January 2017.

[236] M. Murgia, F. Govoni, L. Feretti, G. Giovannini, D. Dallacasa, R. Fanti, G. B. Taylor, and K. Dolag. Magnetic fields and Faraday rotation in clusters of galaxies. A&A, 424:429–446, September 2004.

[237] E. J. Murphy, G. Helou, R. Braun, J. D. P. Kenney, L. Armus, D. Calzetti, B. T. Draine, Jr. Kennicutt, R. C., H. Roussel, F. Walter, G. J. Bendo, B. Buckalew, D. A. Dale, C. W. Engelbracht, J. D. T. Smith, and M. D. Thornley. The Effect of Star Formation on the Far-Infrared-Radio Correlation within Galaxies. ApJ, 651:L111–L115, November 2006.

[238] A. Natarajan, J. E. Aguirre, K. Spekkens, and B. S. Mason. Green Bank Telescope Constraints on Dark Matter Annihilation in Segue I. *ArXiv e-prints*, July 2015.

[239] A. Natarajan, J. B. Peterson, T. C. Voytek, K. Spekkens, B. Mason, J. Aguirre, and B. Willman. Bounds on dark matter properties from radio observations of Ursa Major II using the Green Bank Telescope. Phys. Rev. D, 88(8):083535, October 2013.

[240] J. F. Navarro, C. S. Frenk, and S. D. M. White. The Structure of Cold Dark Matter Halos. ApJ, 462:563, May 1996.

[241] J. F. Navarro, C. S. Frenk, and S. D. M. White. A Universal Density Profile from Hierarchical Clustering. ApJ, 490:493–508, December 1997.

[242] J. F. Navarro, E. Hayashi, C. Power, A. R. Jenkins, C. S. Frenk, S. D. M. White, V. Springel, J. Stadel, and T. R. Quinn. The inner structure of ΛCDM haloes - III. Universality and asymptotic slopes. MNRAS, 349:1039–1051, April 2004.

[243] Julio F. Navarro, Vincent R. Eke, and Carlos S. Frenk. The cores of dwarf galaxy haloes. MNRAS, 283(3):L72–L78, December 1996.

[244] J. A. Nelder and R. Mead. A simplex method for function minimization. *The Computer Journal*, 7(4):308–313, January 1965.

[245] A. Neronov and D. Malyshev. Toward a full test of the ν MSM sterile neutrino dark matter model with Athena. Phys. Rev. D, 93(6):063518, March 2016.

[246] K. C. Y. Ng, B. M. Roach, K. Perez, J. F. Beacom, S. Horiuchi, R. Krivonos, and D. R. Wik. New Constraints on Sterile Neutrino Dark Matter from *NuSTAR* M31 Observations. *arXiv e-prints*, January 2019.

[247] Keith A. Olive. TASI Lectures on Dark Matter. *arXiv e-prints*, pages astro–ph/0301505, January 2003.

[248] Knut A. G. Olsen, Robert D. Blum, Andrew W. Stephens, Tim J. Davidge, Philip Massey, Stephen E. Strom, and François Rigaut. The Star Formation Histories of the Bulge and Disk of M31 from Resolved Stars in the Near-Infrared. AJ, 132(1):271–289, Jul 2006.

[249] J. H. Oort. Some Problems Concerning the Structure and Dynamics of the Galactic System and the Elliptical Nebulae NGC 3115 and 4494. ApJ, 91:273, April 1940.

[250] E. O'Sullivan and T. J. Ponman. The isolated elliptical NGC 4555 observed with Chandra. MNRAS, 354(3):935–944, November 2004.

[251] T. A. D. Paglione, A. P. Marscher, J. M. Jackson, and D. L. Bertsch. Diffuse Gamma-Ray Emission from the Starburst Galaxy NGC 253. ApJ, 460:295, March 1996.

[252] Vasiliki Pavlidou and Brian D. Fields. Diffuse Gamma Rays from Local Group Galaxies. ApJ, 558:63–71, September 2001.

[253] P. J. E. Peebles and J. T. Yu. Primeval Adiabatic Perturbation in an Expanding Universe. ApJ, 162:815, December 1970.

[254] Annika H. G. Peter, Miguel Rocha, James S. Bullock, and Manoj Kaplinghat. Cosmological simulations with self-interacting dark matter - II. Halo shapes versus observations. MNRAS, 430(1):105–120, March 2013.

[255] C. Pfrommer and T. A. Enßlin. Constraining the population of cosmic ray protons in cooling flow clusters with γ-ray and radio observations: Are radio mini-halos of hadronic origin? A&A, 413:17–36, January 2004.

[256] A. M. T. Pollock, G. F. Bignami, W. Hermsen, G. Kanbach, G. G. Lichti, J. L. Masnou, B. N. Swanenburg, and R. D. Wills. Search for gamma-radiation from extragalactic objects using a likelihood method. A&A, 94:116–120, Jan 1981.

[257] T. A. Porter, I. V. Moskalenko, A. W. Strong, E. Orlando, and L. Bouchet. Inverse Compton Origin of the Hard X-Ray and Soft Gamma-Ray Emission from the Galactic Ridge. ApJ, 682:400–407, July 2008.

[258] William H. Press. *Numerical Recipes 3rd Edition: The Art of Scientific Computing*. Cambridge University Press, sep 2007.

[259] S. Profumo and P. Ullio. Multi-wavelength Searches for Particle Dark Matter. *ArXiv e-prints*, January 2010.

[260] Stefano Profumo, Farinaldo Queiroz, and Clarissa Siqueira. Has AMS-02 Observed Two-Component Dark Matter? *arXiv e-prints*, page arXiv:1903.07638, March 2019.

[261] S. Rahmani, S. Lianou, and P. Barmby. Star formation laws in the Andromeda galaxy: gas, stars, metals and the surface density of star formation. MNRAS, 456(4):4128–4144, Mar 2016.

[262] Scott W. Randall, Maxim Markevitch, Douglas Clowe, Anthony H. Gonzalez, and Marusa Brada**c**. Constraints on the Self-Interaction Cross Section of Dark Matter from Numerical Simulations of the Merging Galaxy Cluster 1E 0657-56. ApJ, 679(2):1173–1180, June 2008.

[263] M. Regis, S. Colafrancesco, S. Profumo, W. J. G. de Blok, M. Massardi, and L. Richter. Local Group dSph radio survey with ATCA (III): constraints on particle dark matter. J. Cosmology Astropart. Phys., 10:016, October 2014.

[264] M. Regis and P. Ullio. Multiwavelength signals of dark matter annihilations at the Galactic center. Phys. Rev. D, 78(4):043505, August 2008.

[265] Adam G. Riess et al. Observational Evidence from Supernovae for an Accelerating Universe and a Cosmological Constant. AJ, 116(3):1009–1038, September 1998.

[266] Lucia Rinchiuso. Latest results on dark matter searches with H.E.S.S. In *European Physical Journal Web of Conferences*, volume 209 of *European Physical Journal Web of Conferences*, page 01023, September 2019.

[267] Hans-Walter Rix and George Lake. Can the Dark Matter be 10 6 Solar Mass Objects? ApJ, 417:L1, November 1993.

[268] Miguel Rocha, Annika H. G. Peter, James S. Bullock, Manoj Kaplinghat, Shea Garrison-Kimmel, Jose Oñorbe, and Leonidas A. Moustakas. Cosmological simulations with self-interacting dark matter - I. Constant-density cores and substructure. MNRAS, 430(1):81–104, March 2013.

[269] Aaron J. Romanowsky and Christopher S. Kochanek. Twisting of X-Ray Isophotes in Triaxial Galaxies. ApJ, 493(2):641–649, January 1998.

[270] Marco Roncadelli, Giorgio Galanti, and Alessandro De Angelis. Axion-like particles and e-ASTROGAM. *arXiv e-prints*, page arXiv:1704.00144, April 2017.

[271] R. Rubenzahl, S. BenZvi, J. Wood, and HAWC Collaboration. Limits on the Emission of Gamma Rays from M31 (The Andromeda Galaxy) with HAWC. *International Cosmic Ray Conference*, 301:594, Jan 2017.

[272] Vera C. Rubin and Jr. Ford, W. Kent. Rotation of the Andromeda Nebula from a Spectroscopic Survey of Emission Regions. ApJ, 159:379, February 1970.

[273] G. B. Rybicki and A. P. Lightman. *Radiative processes in astrophysics*. 1979.

[274] B. S. Ryden and J. E. Gunn. Galaxy formation by gravitational collapse. ApJ, 318:15–31, July 1987.

[275] R. P. Saglia, M. Fabricius, R. Bender, M. Montalto, C. H. Lee, A. Riffeser, S. Seitz, L. Morganti, O. Gerhard, and U. Hopp. The old and heavy bulge of M 31 . I. Kinematics and stellar populations. A&A, 509:A61, Jan 2010.

[276] Edwin E. Salpeter. The Luminosity Function and Stellar Evolution. ApJ, 121:161, Jan 1955.

[277] Christoph Saulder, Eelco van Kampen, Igor V. Chilingarian, Steffen Mieske, and Werner W. Zeilinger. The matter distribution in the local Universe as derived from galaxy groups in SDSS DR12 and 2MRS. A&A, 596:A14, November 2016.

[278] R. Schlickeiser. *Cosmic Ray Astrophysics.* 2002.

[279] Marc Schumann. Direct detection of WIMP dark matter: concepts and status. *Journal of Physics G Nuclear Physics*, 46(10):103003, October 2019.

[280] R. Shirey, R. Soria, K. Borozdin, J. P. Osborne, A. Tiengo, M. Guainazzi, C. Hayter, N. La Palombara, K. Mason, S. Molendi, F. Paerels, W. Pietsch, W. Priedhorsky, A. M. Read, M. G. Watson, and R. G. West. The central region of M 31 observed with XMM-Newton. I. Group properties and diffuse emission. A&A, 365:L195–L201, January 2001.

[281] Steven L. Snowden and K. D. Kuntz. Analysis of XMM-Newton Data from Extended Sources and the Diffuse X-ray Background. In *American Astronomical Society Meeting Abstracts #217*, volume 217 of *American Astronomical Society Meeting Abstracts*, page 344.17, January 2011.

[282] Y. Sofue. Dark halos of M 31 and the Milky Way. PASJ, 67:75, August 2015.

[283] K. Spekkens, B. S. Mason, J. E. Aguirre, and B. Nhan. A Deep Search for Extended Radio Continuum Emission from Dwarf Spheroidal Galaxies: Implications for Particle Dark Matter. ApJ, 773:61, August 2013.

[284] David N. Spergel and Paul J. Steinhardt. Observational Evidence for Self-Interacting Cold Dark Matter. Phys. Rev. Lett., 84(17):3760–3763, April 2000.

[285] V. Springel, J. Wang, M. Vogelsberger, A. Ludlow, A. Jenkins, A. Helmi, J. F. Navarro, C. S. Frenk, and S. D. M. White. The Aquarius Project: the subhaloes of galactic haloes. MNRAS, 391(4):1685–1711, December 2008.

[286] Volker Springel, Carlos S. Frenk, and Simon D. M. White. The large-scale structure of the Universe. Nature, 440(7088):1137–1144, April 2006.

[287] Christopher M. Springob, Christina Magoulas, Matthew Colless, Jeremy Mould, Pirin Erdoğdu, D. Heath Jones, John R. Lucey, Lachlan Campbell, and Christopher J. Fluke. The 6dF Galaxy Survey: peculiar velocity field and cosmography. MNRAS, 445(3):2677–2697, December 2014.

[288] P. Sreekumar, D. L. Bertsch, B. L. Dingus, J. A. Esposito, C. E. Fichtel, R. C. Hartman, S. D. Hunter, G. Kanbach, D. A. Kniffen, Y. C. Lin, J. R. Mattox, H. A. Mayer-Hasselwander, P. F. Michelson, C. von Montigny, P. L. Nolan, E. J. Schneid, and D. J. Thompson. A Study of M31, M87, NGC 253, and M82 in High-Energy Gamma Rays. ApJ, 426:105, May 1994.

[289] K. Z. Stanek and P. M. Garnavich. Distance to M31 with the Hubble Space Telescope and HIPPARCOS Red Clump Stars. ApJ, 503:L131–L134, August 1998.

[290] G. Steigman, B. Dasgupta, and J. F. Beacom. Precise relic WIMP abundance and its impact on searches for dark matter annihilation. Phys. Rev. D, 86(2):023506, July 2012.

[291] Gary Steigman and Michael S. Turner. Cosmological constraints on the properties of weakly interacting massive particles. *Nuclear Physics B*, 253:375–386, January 1985.

[292] E. Storm, T. E. Jeltema, S. Profumo, and L. Rudnick. Constraints on Dark Matter Annihilation in Clusters of Galaxies from Diffuse Radio Emission. ApJ, 768:106, May 2013.

[293] E. Storm, T. E. Jeltema, M. Splettstoesser, and S. Profumo. Synchrotron Emission from Dark Matter Annihilation: Predictions for Constraints from Non-detections of Galaxy Clusters with New Radio Surveys. *ArXiv e-prints*, July 2016.

[294] L. E. Strigari, S. M. Koushiappas, J. S. Bullock, M. Kaplinghat, J. D. Simon, M. Geha, and B. Willman. The Most Dark-Matter-dominated Galaxies: Predicted Gamma-Ray Signals from the Faintest Milky Way Dwarfs. ApJ, 678:614–620, May 2008.

[295] A. W. Strong, I. V. Moskalenko, and V. S. Ptuskin. Cosmic-Ray Propagation and Interactions in the Galaxy. *Annual Review of Nuclear and Particle Science*, 57:285–327, November 2007.

[296] A. W. Strong, I. V. Moskalenko, and O. Reimer. Diffuse Continuum Gamma Rays from the Galaxy. ApJ, 537:763–784, July 2000.

[297] R. Supper, G. Hasinger, W. H. G. Lewin, E. A. Magnier, J. van Paradijs, W. Pietsch, A. M. Read, and J. Trümper. The second ROSAT PSPC survey of M 31 and the complete ROSAT PSPC source list. A&A, 373:63–99, July 2001.

[298] R. Supper, G. Hasinger, W. Pietsch, J. Truemper, A. Jain, E. A. Magnier, W. H. G. Lewin, and J. van Paradijs. ROSAT PSPC survey of M 31. A&A, 317:328–349, January 1997.

[299] A. Tamm, E. Tempel, P. Tenjes, O. Tihhonova, and T. Tuvikene. Stellar mass map and dark matter distribution in M 31. A&A, 546:A4, October 2012.

[300] V. Tatischeff. Radio emission and nonlinear diffusive shock acceleration of cosmic rays in the supernova SN 1993J. A&A, 499:191–213, May 2009.

[301] A. M. Taylor, S. Gabici, and F. Aharonian. Galactic halo origin of the neutrinos detected by IceCube. Phys. Rev. D, 89(10):103003, May 2014.

[302] G. B. Taylor, N. E. Gugliucci, A. C. Fabian, J. S. Sanders, G. Gentile, and S. W. Allen. Magnetic fields in the centre of the Perseus cluster. MNRAS, 368:1500–1506, June 2006.

[303] The ANTARES Collaboration. Search for dark matter towards the Galactic Centre with 11 years of ANTARES data. *arXiv e-prints*, page arXiv:1912.05296, December 2019.

[304] G. Theureau, M. O. Hanski, N. Coudreau, N. Hallet, and J. M. Martin. Kinematics of the Local Universe. XIII. 21-cm line measurements of 452 galaxies with the Nançay radiotelescope, JHK Tully-Fisher relation, and preliminary maps of the peculiar velocity field. A&A, 465(1):71–85, April 2007.

[305] D.J. Thompson, L. Baldini, and Y. Uchiyama. Cosmic ray studies with the fermi gamma-ray space telescope large area telescope. *Astroparticle Physics*, 39-40:22 – 32, 2012. Cosmic Rays Topical Issue.

[306] John L. Tonry, Alan Dressler, John P. Blakeslee, Edward A. Ajhar, André B. Fletcher, Gerard A. Luppino, Mark R. Metzger, and Christopher B. Moore. The SBF Survey of Galaxy Distances. IV. SBF Magnitudes, Colors, and Distances. ApJ, 546(2):681–693, January 2001.

[307] Scott Tremaine and James E. Gunn. Dynamical role of light neutral leptons in cosmology. Phys. Rev. Lett., 42(6):407–410, February 1979.

[308] Sebastian Trujillo-Gomez, Anatoly Klypin, Joel Primack, and Aaron J. Romanowsky. Galaxies in ΛCDM with Halo Abundance Matching: Luminosity-Velocity Relation, Baryonic Mass-Velocity Relation, Velocity Function, and Clustering. ApJ, 742(1):16, November 2011.

[309] Robert J. Trumpler and Harold F. Weaver. *Statistical astronomy*. University of California Press, Berkeley and Los Angeles, 1953.

[310] Sean Tulin and Hai-Bo Yu. Dark matter self-interactions and small scale structure. Phys. Rep., 730:1–57, February 2018.

[311] Sean Tulin, Hai-Bo Yu, and Kathryn M. Zurek. Beyond collisionless dark matter: Particle physics dynamics for dark matter halo structure. Phys. Rev. D, 87(11):115007, June 2013.

[312] Sean Tulin, Hai-Bo Yu, and Kathryn M. Zurek. Resonant Dark Forces and Small-Scale Structure. Phys. Rev. Lett., 110(11):111301, March 2013.

[313] R. Brent Tully, Hélène M. Courtois, Andrew E. Dolphin, J. Richard Fisher, Philippe Héraudeau, Bradley A. Jacobs, Igor D. Karachentsev, Dmitry Makarov, Lidia Makarova, Sofia Mitronova, Luca Rizzi, Edward J. Shaya, Jenny G. Sorce, and Po-Feng Wu. Cosmicflows-2: The Data. AJ, 146(4):86, October 2013.

[314] V. Vacca, M. Murgia, F. Govoni, L. Feretti, G. Giovannini, R. A. Perley, and G. B. Taylor. The intracluster magnetic field power spectrum in A2199. A&A, 540:A38, April 2012.

[315] S. Veilleux, G. Cecil, and J. Bland-Hawthorn. Galactic Winds. ARA&A, 43:769–826, September 2005.

[316] A. Vikhlinin, A. V. Kravtsov, R. A. Burenin, H. Ebeling, W. R. Forman, A. Hornstrup, C. Jones, S. S. Murray, D. Nagai, H. Quintana, and A. Voevodkin. Chandra Cluster Cosmology Project III: Cosmological Parameter Constraints. ApJ, 692(2):1060–1074, February 2009.

[317] A. E. Vladimirov, G. Jóhannesson, I. V. Moskalenko, and T. A. Porter. Testing the Origin of High-energy Cosmic Rays. ApJ, 752:68, June 2012.

[318] Mark Vogelsberger, Jesus Zavala, and Abraham Loeb. Subhaloes in self-interacting galactic dark matter haloes. MNRAS, 423(4):3740–3752, July 2012.

[319] Martin Vollmann, Volker Heesen, Timothy Shimwell, Martin J. Hardcastle, Marcus Brüggen, Günter Sigl, and Huub Röttgering. Radio constraints on dark matter annihilation in Canes Venatici I with LOFAR. *arXiv e-prints*, page arXiv:1909.12355, September 2019.

170

[320] R. A. M. Walterbos and R. Graeve. Radio continuum emission from the nuclear region of M31 Evidence for a nuclear radio spiral. A&A, 150:L1–L4, September 1985.

[321] Casey R. Watson, Zhiyuan Li, and Nicholas K. Polley. Constraining sterile neutrino warm dark matter with Chandra observations of the Andromeda galaxy. *Journal of Cosmology and Astro-Particle Physics*, 2012:018, Mar 2012.

[322] W. R. Webber, M. A. Lee, and M. Gupta. Propagation of cosmic-ray nuclei in a diffusing galaxy with convective halo and thin matter disk. ApJ, 390:96–104, May 1992.

[323] Xenon Collaboration. Dark Matter Search Results from a One Ton-Year Exposure of XENON1T. Phys. Rev. Lett., 121(11):111302, September 2018.

[324] T. Yapici, A. Smith, and HAWC Collaboration. Dark Matter Searches with HAWC. In *35th International Cosmic Ray Conference (ICRC2017)*, volume 301 of *International Cosmic Ray Conference*, page 891, January 2017.

[325] Naoki Yoshida, Volker Springel, Simon D. M. White, and Giuseppe Tormen. Weakly Self-interacting Dark Matter and the Structure of Dark Halos. ApJ, 544(2):L87–L90, December 2000.

[326] Dawei Zhong, Mauro Valli, and Kevork N. Abazajian. Entering the Era of Dark Matter Astronomy? Near to Long-Term Forecasts in X-Ray and Gamma-Ray Bands. *arXiv e-prints*, page arXiv:2003.00148, February 2020.

[327] Bei Zhou, Yun-Feng Liang, Xiaoyuan Huang, Xiang Li, Yi-Zhong Fan, Lei Feng, and Jin Chang. GeV excess in the Milky Way: The role of diffuse galactic gamma-ray emission templates. Phys. Rev. D, 91(12):123010, June 2015.

[328] F. Zwicky. Die Rotverschiebung von extragalaktischen Nebeln. *Helvetica Physica Acta*, 6:110–127, January 1933.